IN THIS ISSUE

IMAGE: OBSERVATORY WITH STAR TRAILS ON MOUNTAINS FOR CLEAR SKY

London Journals Press

www.journalspress.com

LONDON JOURNAL OF ENGINEERING RESEARCH

Volume 22 | Issue 8 | Compilation 1.0

Print ISSN: 2631-8474
Online ISSN: 2631-8482
DOI: 10.17472/LJER

COMPILED IN UNITED KINGDOM

ENGLISH

London Journal of Engineering Research

Volume 22 | Issue 8 | Compilation 1.0

PUBLISHER

London Journals Press
1210th, Waterside Dr, Opposite Arlington Building, Theale, Reading
Phone:+444 0118 965 4033 Pin: RG7-4TY United Kingdom

SUBSCRIPTION

Frequency: Quarterly

Print subscription
$280USD for 1 year
$500USD for 2 year
(color copies including taxes and international shipping with TSA approved)

Find more details at https://journalspress.com/journals/subscription

ENVIRONMENT

London Journals Press is intended about protecting the environment. This journal is printed using led free environmental friendly ink and acid-free papers that are 100% recyclable.

London Journals Press Headquaters

1210th, Waterside Dr,
Opposite Arlington
Building, Theale, Reading
Phone:+444 0118 965 4033
Pin: RG7-4TY
United Kingdom

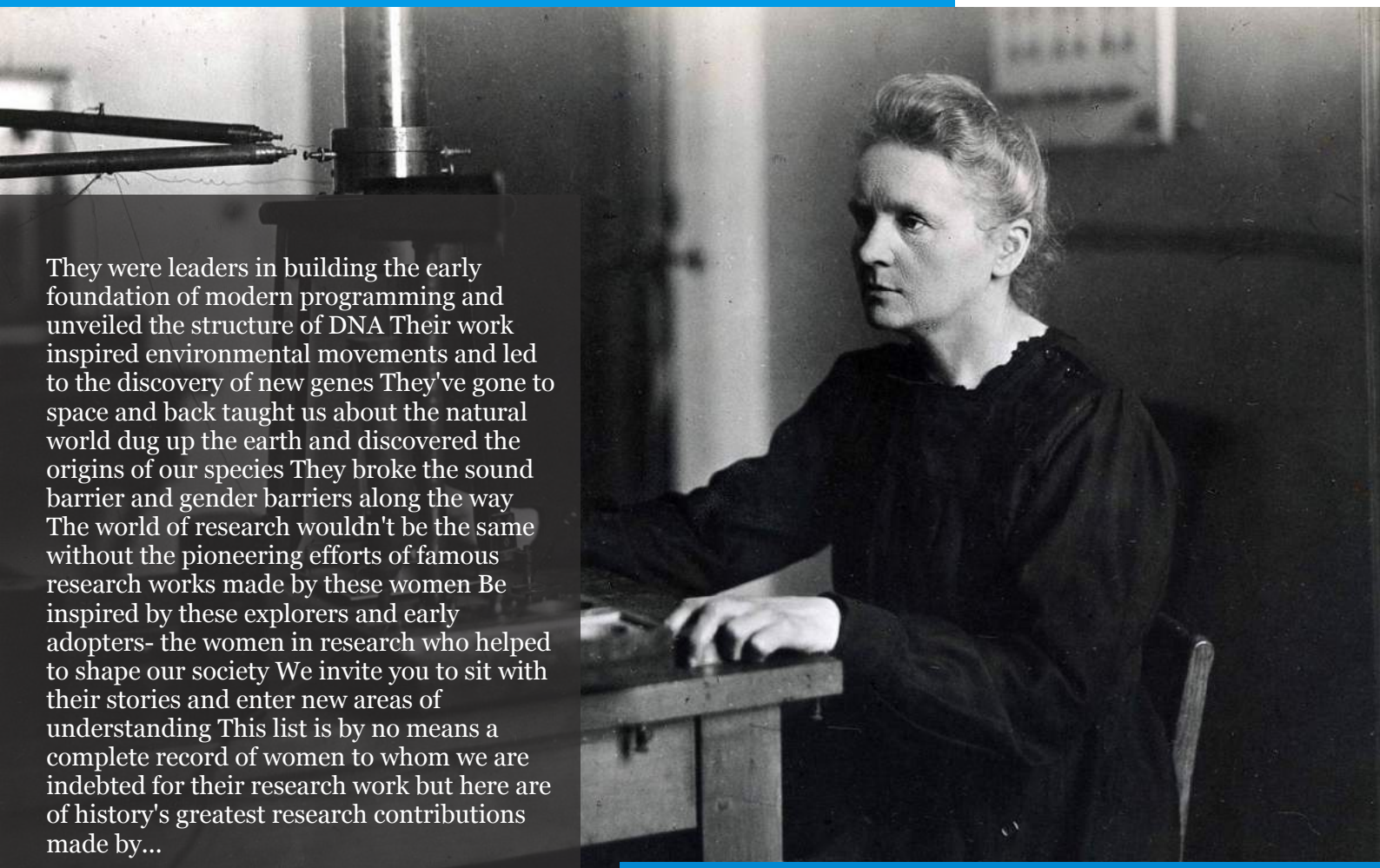

They were leaders in building the early foundation of modern programming and unveiled the structure of DNA Their work inspired environmental movements and led to the discovery of new genes They've gone to space and back taught us about the natural world dug up the earth and discovered the origins of our species They broke the sound barrier and gender barriers along the way The world of research wouldn't be the same without the pioneering efforts of famous research works made by these women Be inspired by these explorers and early adopters- the women in research who helped to shape our society We invite you to sit with their stories and enter new areas of understanding This list is by no means a complete record of women to whom we are indebted for their research work but here are of history's greatest research contributions made by...

Read complete here:
https://goo.gl/1vQ3lS

Women In Research

Computing in the cloud!

Cloud Computing is computing as a Service and not just as a Product Under Cloud Computing...

Read complete here:
https://goo.gl/VvHC72

Writing great research...

Prepare yourself before you start Before you start writing your paper or you start reading other...

Read complete here:
https://goo.gl/np73jP

Journal Content
In this Issue

London Journals Press

Editorial Board

Curated board members

Geomagnetic Storm Impacts on Communication, Navigation, Surveillance, and Air Traffic Management (CNS/ATM)

Abdallah Ahmed Eid

Cairo University

ABSTRACT

On 17 March, and 23 June 2015 secondary Air Traffic Control (ATC) radar was strongly disturbed in Cairo Air Navigation Center (CANC) with deterioration and interruptions of communications (Di) at Cairo international airport the disturbances occurred when the radar antennas were pointing at the Sun. In this paper, we are studying the impacts of geomagnetic storms on Communication, Navigation, Surveillance, and Air Traffic Management (CNS/ATM) by researching and analyzing the number of hours in a geomagnetic storm per year.

According to Dst (<-50 nt) in the period from 2015 to 2021 has been analyzed, associated with (Dst) less than (-50 nT), using Dst records that tabulate the amount and vigor of geomagnetic storms, Sunspot Number (SSN) it is period connects the end of the solar cycle 24 and the beginning of the cycle 25 With comparison the deterioration and interruptions of communications (Di) at Cairo international airport Geomagnetic Storm events occur when the Sun causes disruptions to aviation Communications, Navigation, and Surveillance (CNS) systems, and elevates radiation dose levels at flight altitudes.

Keywords: geomagnetic storms/ sunspot number (SSN)/communications, navigation, surveillance (CNS) and satellite solar outage.

Classification: DDC Code: 621.3848 LCC Code: TK6592.S95

Language: English

London Journals Press

LJP Copyright ID: 392921
Print ISSN: 2631-8474
Online ISSN: 2631-8482

London Journal of Engineering Research

Volume 22 | Issue 8 | Compilation 1.0

Geomagnetic Storm Impacts on Communication, Navigation, Surveillance, and Air Traffic Management (CNS/ATM)

Abdallah Ahmed Eid

ABSTRACT

On 17 March, and 23 June 2015 secondary Air Traffic Control (ATC) radar was strongly disturbed in Cairo Air Navigation Center (CANC) with deterioration and interruptions of communications (Di) at Cairo international airport the disturbances occurred when the radar antennas were pointing at the Sun. In this paper, we are studying the impacts of geomagnetic storms on Communication, Navigation, Surveillance, and Air Traffic Management (CNS/ATM) by researching and analyzing the number of hours in a geomagnetic storm per year.

According to Dst (<-50 nt) in the period from 2015 to 2021 has been analyzed, associated with (Dst) less than (-50 nT), using Dst records that tabulate the amount and vigor of geomagnetic storms, Sunspot Number (SSN) it is period connects the end of the solar cycle 24 and the beginning of the cycle 25 With comparison the deterioration and interruptions of communications (Di) at Cairo international airport Geomagnetic Storm events occur when the Sun causes disruptions to aviation Communications, Navigation, and Surveillance (CNS) systems, and elevates radiation dose levels at flight altitudes. Space weather events may occur on short time scales, with the effects occurring from seemingly instantaneous to a few days hence. The effects of space weather come from processes that are invisible to the human eye. The sole exceptions are the brilliant auroras, spawned by energetic electrons and ions.

Energized auroras indicate the deposition of energy into the upper atmosphere, and may herald the degradation of communications, navigation, and surveillance of aircraft in the vicinity. Therefore, decision- makers in the field of aviation should be aware that the phenomena of space weather can pose a threat to the safety and efficiency of flight operations, as the answer is to know what the effects are, the potential and consequent risks of electromagnetic storms, and the options available to mitigate those risks. This means following aviation regulations, operational rules, and business practices applicable in this field.

Keywords: geomagnetic storms/ sunspot number (SSN)/communications, navigation, surveillance (CNS) and satellite solar outage.

Author: Air Traffic Controller at The National Air Navigation Services Company (NANSC), Cairo, Egypt. MSc of Astrophysics, Astronomy, Space Science and Meteorology Dept., Faculty of Science, Cairo University, Egypt.

I. INTRODUCTION

These solar events and variations can give rise to the following effects aurora, ionospheric disturbances, Solar Particle Events (SPEs), and geomagnetic storms. Probably the most well-known effect of solar-induced geomagnetic storms is the aurora borealis (northern lights) and aurora austral (southern lights). Aurorae begin between 60° and 80° latitude. As a storm intensifies, the aurorae spread toward the equator. During an unusually large storm in 1909, an aurora was visible in Singapore, on the geomagnetic equator. The aurorae provide pretty displays, but they are just a visible sign of atmospheric changes that may wreak havoc on technological systems. The bursts of electromagnetic radiation (ultraviolet and x-ray) from a solar flare journey at the speed of light and

London Journal of Engineering Research

arrive at Earth just 8 minutes after leaving the flare site. Unaffected by the Earth's magnetic field, these emissions directly affect the upper atmosphere (becoming significant below 100km) by producing a temporary increase in ionisation in the sunlit hemisphere of minutes to hours duration called a "sudden ionospheric disturbance" Certain major solar flares and CMEs can shower the Earth, within 30 minutes, with energetic particles (primarily protons).

In this case, the Earth's magnetic field does offer some protection, but some of these particles spiral down the field lines, entering the upper atmosphere in the Polar Regions where they produce additional ionisation in the ionosphere and below. Very energetic and intense events can also lead to increases at lower latitudes. One to four days after a major solar disturbance occurs, a slower cloud of solar material and magnetic field reaches Earth, buffeting the magnetosphere and resulting in a geomagnetic storm.

The bi-polar magnetic field of the Earth points north but the field contained within the material expelled from the Sun can point in any direction.

When the field is orientated in the opposite direction to that of the Earth's, the two magnetic systems interact and the solar material can enter the Earth's magnetosphere. These interactions can produce very large electrical currents, of up to a million amperes, flowing through the ionosphere and magnetosphere, which can change the direction of the Earth's magnetic field at the surface by up to 1 or 2 degrees, mainly in the aurorally regions. (Space Weather effects on airline operations (Captain Bryn Jones, VAA Cosmic Radiation Project Manager), n.d.)

Space weather is driven by the Sun and follows the "solar cycle" closely. This cycle is typically about 11 years in duration and is manifest in many of the irradiative and magnetic properties of the Sun. The solar cycle is defined in terms of "sunspots" on the solar disc. Sunspots are regions of extremely intense localized magnetic fields, which appear darker than the surrounding surface. A sunspot region on the solar surface is akin to an extreme low-pressure system or cyclone on Earth with intense magnetic fields rather than extreme winds. At times, sunspots are rare and the solar disc appears almost without blemish. This occurs at the solar minimum, the start of a solar cycle. Later, sunspots become common and it is normal to see numerous large sunspots, often assembled in complex groups, spread across the solar disc. The peak of the solar cycle, when sunspots are most numerous, is known as the solar maximum. There is a standardized way of counting sunspots present on the solar disc, to give the sunspot number or SSN, which is the traditional indicator of solar activity and the progress of the solar cycle. (Penza et al., 2021)Severe space weather conditions affect the performance of numerous modern technical systems, causing problems not only for national and global economies but for everyday life as well.

Satellite navigation systems are particularly vulnerable, even though systematic monitoring of space weather in general, is still performed on a global scale. Space weather effect correction models applied within the standard satellite positioning service are not capable of tackling the effects of severe space weather conditions and local ionospheric characteristics. Severe space weather effects on the GPS ionospheric delay are intensely studied to provide advanced models of the space weather effects on GPS positioning performance. Here one study of severe space weather conditions and their consequences on the GPS ionospheric delay in Croatia is presented.

The study takes advantage of the availability of the space weather indices and the GPS pseudo-range measurements (taken at the reference site at Osijek, Croatia) related to a major severe space weather event lasting from early October 2003 to late November 2003. (Filjar, 2007)

Space weather impacts occur to communications, navigation, surveillance, radiation-sensitive electronics, and human exposure the system impacts may include: (ICAO, n.d.)

1.1 Unexpected Loss of Communications

— HF voice and HF data link, i.e. Controller Pilot Data Link Communication (CPDLC), on routes where HF is employed;

— Poor or unusable performance of L-band SATCOM;

1.2 Degraded Performance of Navigation and Surveillance That Rely on GNSS

— Automatic Dependent Surveillance- Broadcast (ADS-B) and/or Automatic Dependent Surveillance –Contract (ADS-C) anomalies;
— Sporadic loss-of-lock of GNSS, especially near the equator, post-sunset;

1.3 Unanticipated Non-Standard Performance of On-Board Electronics, Resulting in Reboots and Anomalies; and

1.4 Issues Related to Radiation Exposure by Aircrew and Passengers

II. METHODOLOGY

Identify and manage the risks that threaten the management of air traffic by responding quickly and positively to mitigate the effects of electromagnetic storms that cause disruption and deterioration of communication, navigation, and Surveillance based on satellites (CNS).

Therefore, the researcher believes that the strategic objective of the research is an investigation of:

1) *Safety by:* enhancing global civil aviation safety
2) *Security by:* enhancing the security of the Air Traffic Management (ATM)
3) *Efficiency by:* enhancing Air Traffic Flow Management (ATFM)
4) *Continuity by:* maintaining the continuity of flight operations

Space weather events impact aviation operations by degrading the performance of Communication, Navigation, and Surveillance services and solar radiation can be detrimental to the health of crews and passengers. (ICAO, n.d.) Communication and Navigation satellites can be disabled by significant solar events and more commonly, in the Polar Regions; space weather conditions can blackout high-frequency satellite communication and satellite navigation services for periods from minutes to several hours. (www.ICAO.int, n.d.)

2.1 Space Weather Impacts on Communications

All communications with aircraft EN Route poleward of 82-degree latitude can be lost during a disruptive space weather event. As flight paths venture to the poleward side of the 80th parallel, they lose their communication link with the geosynchronous communication satellites due to the earth's curvature, and conventional HF radio communication must be employed. Solar storms can render HF communications inoperable for periods of minutes to hours over several days during disruptions in the ionosphere's electron density to the point of becoming unable to bounce radio signals back to the aircraft. These disruptions are driven by the size and location of the disturbance on the sun that triggers these events. There are polar-orbiting satellites available to partially fill this communication gap, but to date; most airlines are not equipped to take advantage of this capability. Space weather interferes with HF or VHF/UHF communications, the problems can quickly become serious. No ground-based air traffic control radar is available over the poles or oceans, so without communications, air traffic controllers have no position reports on the plane. (kejian1.cmatc.cn, n.d.)

This means they cannot verify aircraft separation, which compromises the critical Situational awareness needed for flight safety. Furthermore, without a means of contacting the crew, ATC has no way of finding out whether deviations from the flight path have occurred. Ultimately, failure to make contact can result in ATC initiating search and rescue operations.

2.1.1 Communications Issues Related to Recent Space Weather Events are Reported Below:

A. Thirteen overdue position reports for flights over Central East Pacific and Central West Pacific (1830-1930Z Jan 27, 2012, R3 radio blackout)
B. HF service degraded for over two hours (Oct 19, 2003, R3 radio blackout)

C. Degradation of high latitude (Oct 24, 2003, G3 geomagnetic storm)
D. Widespread HF communications problems in Alaska (Jan 22-23, 2012 S3 SRS)
E. Communications problems in Asia and the Pacific (Jan 22, 2012, daytime R2 radio blackout)
F. Communications problems off U.S. East Coast and West Coast (Jan 27, 2012 daytime radio blackout)

2.2 Space Weather Impacts on Satellite Navigation

Geomagnetic Storms: Disturbances in the geomagnetic field caused by gusts in the solar wind that blows by Earth. Typical effects from geomagnetic storms include degradation of HF radio transmissions, satellite navigation degradation, and disruption of low-frequency radio navigation systems. (Fisher and Kunches, 2011) Geomagnetic storms can also disrupt electrical power grids, and GPS operations are susceptible to these power outages. Geomagnetic storms also weaken the ability of the Earth's magnetic field to deflect incoming charged particles.

III. DATA SOURCES

The data used for this study is classified and retrieved with the permission of the Air Traffic Control System (ATCS). Is a device in the French THALES system (Thales Group, n.d.) that identifies errors and threats that affect air traffic management, which is recorded in the air safety department and followed up periodically through the International Civil Aviation Organization to develop and raise efficiency. We have collected the events with the number of hours Dst (<-50nT) during the period 2015–2021. A list of magnetic storms based on the Dst indices provided by Kyoto University's Data Analysis Center for Geomagnetism and Space Magnetism Graduate School of Science (wdc.kugi.kyoto-u.ac.jp, n.d.), the number of days with a geomagnetic storm per year. According to the finalized KP-index GFZ Potsdam periods from 2015 to 2021, the KP index We used the monthly SSN provided by the Solar Influences Data Analysis Center (sidc.oma.be) and the solar polar field throughout the solar sunspot cycle provided by the Wilcox Solar Observatory (wso.stanford.edu, n.d.). The source of the data is taken from (c=AU; co=Commonwealth of Australia; ou= Department of Sustainability, n.d.)

The total sunspot number data is provided by the Royal Observatory of Belgium, Brussels, and can be downloaded from the SILSO website (www.sidc.be, n.d.). In addition, it can be found at (www.ngdc.noaa.gov, n.d.)

IV. RESULTS AND DISCUSSION

We have followed the duration of (*Di*) at (CANC) in the period for study from 2015 to 2021 by monitoring and following up on all the days of the interruption during the previous years It is observed in all the monitoring years (*Di*) from 2015 to 2019 the rise in the (*Di*) is the observed year 2015 and then the gradual decline and disappearance the year 2019 It is noted that the duration of (*Di*) increased in Cairo year 2020 and 2021, the beginning of the index rises again and we noted that communications have been repeatedly deteriorated and interrupted at Cairo Air Navigation Center. The equation (1) below is used to calculate the total duration (*Di*) for every year from 2015 to 2021.

$$D_i = \sum_{j=1}^{k} C_{ij} \qquad i = 1, 2, \cdots, 7 \tag{1}$$

Where D_i , = 1, 2, ···, 7. Is the total duration of the deterioration and interruptions of the communications during a specific year from 2015 to 2021, respectively, and C_{ij}, =1, 2, ···, 7.

j=1, 2, ···, is the duration of the deterioration and interruptions of the communications during the specified year i, and k refers to the number of days of the specified year.

London Journal of Engineering Research

Table 1: This Shows the Total Number of Deterioration and Interruptions of Communications That Happen Annually in Minutes, Over the Study Period (2015 - 2021) at (CANC)

Year	2015	2016	2017	2018	2019	2020	2021
Duration(MIN)	575	493	380	360	250	355	370

The graph below shows the duration of (*Di*) at (CANC) the maximum in the year 2015 is 575 MIN, and the minimum in the year 2019 is 250 MIN, which indicates the beginning of the index rise again in the year 2020 and 2021.

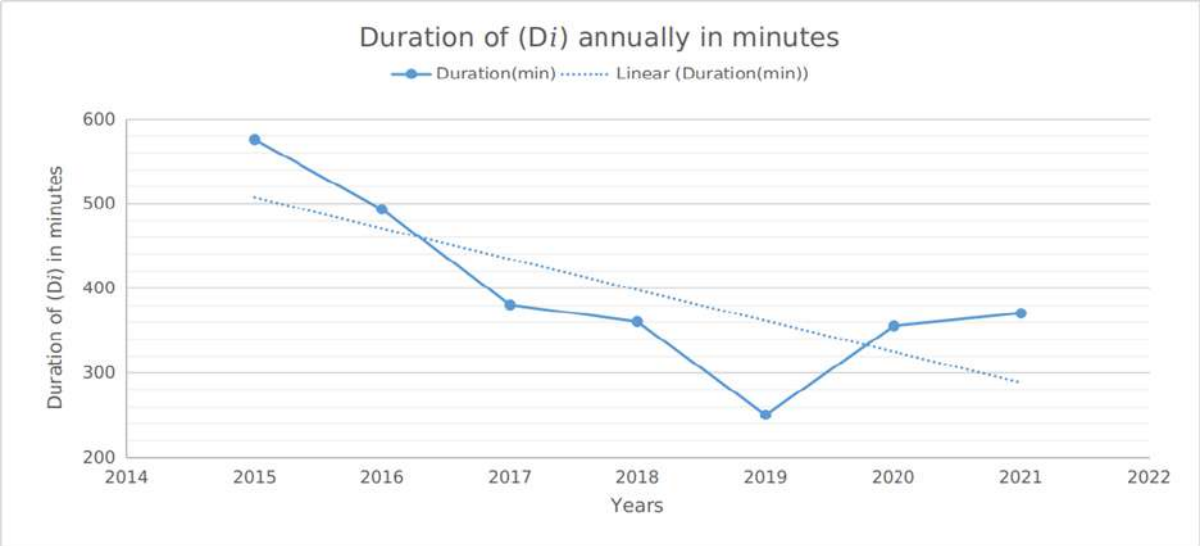

Figure 1: The Duration of (*Di*) at (CANC) in the Periods From 2015 to 2021

4.1 Satellite Solar Outage Impact

The duration of (Di) at (CANC) in the periods from 2015 to 2021 during Satellite Solar Outage It is noted high of the duration of (Di) during Satellite Solar Outage has increased in Cairo in 2015 and gradually decreased until 2020 and indicates the beginning of the index rise again in the year 2021(Guo et al., 2012)

The equation (2) below is used to calculate the total duration (*Di*) during periods I and II for every year from 2015 to 2021

$$D_i = \sum_{j=1}^{m} C_{i1j} + \sum_{j=1}^{n} C_{i2j} \qquad i = 1, 2, \cdots, 7 \tag{2}$$

Where *Di*, $i = 1, 2, \cdots, 7$. is the total duration of the deterioration and interruptions of the communications during a specific year from 2015 to 2021 , respectively *Ci*1*j*, $i = 1, 2, \cdots, 7$,

$j = 1, 2, \cdots, m$ is the duration of the deterioration and interruptions of the communications during the period I in the specified year *i* and *m* refers to the number of days of February and March in the specified year *i*, and *Ci*2*j*, $i = 1, 2, \cdots, 7, j = 1, 2, \cdots,$ *n* is the duration of the deterioration and interruptions of the communications during period II in the specified year *i*, and *n* refers to the number of days of September and October in the specified year *i*. Notated that period I starts from the first day of February till the end day of March in the specified year *i*, while period II starts from the first day of September till the end day of October in the specified year *i*.

Table 2: Shows the total number of deterioration and interruption of communication that happens annually in minutes, to the Satellite Solar Outage (period I and II) (2015-2021)

Year	2015	2016	2017	2018	2019	2020	2021
Duration(min)	434	381	324	294	239	198	240

The graph below shows the duration of (*Di*) at (CANC) in the periods from 2015 to 2021 during Satellite Solar Outage (periods I and II)) the maximum in the year 2015 is 434 MIN, and the minimum in the year 2020 is 198 MIN, which indicates the beginning of the index rise again in the year 2021.

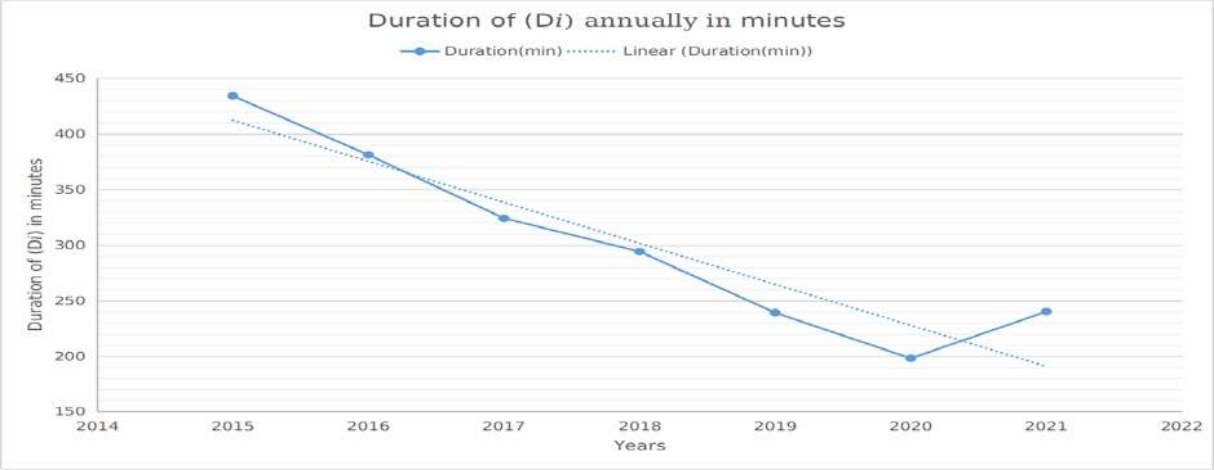

Figure 2: Shows the Duration of (Di) at (CANC) in the Periods From 2015 to 2021 During Satellite Solar Outage (Period I and II)

4.2 Geomagnetic Storms

A geomagnetic storm is a major temporary disturbance in the Earth's magnetic activity and is associated with solar activity, e.g., coronal mass ejection (CME) and high-speed solar wind stream (HSS) (S. O. Ikubanni et al., 2020). When there is greater solar activity, geomagnetic storms are mainly generated by CME; while during moments of less solar activity, it is the coronal holes that have a dominant effect (Gonzalez, Tsurutani, and Clúa de Gonzalez, 1999). Geomagnetic storms occur when there is a large sudden change in the solar wind dynamic pressure at the magnetopause (Mengistu Tsidu and Abraha, 2014)The distinctive characteristic of a geomagnetic storm is a clear decrease in the horizontal intensity of the magnetic field (Gonzalez et al., 1994) Geomagnetic storms can be usually divided into three main phases: initial, main, and recovery (Joshua et al., 2014). Geomagnetic storms are detected prior to the ionospheric disturbances and to the decrease in positioning estimation.

Different geomagnetic indices are used to characterize geomagnetic storms such as the disturbance storm time (Dst) index, geomagnetic disturbance (Kp), averaged geomagnetic activity (Ap) (based on data from a set of specific Kp stations), and the auroral electrojet (AE) index, where the Dst-index is associated with the effects on the equatorial region, the Kp-index to the mid-latitudes, and the AE-index at high latitudes since it characterizes the intensity of ionospheric currents during magnetic storms and substorms activity (Davis and Sugiura, 1966) and (Boroev and Vasiliev, 2020).

The Dst-index has been used historically to characterize the severity of a geomagnetic storm.

Depending on the Dst value, the storms are usually classified in ranges such as weak (−30 nT and −50 nT), moderate (−50 nT and −100 nT), intense (−100 nT and −200 nT), very intense (−200 nT and −350 nT), and great (Dst below

−350 nT) (Borovsky and Shprits, 2017) Furthermore, the Kp-index is based on 3 h measurements from ground- based magnetometers around the world (www.spacew eatherlive.com, n.d.) The storms are usually classified as minor (G1) with a Kp = 5; moderate (G2) with a Kp = 6; strong (G3) with a Kp = 7; severe (G4) with Kp = 8, and extreme (G5) with Kp = 9 (www.swpc.noaa.gov, n.d.).The Ap-index provides a daily average level for geomagnetic activity. The Kp-value converts to a linear scale called the a- index. The average from eight daily a-values gives us the Ap-index of a certain day. Thus, high levels of geomagnetic activity have a higher daily Ap-value (Matzka et al., 2021).

The geomagnetic storms can also be identified by various other parameters such as the symmetric disturbance of the magnetic field H (SYM-H); the interplanetary electric field (IEF); and the interplanetary magnetic field (IMF), where IMF-Bz is the most important parameter for the study of geomagnetic storms, as the energy input into the magnetosphere, depends on Bz orientation and its magnitude (Desai and Shah, 2018) Although these indexes provide extra information regarding the space conditions, some of them are related to The Dst-index. For instance, a relationship has been shown between Dst and Bz (Gonzalez and Echer, 2005). The response of the ionosphere to geomagnetic-induced disturbances is known as an ionospheric storm (Mendillo, 2006) and (Joshua et al., 2018).

The ionosphere plasma density is mainly determined by the chemistry/composition, transport due to electric fields, transport due to neutral wind, and transport due to ambipolar diffusion. During geomagnetic storms, the variations of chemistry or the thermospheric composition, the interaction with the neutrals (neutral wind) (Cai et al., 2021) and (Yu et al., 2021 and/or variations of electric field and ambipolar diffusion (Tsurutani et al., 2008) are the final cause that alters the ionosphere plasma density. Nevertheless, the response of the ionosphere during a geomagnetic storm is complex and difficult to predict accurately, and the physical nature of many underlying mechanisms needs a better understanding to obtain precise forecasting of its behavior based on geomagnetic storm parameters (Samed Inyurt, 2020).

In addition, the effects of these physical processes on the ionosphere have also been reported to vary with solar activity, storm intensity, storm duration, season, location, local time, and altitude of the observing station, which increases the forecast uncertainties (Liu et al., 2008).

The table2: below shows the number of days with a geomagnetic storm per year from 2015 to 2021 and how strong those storms were (www.gfz-potsdam.de, n.d.) during the end of the Solar Cycle 24 and the beginning of the Solar Cycle 25. The Source of the Kp index is the Kp-website of GFZ (www.gfz-potsdam.de, n.d.)

Year	G1	G2	G3	G4	G5	Total
2015	43	18	5	3	0	68 days
2016	45	18	0	0	0	63 days
2017	37	12	2	2	0	53 days
2018	12	7	2	0	0	21 days
2019	16	2	0	0	0	18 days
2020	8	1	0	0	0	9 days
2021	19	4	1	1	0	25 days

Table 2: Shows the Number of Days With a Geomagnetic Storm per Year According to Finalized KP-Index GFZ Potsdam, Over the Study Period (2015-2021)

Year	2015	2016	2017	2018	2019	2020	2021
Number of Day	68	63	53	21	18	9	25

The graph below shows the number of days with a geomagnetic storm per year and how strong those storms were. This will give you an idea of which years there were many geomagnetic storms in the periods from 2015 to 2021. The Source of the Kp index is the Kp-website of GFZ (www.gfz-potsdam.de, n.d.) the maximum in the year 2015 is 68 Days, and the minimum in the year 2020 is 9 days which indicates the beginning of the index rise again in the year 2021.

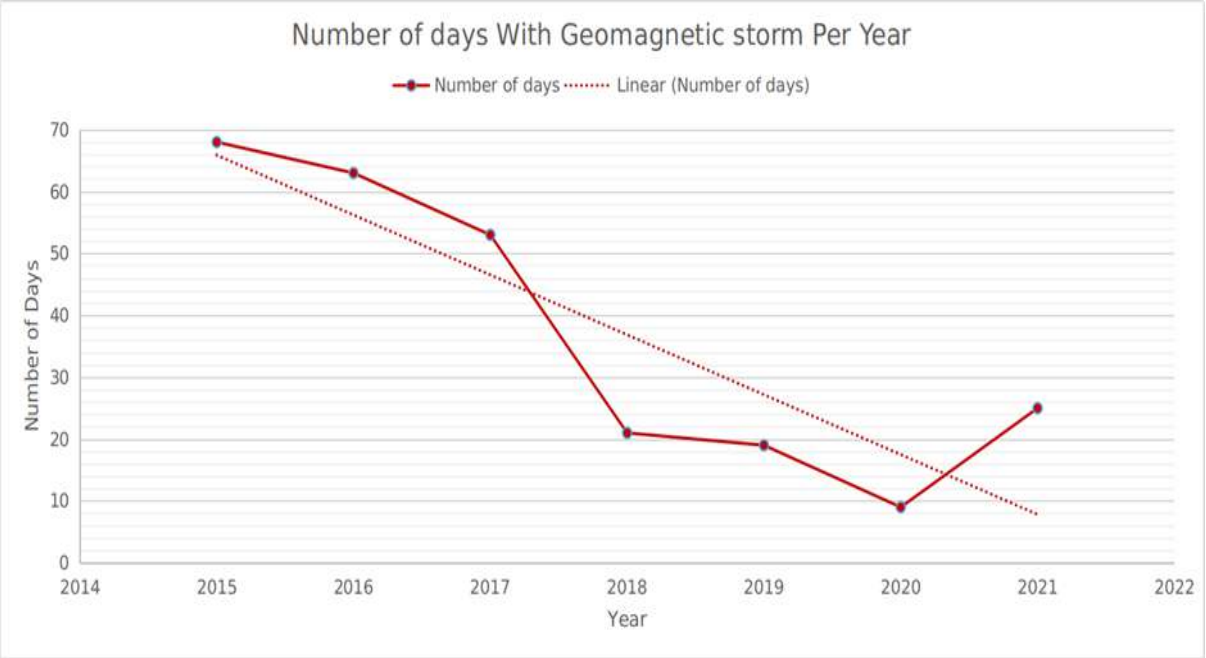

Figure 3: The Number of Days With a Geomagnetic Storm per Year According to Finalized KP- Index GFZ Potsdam Periods From 2015 to 2021

The disturbance storm time (Dst- index) is a measure in the context of space weather. It gives information about the strength of the ring current around Earth caused by solar protons and electrons. The ring current around Earth produces a magnetic field that is directly opposite Earth's magnetic field, i.e. if the difference between solar electrons and protons gets higher, then Earth's magnetic field becomes weaker (Clette et al., 2015). A negative Dst value means that Earth's magnetic field is weakened. This is particularly the case during Geomagnetic storms. (Kyoto-u.ac.jp, 2022)

The Dst-index has been used historically to characterize the severity of a geomagnetic storm. Depending on the Dst value, the storms are usually classified in ranges such as weak (−30 nT and −50 nT), moderate (−50 nT and −100 nT), intense (−100 nT and −200 nT), very intense (−200 nT and −350 nT), and great (Dst below −350 nT), (Borovsky and Shprits, 2017) and Our study will depend on the intensity of the geomagnetic storm. Depending on the value of Dst, storms are classified as moderate (−50 nT) periods from 2015 to 2021 during the end of Solar Cycle 24 and the beginning of Solar Cycle 25.

To get the number of hours with a Geomagnetic Storm per year (N_i), we present the following equation (3)

$$N_i = \sum_{j=1}^{k} G_{ij} \qquad i = 1, 2, \cdots, 7 \tag{3}$$

Where N_i,i=1,2,⋯,7 is the total number of hours with a Geomagnetic Storm during a specific year from 2015 to 2021, respectively and G_{ij}, i=1,2,⋯,7, j =1,2,⋯,k is the number of the hours with a Geomagnetic Storm during the specified year i with, Dst < −50 nt and k refer to the number of days of the specified year i.

The year 2015 was chosen because it is the highest in the number of hours with a geomagnetic storm per year According to Dst (< -50 nt) The period from 2015 to 2021 connects the end of the solar cycle 24 and the beginning of the cycle 25. We have followed the Number of hours with a geomagnetic storm per year According to Dst (< -50 nt) in the period for study from 2015 to 2021 by monitoring and using Equation (2) We found the number of hours with a geomagnetic storm per year According to Dst (< -50 nt) have increased in 2015 and gradually decreased until 2019 and increased during the year 2020 and 2021, i.e. the beginning of the index rise again The graph below shows the number of hours with a Geomagnetic Storm per year According to Dst (< -50 nt) in the period from 2015 to 2021.

Table 4: Shows the Number of Hours With a Geomagnetic Storm per Year According to Dst (< -50 Nt), Over the Study Period (2015-2021)

Year	2015	2016	2017	2018	2019	2020	2021
Number of hours	560	182	89	64	14	25	55

The graph below shows the number of hours with a Geomagnetic Storm per year According to Dst (< -50 nt)in the period from 2015 to 2021, the maximum in the year 2015 is 560 hours, and the minimum in the year 2019 is 14 hours which indicates the beginning of the index rise again in the year 2020 and 2021.

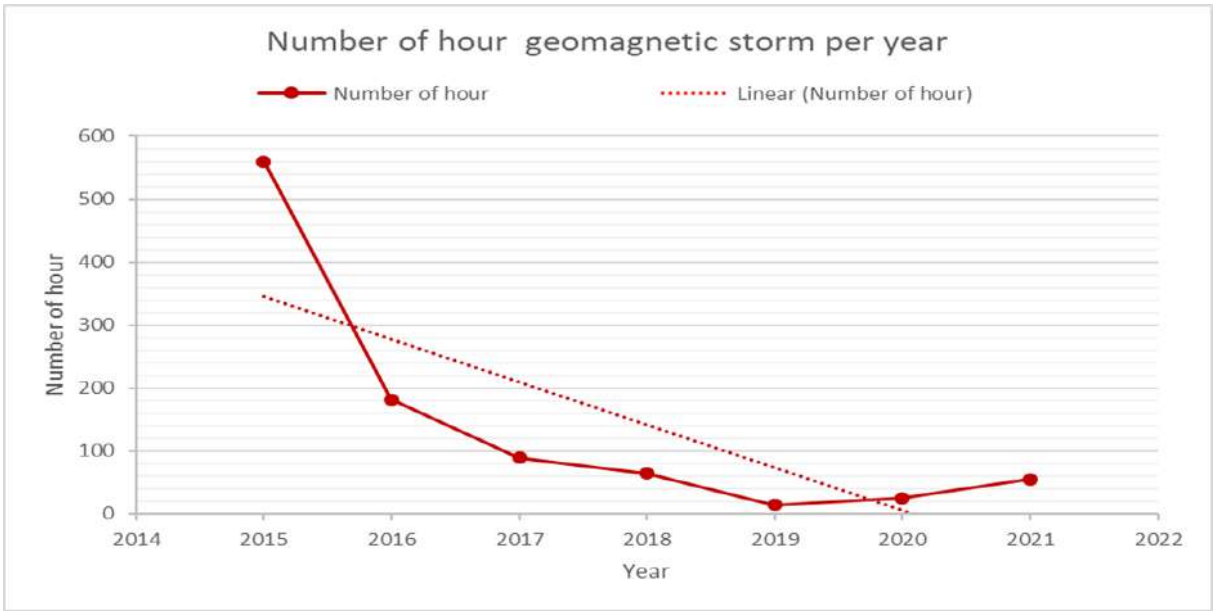

Figure 4: The Number of Hours With a Geomagnetic Storm per Year According to Dst (< -50 Nt) in the Period From 2015 to 2021

4.3 The Solar Cycle and Sunspots

Space weather is driven by the Sun and follows the "solar cycle" closely. This cycle is typically about 11 years in duration and is manifest in many of the irradiative and magnetic properties of the Sun. Solar activity is not constant and, from time to time, eruptions appear on the sun's surface which results in an abnormal level of radiation and particle ejection. (Clette et al., 2015)

The equation (4) below is used to calculate the Observed Sunspot Number (S_i) for every year from 2015 to 2021

$$S_i = \sum_{j=1}^{12} S_{ij} \qquad i = 1, 2, \cdots, 7 \tag{4}$$

Where $S_i, i = 1, 2, \cdots, 7$ the total sunspot numbers during a specific year from 2015 to 2021, respectively, and $S_{ij}, i = 1, 2, \cdots, 7, j = 12, \cdots, 12.$ is the observed monthly sunspot number.

We have followed the Solar Cycles (SSN) in the period for study from 2015 to 2021 by monitoring and using Equation (4) We found the Solar Cycles (SSN) increased in 2015 and gradually decreased until 2019 and increased during the year 2020 and 2021, i.e. the beginning of the (SSN) rise again. The graph below shows sunspot measurements for Solar Cycle 24, which ended in 2019 and started new Solar Cycle 25 in the period from 2015 to 2021

Table 5: Shows the Sunspot Number (SSN), Over the Study Period (2015-2021)

Year	2015	2016	2017	2018	2019	2020	2021
Sunspot Number	783.4	477.9	261.8	84.1	43	105.5	353.8

The graph below shows the Sunspot Number (SSN) in the period from 2015 to 2021 the maximum in the year 2015 is 783.4, and the minimum in the year 2019 is 43, which indicates the beginning of the index rise again in the year 2020 and 2021.

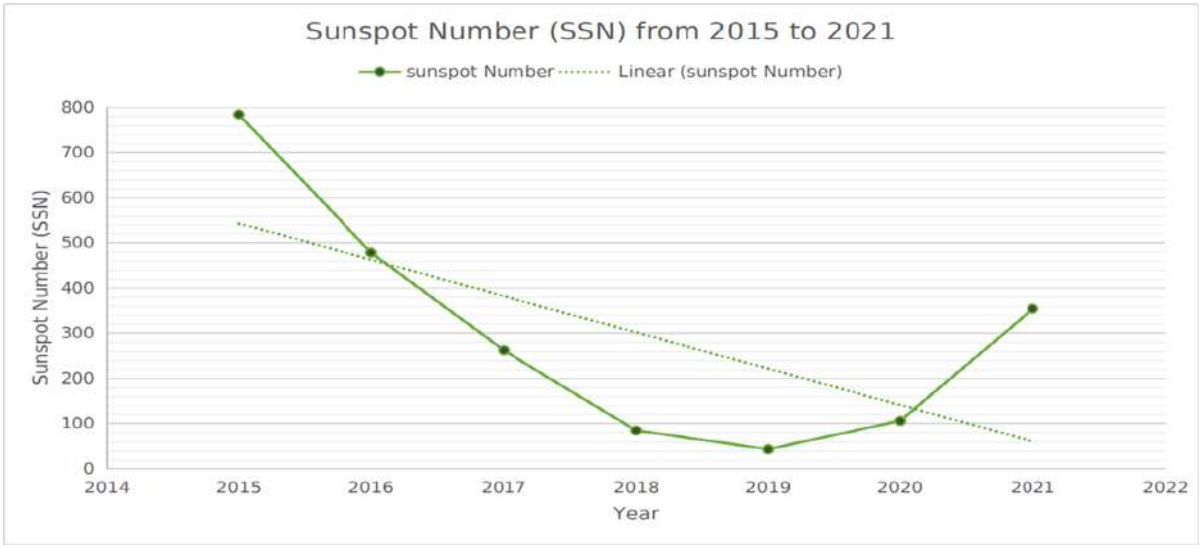

Figure 5: Sunspot Number (SSN) in the Period From 2015 to 2021

Table 6: Shows a Comparison between The number of hours with a geomagnetic storm per year According to Dst (< -50 nt), Sunspot Number (SSN), and the Duration of (*Di*) at (CANC), over the study period (2015-2021) we noticed an increase in 2015 and gradually decreased until 2019 and increased during the year 2020 and 2021, namely the occurrence rate tends to be increased

Year	2015	2016	2017	2018	2019	2020	2021
Dst	560	182	89	64	14	25	55
Sunspot Number	783.8	477.9	261.8	84.1	43	105.5	353.8
Duration	575	493	380	360	250	355	370

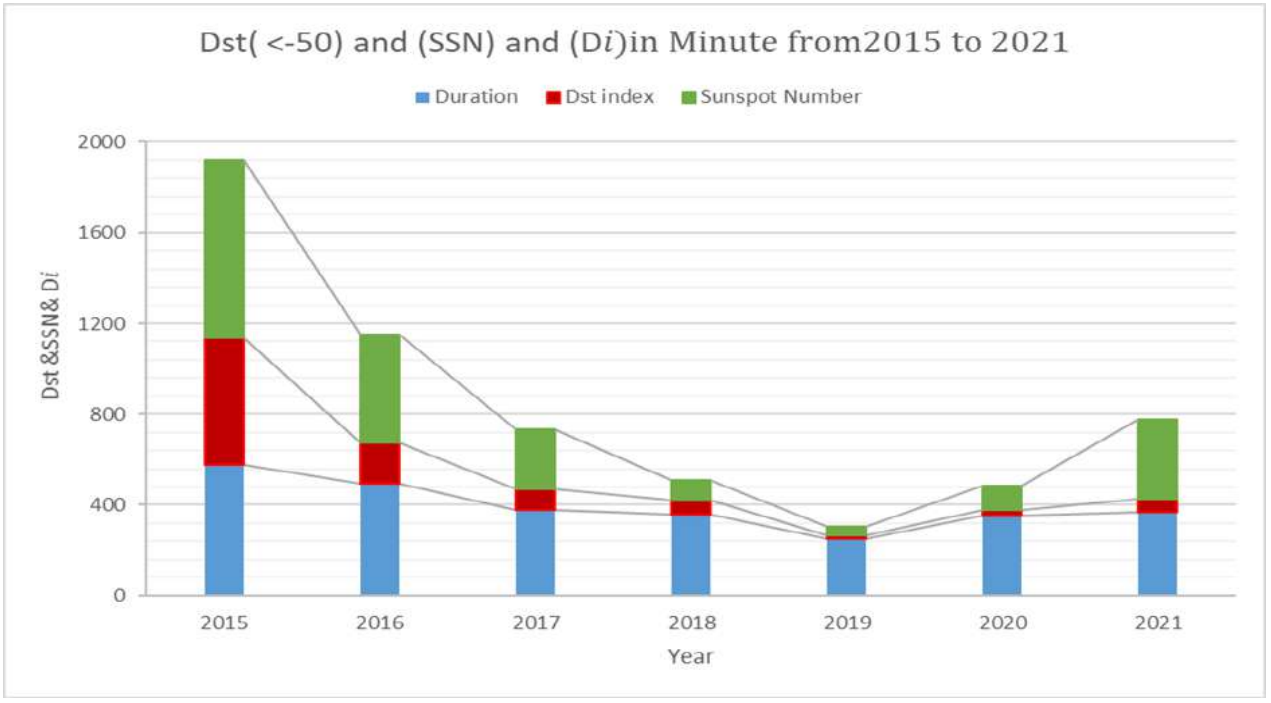

Figure 6: Shows a Comparison Between the Number of Hours With a Geomagnetic Storm per Year According to Dst (< – 50 Nt) and the Solar Cycles (SSN) and the Duration of (Di) at (CANC) in the Period From 2015 to 2021

V. CASE STUDY (1) EVENT OF 17 MARCH 2015 AT CAIRO INTERNATIONAL AIRPORT

On 17 March 2015 at Cairo International airport, radar failure, and loss of radar identification, instructions were issued to restore non-radar standard separation and the pilot was instructed to communicate with the ATS unit concerned.

Therefore, without communications, air traffic controllers have no position reports on the plane.

This means they cannot verify aircraft separation, which compromises the critical situational awareness needed for flight safety.

Furthermore, without a means of contacting the crew, ATC has no way of finding out whether deviations from the flight path have occurred.

Ultimately, failure to make contact can result in ATC initiating search and rescue operations. The (*Di*) is 40 minutes on17 March 2015, the graph below shows the duration of (*Di*) in minutes at Cairo International airport on 17 March 2015.

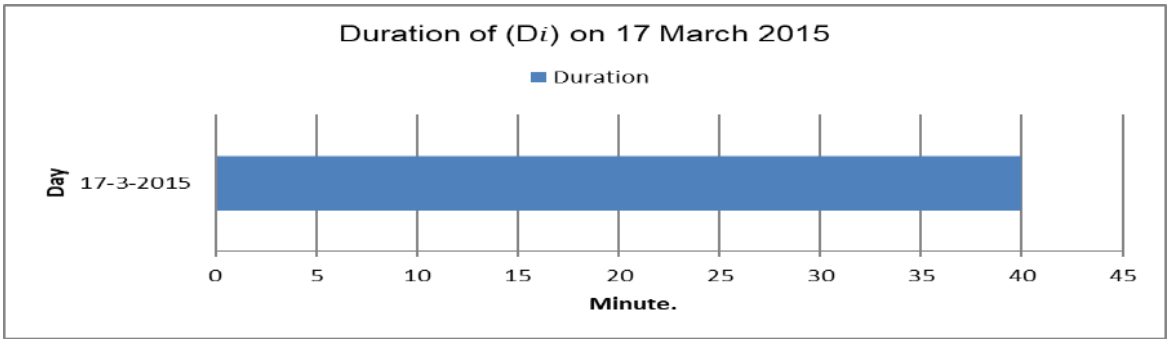

Figure 7: Shows the Duration of (Di) in Minutes at the Cairo International Airport on 17 March 2015

The geomagnetic storm under study occurred on 17 March 2015. It can be classified as The Strongest G4 Storm of Solar Cycle 24, known as the St. Patrick's Day storm on March 17, 2015, Super Geomagnetic Storm (−200 nt) The main phase of this storm lasted two hours or 120 minutes originating by the impact on Earth's atmosphere of coronal mass ejections (CMEs), the storm reaching the condition of G4 (severe) level, in the NOAA geomagnetic scale (Kil et al., 2016) The graph below shows the super geomagnetic storm Dst(< −200 nt) of solar cycle 24 which occurred on 17 March 2015.

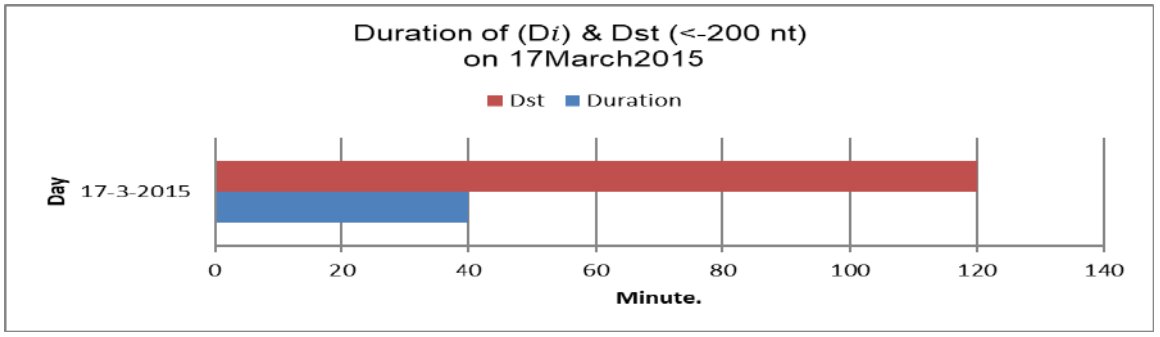

Figure 8: Shows a Comparison Between the First Super Geomagnetic Storm of Solar Cycle 24 Occurred Dst (< −200 nT) and the Duration of (*Di*) at Cairo International Airport on 17 March 2015

VI. CASE STUDY (2) EVENT OF 23 JUNE 2015 AT CAIRO INTERNATIONAL AIRPORT

The graph below shows the deterioration and interruption of communication at Cairo International airport in 25 minutes. This event affected the safety and security of Egyptian Air Traffic Management on 23 June 2015.

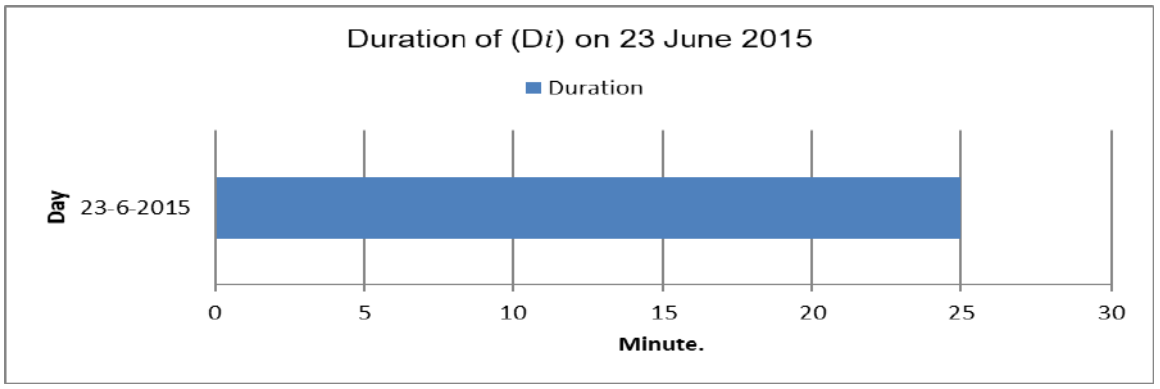

Figure 9: Shows the Duration of (*Di*) at the Cairo International Airport on 23 June 2015

After analyzing the data shown in the graph below Comparison the duration of (*Di*) at Cairo International airport is 25 minutes and The second largest geomagnetic storm Dst (< −200 nt) is 60 minutes on June 23, 2015, we noticed this event has affected the safety and security of Egyptian Air Traffic Management.

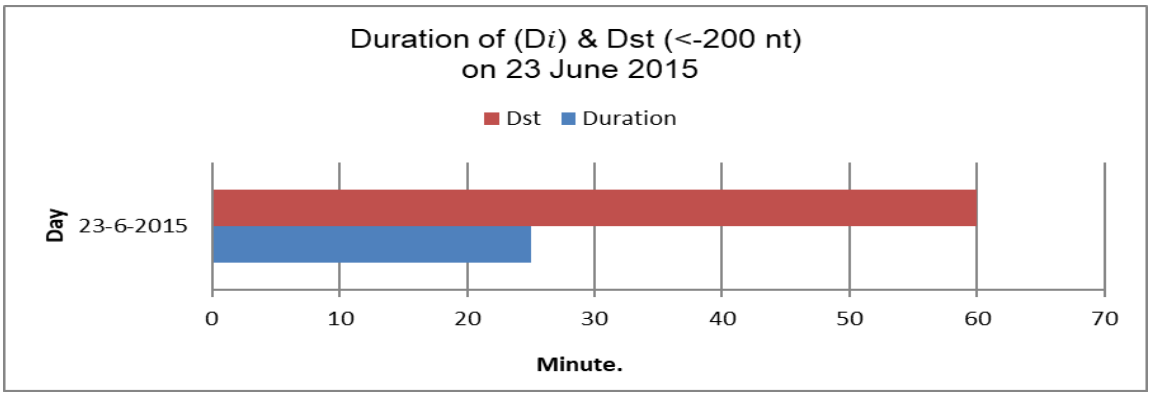

Figure 10: Shows a comparison between Geomagnetic storm Dst (< −200 nT) of Solar Cycle 24 that occurred on 23 JUNE, 2015, and the duration of (*Di*) at the Cairo International airport on June 23, 2015

VII. CONCLUSION

Realize the objective of diagnosing how geomagnetic storms affect CNS/ATM (communication, navigation, surveillance, and air traffic management). According to a study and analysis of the outages and degradation of contacts in the base's air center from 2015 to 2021, the maximum outage and disruption of communications occurred in 2015 for a total of 575 minutes, and the minimum occurred in 2019 for a total of 250 minutes. In 2020, however, the degradation and disruption of communications started to rise once more for a total of 355 minutes, and after monitoring in 2021, it was confirmed that it occurred for 370 minutes.

Aswan International Airport in Egyptian airspace is the change of the natural geographical process of study in general, and the results are identical to those of the first Cairo International Airport, with (*D1*) Act 2015 being 605 minutes, which is the majority, as well as (*D5*) for the year 2019 being 285 minutes, which is the minimum, and the beginning of the increase in (*D6*) 2020 being 375 minutes, which indicates the beginning of the rise. The investigation and analysis of the communications breakdown and deterioration at the Cairo Aeronautical Center during Periods I and II of the Satellite Solar Outage, The conclusion drawn from the two time periods above is that (*D1*) for the year 2015 is the highest degree and (*D6*) for the year 2020 is the lowest

degree. Studying and analyzing how communications in the second terminal of the Aswan International Airport changed and were disrupted during the same two times as above led to the conclusion that (*D1*) for the year 2015 was the highest degree and (*D6*) for the year 2020 was the lowest degree.

Based on research and analysis of the number of geomagnetic storm days per year from 2015 to 2021, the largest number of days, or 68 per day, is categorized as follows:

The minimum number of geomagnetic storm days in a year is specifically one day for which they are classed as follows: 43 days of a minor (G1), 18 days of moderate (G2), 5 days of strong (G3), and 3 days of severe (G4). 1 day of a moderate, 8 days of a minor (G1) (G2).

The duration of a geomagnetic storm in hours per year has been studied and analyzed. In the years 2015 through 2021, the greatest number of hours worked is 560, and the minimum number of hours worked is 14, according to Dst (-50 nt).

Using Dst records that tabulate the quantity and intensity of geomagnetic storms, Sunspot Number (SSN), and the deterioration and interruptions of communications (*Di*), the number of hours of geomagnetic storm per year for the period (2015–2021) has been examined.

This period spans the end of solar cycle 24 and the start of cycle 25, and it is associated with (Dst) less than (-50 nT). Because there are more solar active regions visible during this time, it is thought that the majority of intense geomagnetic storms, communication deterioration, and interruptions happen during the maximum phase of the sunspot. In contrast, only a small number of these events are seen during the minimum phase of the sunspot.

Study and evaluation of the monthly Sunspot Number (SSN) (2015 to 2021). Its maximum value is around 838 in the year 2015, and its smallest value is 43 in the year 2019.

After examining the data, we discovered that there was a 120-minute gap between the time (*Di*) at Cairo International Airport on March 17, 2015, and the Super Geomagnetic Storm Dst (-200 nt), also known as the St. Patrick's Day storm, which was the strongest G4 storm of Solar Cycle 24. This event had an impact on the security and safety of Egyptian Air Traffic Management.

When we compared the duration of the second-largest geomagnetic storm, Dst(-200 nt), on June 23, 2015, to the duration of (*Di*) at Cairo International Airport, which was 25 minutes, we saw that this event had a negative impact on the safety and security of Egyptian Air Traffic Management.

Even in other airports, such as but not limited to Aswan International Airport, after ongoing surveillance and follow-up of this Important in Cairo International Airport On March 17, 2015, the airport experienced the same issue as previously described both at once. After comparing the durations of (*Di*) at Aswan International Airport and the Super Geomagnetic Storm Dst (-200 nt), which is known as St. Patrick's Day and lasts 120 minutes, we observed that this event has had an impact on the safety and security of Egyptian Air Traffic Management on March 17, 2015. After comparing the data, we discovered that on June 23, 2015, this event had a negative impact on the security and safety of Egyptian Air Traffic Management.

The duration of (*Di*) at Aswan International Airport was 33 minutes, while the second-largest geomagnetic storm, Dst (-200 nt), was 60 minutes. The main findings of this study suggest a direct association between the first super geomagnetic storm Dst (-200 nt) of solar cycle 24 that occurred on "St. Patrick's day," March 17, 2015, and (*Di*) at Cairo International Airport on March 17, 2015. Communication, navigation, surveillance, and air traffic control will all suffer when there is a satellite solar outage during periods II, a moderate or violent geomagnetic storm, and I during the sunspot cycle's peak. The answer is to be aware of the effects, the potential and consequent risks of electromagnetic storms, and the options available to mitigate those risks.

As a result, decision-makers in the field of aviation should be aware that space-weather phenomena can pose a threat to the safety and efficiency of flight operations. This entails abiding by the relevant business procedures, operational guidelines, and aviation regulations.

VIII. RECOMMENDATIONS

The Egyptian aviation sector is vulnerable to the impacts of space weather, which can affect High-Frequency radio communication, satellites, avionics, and aircraft navigation and communication systems. Internationally, ICAO is requiring that certain standards be developed to assist aircrew and ground support in managing the potential impact of space weather. The main recommendation from this policy brief is that Cairo Air Navigation Center (CANC) should align itself with international for the provision and access to space weather information to be ready to meet the ICAO recommendations by 2025 and to protect the vulnerable areas within aviation systems.

The following recommendations are put forward within this policy brief for consideration:

- Cairo Air Navigation Center (CANC) user forum, with participation from affected parties within the sector should be established to consider and make provision for space weather impacts on aviation.
- Cairo Air Navigation Center (CANC) should be requested to lead the aviation Community in defining and collecting operational data that can be used to assess the different Impact areas, and the economic impact arising from space weather mitigation.
- The aviation industry, with the assistance of the Space weather monitoring Center (SWMC) in Egypt, should be requested to clearly define its requirements for space weather information and how these can be incorporated into the operational decision-making process.
- The Space weather monitoring Center (SWMC) should align itself to deliver space weather information in an internationally agreed-upon standardized format as defined by the aviation user requirements, and be given the mandate to assist the aviation sector in fulfilling the ICAO recommendations.
- The Egyptian Civil Aviation Authority (ECAA) should define a minimum set of requirements for incorporating space weather into operational training for Air Traffic Controllers (ATC), aircrew (pilots and cabin crew), dispatchers, meteorologists, and engineers.
- The Egyptian Civil Aviation Authority (ECAA) should mandate that space weather Information be received by aviation operators and be included as part of their planning and briefing process. This information must meet a minimum set of standards.
- An annual assessment should be carried out of the service performance within the aviation Sector based on space weather events. These recommendations come from an understanding and awareness of the potential impacts of space weather on the aviation sector.

REFERENCE

1. Bom.gov.au. (2019). Space Weather Services website. [online] Available at: https://www.sws.bom.gov.au/.
2. Boroev, R. and Vasiliev, M. (2020a). RELATIONSHIP OF THE ASY-H INDEX WITH INTERPLANETARY MEDIUM PARAMETERS AND AURORAL ACTIVITY IN MAGNETIC STORM MAIN PHASES DURING CIR AND ICME EVENTS. Solar-Terrestrial Physics, 6(1), pp.35–40. doi:10.12737/stp-61202004.
3. Boroev, R. and Vasiliev, M. (2020b). RELATIONSHIP OF THE ASY-H INDEX WITH INTERPLANETARY MEDIUM PARAMETERS AND AURORAL ACTIVITY IN MAGNETIC STORM MAIN PHASES DURING CIR AND ICME EVENTS. Solar-Terrestrial Physics, 6(1), pp.35–40. doi:10.12737/stp-61202004.
4. Borovsky, J.E. and Shprits, Y.Y. (2017a). Is theDst Index Sufficient to Define All Geospace Storms?. Journal of Geophysical Research: Space Physics, 122(11). doi:10.1002/2017ja024679.

5. Cai, X., Burns, A.G., Wang, W., Qian, L., Solomon, S.C., Eastes, R.W., McClintock, W.E. and Laskar, F.I. (2021). Investigation of a Neutral 'Tongue' Observed by GOLD During the Geomagnetic Storm on May 11, 2019. Journal of Geophysical Research: Space Physics, 126(6). doi:10.1029/2020ja028817.
6. Clette, F., Cliver, E.W., Lefèvre, L., Svalgaard, L. and Vaquero, J.M. (2015). Revision of the Sunspot Number(s). Space Weather, 13(9), pp.529–530. doi:10.1002/2015sw001264.
7. Davis, T.N. and Sugiura, M. (1966). Auroral electrojet activity indexAEand its universal time variations. Journal of Geophysical Research, 71(3), pp.785–801. doi:10.1029/jz071i003p00785.
8. Desai, M. and Shah, S. (2018). Impacts of Intense Geomagnetic Storms on NavIC / IRNSS System. Annals of Geophysics, 61(5). doi:10.4401/ag-7856.
9. Filjar, R. (2007). A Study Of Direct Severe Space Weather Effects On GPS Ionospheric Delay. Journal of Navigation, 61(1), pp. 115–128. doi:10.1017/s03734633070044 20.
10. Fisher, G. and Kunches, J. (2011). Building resilience of the Global Positioning System to space weather. Space Weather, 9 (12), p.n/a-n/a. doi:10.1029/2011sw000718.
11. Gonzalez, W.D., Joselyn, J.A., Kamide, Y., Kroehl, H.W., Rostoker, G., Tsurutani, B.T. and Vasyliunas, V.M. (1994). What is a geomagnetic storm? Journal of Geophysical Research, 99 (A4), p.5771. doi:10.1029/93ja02867.
12. Gonzalez, W.D., Tsurutani, B.T. and Clúa de Gonzalez, A.L. (1999). Space Science Reviews, 88(3/4), pp.529–562. doi:10.1023/a:1005160129098.
13. Guo, Y., Li, M., He, S., Xin, P. and Tao, L. (2012). Analysis of the Sun Transit Outage Impact on the Inter-satellite Link of the Navigation Satellite. Lecture Notes in Electrical Engineering, pp.133–143. doi:10.1007/978-3-642-29175-3_13.
14. Joshua, B.W., Adeniyi, J.O., Oladipo, O.A., Doherty, P.H., Adimula, I.A., Olawepo, A.O. and Adebiyi, S.J. (2018). Simultaneous response of NmF2 and GPS-TEC to storm events at Ilorin. Advances in Space Research, 61(12), pp.2904–2913. doi:10.1016/j.asr.2018.03.031.
15. Joshua, B.W., Adeniyi, J.O., Reinisch, B.W., Adimula, I.A., Olawepo, A.O., Oladipo, O.A. and Adebiyi, S.J. (2014). The response of the ionosphere over Ilorin to some geomagnetic storms. Advances in Space Research, 54(11), pp.2224–2235. doi:10.1016/j.asr.2014.08.027.
16. kejian1.cmatc.cn. (n.d.). Space Weather Impacts on Aviation. [online] Available at: http://kejian1.cmatc.cn/vod/comet/spaceweather/aviation_space_wx/print.htm.
17. Kyoto-u.ac.jp. (2022). WDC for Geomagnetism, Kyoto. [online] Available at: https://wdc.kugi.kyoto-u.ac.jp/.
18. Liu, L., Wan, W., Zhang, M.-L., Zhao, B. and Ning, B. (2008). Prestorm enhancements in NmF2and total electron content at low latitudes. Journal of Geophysical Research: Space Physics, 113(A2), p.n/a-n/a. doi:10.1029/2007ja012832.
19. Matzka, J., Stolle, C., Yamazaki, Y., Bronkalla, O. and Morschhauser, A. (2021). The Geomagnetic Kp Index and Derived Indices of Geomagnetic Activity. Space Weather, 19(5). doi:10.1029/2020sw002641.
20. Mendillo, M. (2006). Storms in the ionosphere: Patterns and processes for total electron content. Reviews of Geophysics, 44(4). doi:10.1029/2005rg000193.
21. Mengistu Tsidu, G. and Abraha, G. (2014). Moderate geomagnetic storms of January 22–25, 2012 and their influences on the wave components in ionosphere and upper stratosphere- mesosphere regions. Advances in Space Research, 54(9), pp.1793–1812. doi:10.1016/j.asr.2014.07.029.
22. Penza, V., Berrilli, F., Bertello, L., Cantoresi, M. and Criscuoli, S. (2021). Prediction of Sunspot and Plage Coverage for Solar Cycle 25. The Astrophysical Journal Letters, 922(1), p.L12. doi:10.3847/2041-8213/ac3663.
23. S. O. Ikubanni, S. J. Adebiyi, B. O. Adebesin, O. S. Bolaji, B. J. Adekoya, B. W. Joshua and J. O. Adeniyi (2020). Plasma re-distribution in the African low-latitude ionosphere during intense geomagnetic storms. Journal of the

Nigerian Society of Physical Sciences, pp.228–240. doi:10.46481/jnsps.2020.112.

24. Samed Inyurt (2020). Investigation of Ionospheric Variations During Magnetic Storm Over Turkey. Geomagnetism and Aeronomy, 60(1), pp.131–135. doi:10.1134/s0016793220010120.
25. Space Weather effects on airline operations (Captain Bryn Jones, VAA Cosmic Radiation Project Manager). (n.d.). [online] Available at: https://www.mssl.ucl.ac.uk/cosrad/Website/Publications/SpaceWeatherAL1.pdf.
26. Thales Group. (n.d.). Egypt. [online] Available at: https://www.thalesgroup.com/en/countries/middle-east-africa/egypt [Accessed 6 Aug. 2022].
27. Tsurutani, B.T., Verkhoglyadova, O.P., Mannucci, A.J., Saito, A., Araki, T., Yumoto, K., Tsuda, T., Abdu, M.A., Sobral, J.H.A., Gonzalez, W.D., McCreadie, H., Lakhina, G.S. and Vasyliūnas,
28. V.M. (2008). Prompt penetration electric fields (PPEFs) and their ionospheric effects during the great magnetic storm of 30-31 October 2003. Journal of Geophysical Research: Space Physics, 113(A5), p.n/a-n/a. doi:10.1029/2007ja012879. www.ngdc.noaa.gov. (n.d.). Index of /stp/space-weather/solar-data/solar-indices/sunspot- numbers/group. [online] Available at: http://www.ngdc.noaa.gov/stp/space- weather/solar-data/solar-indices/sunspot- numbers/group/. www.sidc.be. (n.d.). SILSO | World Data Center for the production, preservation and dissemination of the international sunspot number. [online] Available at: http://sidc.be/silso/home. www.spaceweatherlive.com. (n.d.). StackPath. [online] Available at: https://www.spaceweatherlive.com/..
29. Yu, T., Wang, W., Ren, Z., Yue, J., Yue, X. and He, M. (2021). Middle‐Low Latitude Neutral Composition and Temperature Responses to the 20 and 21 November 2003 Superstorm From GUVI Dayside Limb Measurements. Journal of Geophysical Research: Space Physics, 126(8). doi:10.1029/2020ja028427.

This page is intentionally left blank

The 3-Cosmic Framework of the Universe Can Hold Dark Matter and Dark Energy Newidea Research Center

Hsien-Jung Ho

ABSTRACT

To solve the problems of dark matter and dark energy, some cosmologists accept the type of multiverse today. Based on String theory, the Universe's constitution is nine-dimensional space and one-dimensional time and apply "Anthropic Principle" and "Causality" to deal with space and time, that takes 4-dimensional spacetime as one Cosmos as we known world, therefore, there is a 3-cosmic framework of the Universe, which has triple Cosmoses in the whole space. Between any two Cosmoses, except gravitational force, there is no other fundament force that implying dark matter is in the other Cosmoses than ours.

Exploring dark matter from the interior of the Earth, a dark planet was found, which is about 1.33 times of Mars inside the Earth but in the other Cosmos. Chandler wobble should confirm the existence of the dark planet. Based on the data of cosmological parameters from 1-year WMAP results to Planck Satellite 2018 results, dark energy gradual decreasing, but the total matter gradual increasing at the same value.

Keywords: string theory, triple cosmoses, dark matter, dark energy, chandler wobble.

Classification: DDC Code: 523.84465 LCC Code: QB843.S95

Language: English

London Journals Press

LJP Copyright ID: 392922
Print ISSN: 2631-8474
Online ISSN: 2631-8482

London Journal of Engineering Research

Volume 22 | Issue 8 | Compilation 1.0

The 3-Cosmic Framework of the Universe Can Hold Dark Matter and Dark Energy Newidea Research Center

Hsien-Jung Ho

ABSTRACT

To solve the problems of dark matter and dark energy, some cosmologists accept the type of multiverse today. Based on String theory, the Universe's constitution is nine-dimensional space and one-dimensional time and apply "Anthropic Principle" and "Causality" to deal with space and time, that takes 4-dimensional spacetime as one Cosmos as we known world, therefore, there is a 3-cosmic framework of the Universe, which has triple Cosmoses in the whole space. Between any two Cosmoses, except gravitational force, there is no other fundament force that implying dark matter is in the other Cosmoses than ours.

Exploring dark matter from the interior of the Earth, a dark planet was found, which is about 1.33 times of Mars inside the Earth but in the other Cosmos. Chandler wobble should confirm the existence of the dark planet. Based on the data of cosmological parameters from 1-year WMAP results to Planck Satellite 2018 results, dark energy gradual decreasing, but the total matter gradual increasing at the same value.

This phenomenon accords with the narration of the Big Bang Theory; therefore, we should take the current dark energy as the residual energy of the Universe today after the Big Ban. According to the data, cold dark matter density increases gradually about 4.3%, which implies to be in the high-energy-density Cosmoses, comparing to baryon density increasing gradually about 0.5%, which is in our low-energy-density Cosmos.

Because the high-energy-density Cosmoses rapidly expands, its matter (dark matter) should subject to a "drag" on the stars of our Cosmos that causes the effect of pulling our Cosmos accelerating expansion. From this study, the problems of dark matter and dark energy in astrophysics may be roughly solved.

Keywords: string theory, triple cosmoses, dark matter, dark energy, chandler wobble.

Other writings of paper

Ho, Hsien-Jung, *1993*. Reconstruction of the Earth Model and Discovery of the Interior Dark Matter, *First Symposium on UFO cross-strait. China Ufology Institute*. http://newidea.org.tw/pdf/S2.pdf.

Ho, Hsien-Jung and Hsui, Haw-Ping Peter, 2005. Mega-Tsunami in Northeastern Taiwan At Least 12,000 Years Ago, *3rd International Conference on Asian and Pacific Coasts 2005,* Hanrimwon Publishing Co. Seoul Korea, p. 199-208. http://newidea.org.tw/pdf/S4.pdf.

Ho, Hsien-Jung, 2019. Based on spacetime of String theory exploring dark matter inside the Earth, *Journal of Scientific and Engineering Research*, 2019, 6(8):166-191. http://newidea.org.tw/pdf/S71.pdf.

I. INTRODUCTION

In 1922, Kapteyn the first astronomer addressed the possible existence of invisible matter in the Milky Way Galaxy by using stellar velocities [Kapteyn 1922]. Then some scientists, Oort (1932), Zwicky (1937), Bartusiak (1988), Stsrobinskii and Zel'dovich (1988), found unobservable matter, which was called dark matter, amounted to more than 90 % mass of the entire Universe.

In 2006, astronomers used Chandra X-ray Observatory to observe the Bullet Cluster of galaxies and found a recent big collision of two galaxy clusters, by separating dark matter from

normal matter, that is direct evidence of the existence of dark matter [Clowe *et al.* 2006]. The dark matter is real that can only be detected by its gravitational influence on visible matter. While almost all astronomers agree on the existence of the dark matter; however, after one hundred years of search, there is nothing gained.

In 1998, the High-Z Supernova Search Team published observations of type 1a supernova as standard candles [Riess *et al.* 1998], and in 1999 the Supernova Cosmology Project followed immediately [Perlmutter *et al.* 1999], then the two independent projects obtained results suggesting a totally unexpected acceleration in the expansion of the Universe. To explain the phenomenon of the Universe is expanding at an accelerating rate, "dark energy" is the most accepted hypothesis to the observations. Dark energy acts as a sort of an anti-gravity and is responsible for the present-day acceleration of the Universal expansion.

From 2003 to 2020, the Wilkinson Microwave Anisotropy Probe (WMAP), and the Planck Satellite have released their measurements with the content of the present-day Universe, roughly there are dark energy about 68%, dark matter about 27%, and the rests — everything ever observed with all our instruments and all normal matter — add up to about 5%.

Dark energy is a current scientific hypothesis, being neither matter nor radiation, its physical properties have no clue, and we don't know how it works, and dark matter is also no solution, so, now all astrophysicists take them as the major Conundrums. As the names of dark matter and dark energy are all come from astrophysics, we try String theory of theoretical physics to solve the major problems of science.

1.1 Based on String Theory there is 10-Dimensional Spacetime in the Universe

String theory describes all fundamental forces and forms of matter and potentially provides a unified description of gravity and particle physics. Based on String theory, the Universe's constitution are nine-dimensional space and one-dimensional time, that is interpreted as the product of ordinary 4-dimensional spacetime, and 6-extra-dimensional space, but 6-extra-dimensional spaces is yet unobserved [Scherk & Schwarz 1975]. physicists have attempted to compactify the ten-dimensional spacetime model through spontaneous symmetry breaking down to a four-dimensional one as our known world and the other 6-extra-dimensional space, which is compacted to be tiny space. Because of no exact boundary condition to fit the real Universe and works out a theoretically solid basic geometry, therefore no proposed method meets perfection.

Without considering compaction, nine-dimensional space should be symmetrical, i.e., symmetrical with the same weight for each dimension of space. Therefore, the Universe should still exist in equal weight of nine-dimensional space, plus one-dimensional time, so it can be argued that String theory of the cosmic framework should still be able to maintain a complete ten-dimensional spacetime.

In the multidimensional theories of String theory, the force of gravity is the only fundamental force with effect across all dimensions. This explains the relative weakness of gravity compared to the other fundamental forces (as electromagnetic force), which cannot cross into extra dimensions.

In that case, dark matter could exist in extra dimensions that only interact with the matter in our space through gravity. That dark matter could potentially aggregate in the same way as ordinary matter, forming extra-dimensional galaxies [Siegfried, 1999].

Dvali suggested that the extra dimensions of space do not curl up become minimum, but infinite in size and uncurved, just like our ordinary three-dimensional view. Character in String theory, they rethink the "extra dimensions" problem, that are, gravity can roam to any additional dimension of space. They think that the accelerated expansion of the Universe is not caused by dark energy, but because gravity leaks out of our world. In particular, the theory predicts that the Universe has extra dimensions into which gravity, unlike ordinary matter, may be able to escape. This leakage would warp the spacetime continuum and cause cosmic expansion to

accelerate. Thus, the extra dimensions need not be small and compactify, but may be large extra dimensions [Dvali 2004], i.e., outside our ordinary three-dimensional space, there are the same six extra dimensions of other space usually in the Universe.

1.2 Some Cosmologists Accept This Type of Multiverse Today

In 1957, Everett devised "the many-worlds interpretation (MWI)" of quantum mechanics. The core of the idea was to interpret in the quantum world, an elementary particle, or a collection of such particles, can exist in a superposition of two or more possible states of being [Everett 1957].

In the 1980s, Susskind said that it was the result of string theory, which was used as a tool or framework to describe cosmic phenomena [Susskind 2006]. MWI is a theory of multiple Universes. In this case, scientists can come up with the only explanation: these elementary particles do not exist only in our Cosmos; it may also fly around the other Cosmoses that are not ours. This means that there may be multiple Cosmoses, called multiverse, in space, but there are only subtle differences between them, so there are still the Cosmoses that we do not know about.

An important aspect needs to extend our physical theories within a multiverse framework. The dominant expectation so far for the theory of quantum gravity (QG) has been the 'reductionist' hope that relies on QG producing one unique solution that resembles the general features of our Universe, but scientists have failed. The three different and important theories: quantum mechanics, String theory and inflation, all predict the existence of the multiverse is, scientists believe, hardly coincidental. The existence of the multiverse must be expected from the underlying fundamental theory.

Deutsch is one of the leading figures in theoretical physics in the multiverse. He believes that this multiverse theory is the only explanation for the strange phenomenon in quantum mechanics, because it is based on rigorous mathematical equations and many experimental results [Deutsch 2010]. Although more than 50 years have elapsed since the first discussion of the "many worlds" by Everett, there is not any new step to set the foundations and the ontology of the multiverse and of this new field in physics.

1.3 The Universe Should Be a 3-Cosmic Framework From Causality and Anthropic Principle

Without compactifying the nine-dimensional space of the Universe, bases on ten-dimensional spacetime of String theory that is considered to universally exist. According to "Causality", an effect cannot occur before its cause, which means time has one direction and cannot be divided into some different parts. So one-dimensional time is taken as a common standard in order of event in the Universe.

According to "Anthropic Principle", which is the simple fact that we live in a Universe set up to allow our existence. It means that 3-dimensional space and 1-dimensional time, called 4-dimensional spacetime, are taken as one Cosmos as our living world. Therefore, the 9-dimensional space can be divided into three portions, and each portion has a common standard time. It means there is a 3-cosmic framework in the Universe, called triple Cosmoses; in other word, the Universe contains three Cosmoses, which locate in the same nine-dimensional space of the Universe, but cannot be observed directly with each other.

According to String theory, a 3-cosmic framework of the Universes has characteristics in which our Cosmos describes the world of general matter as we know, but the others describe another world, which we know nothing. Among any other Cosmoses, there is no fundamental forces except gravity; in other words, the graviton in the field of gravity can penetrate all three Cosmoses; however, the light (electromagnetic wave) cannot that means the dark matter should be situated in the Cosmoses other than ours.

According to this 3-cosmic framework of the Universe, there are triple Cosmoses in the whole space, namely 1st Cosmos, 2nd Cosmos and 3rd Cosmos, used U1, U2, and U3 instead. In the

3-cosmic framework of the Universe, there is no fundament force exists between any two Cosmoses, except gravitational force, i.e., Cosmoses cannot observe directly with each other that is the characteristic of dark matter. So, the dark matter, which will be found through the gravity, should be in invisible Cosmoses other than ours.

U_1 : 1st Cosmos

U_2 : 2nd Cosmos

U_3 : 3rd Cosmos

U_1X : X axle of 1st Cosmos

U_1Y : Y axle of 1st Cosmos

U_1Z : Z axle of 1st Cosmos

U_2X : X axle of 2nd Cosmos

U_2Y : Y axle of 2nd Cosmos

U_2Z : Z axle of 2nd Cosmos

U_3X : X axle of 3rd Cosmos

U_3Y : Y axle of 3rd Cosmos

U_3Z : Z axle of 3rd Cosmos

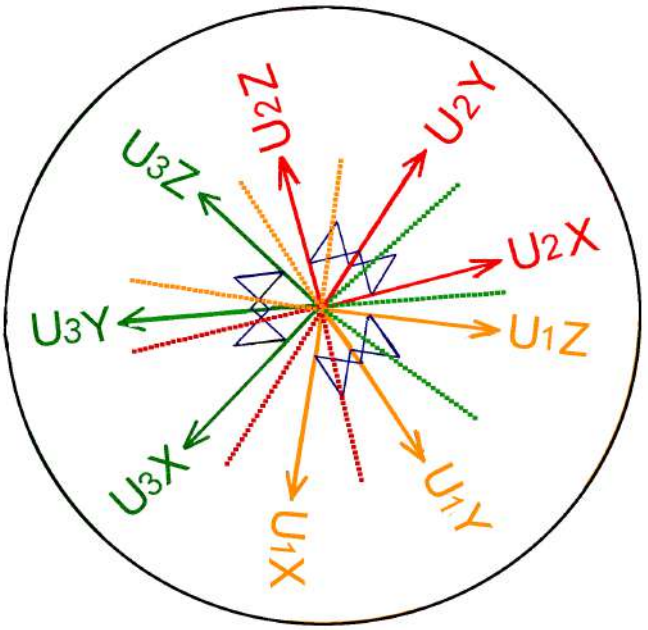

Figure: This is the imitation schematic diagram of nine-dimensional space in a 3-cosmic framework of the Universe. All the 3 Cosmoses (U_1, U_2, and U_3) exist, but none of fundamental forces can affect with each other except gravity; for example, if U_1 is our Cosmos, we cannot observe U_2 and U_3. The deep blue lines denote 3 axles, X, Y and Z, all perpendicular to each other in each Cosmos. In the diagram, the center of circle is assumed a point P, which has 9 coordinates: U_1Xp, U_1Yp, U_1Zp, U_2Xp, U_2Yp, U_2Zp, U_3Xp, U_3Yp and U_3Zp in the Universe. Assuming a star at P position, which appears in our Cosmos, the other Cosmoses cannot observe the star, its coordinates ordinarily are denoted by Xp, Yp and Zp.

1.4 The Map of Microwave Background Radiation Fluctuations Maybe Showed the Hard Evidence of Another Cosmos

June 2001, NASA launched WMAP, which is designed to detect the residual cosmic radiation heat in the Universe after the Big Bang and drew the full map of microwave background radiation fluctuations throughout the Universe. In 2009, European Space Agency's partnership with NASA launched Plank Satellite, which can detect tiny temperature fluctuations in this radiation, then a cosmic microwave background radiation fluctuation map was drawn more accuracy.

In general, scientists tend to think that the radiation is evenly distributed, but the full map shows a different fact — there is a powerful center in the sky in the southern half of the map and a seemingly hole-like "cold spot" that cannot be explained by existing physics knowledge, where galaxies are accelerating away [Rudnick *et al.* 2007].

From the anomaly some scientists propose perspectives of the multiverse to explain the cold spot. The scientist predicted String theory does not predict a unique Universe, on the contrary, it predicts a multiverse [Mersini-Houghton 2008].

In 2005, scientists predicted that anomalies in radiation existed that can only have been caused by the gravitational pulling on our Cosmos from

others as it formed during the Big Bang [Woit 2013]. The "cold spot" in the southern half the map of the Universe may be the first "hard evidence" of another Cosmos than ours that exist has been found by scientists [Leake 2013].

1.5 Exploring Dark Matter From the Interior of the Earth

Based on String theory and the 3-cosmic framework of the Universe, we can find the dark matter in the other Cosmoses than ours. The best method of exploring dark matter is to start from the Earth where we live. In 2019, we published a research article “Based on the Spacetime of String Theory Exploring Dark Matter Inside the Earth” [Ho 2019]. The part of its abstract is as follow.

According to the characteristics of the Earth's interior, equitably examining its constitution, temperature, density, and pressure from a different view of the core, the special arguments are put forward. It is inferred that the solid rock and the magma change states interactively at the Crust-Mantle Boundary (CMB). In the low viscosity F-layer of outer core, high temperature causes some elements and oxides of magma to undergo oxidation-reduction reactions and separate due to its gravity. The great number of heats, produced from radiogenic heat, chemical reaction heat and nuclear fission heat, become the power sources for the geo-dynamo of great convection cell, which are the flows of the magma and the solid rock migrating up to the crust and down across the CMB to the F-layer.

Based on the new conception and applying a simplified method tries the different density distribution curves of models in the core to calculate the data of the Earth and compared with the existing current data of the Earth. The insufficient mass and moment of inertia belong to the missing objects, taken as the parts of dark matter, which may be in the interior of the Earth, and then evaluate the Earth's mass and moment of inertia that are found to be only 85.73% mass and 94.82% moment of inertia of the current data. By the two insufficiencies of the Earth's data, formulating the reasonable assumptions, a planet of dark matter inside the earth has been figured out. And then calculate gravity and pressure in every depth within the Earth to check suitability or not. Finally, a dark planet, radius 3700.375 km about 1.33 times of Mars, exists reasonably inside the Earth but in another Cosmos than ours.

1.6 Chandler Wobble Conforms a Dark Planet Inside the Earth but in the Other Cosmos

It is hard to examine the existence of the dark matter directly; however, that can be recognized from Chandler wobble. Referring to the orientation of the rotation axis of the Earth in space in addition to both precession and nutation, there is a wobble on the instantaneous axis of rotation of the Earth itself. The wobble alters the position of a point on the Earth relative to the pole of rotation. In 1891, Chandler pointed out that there are two different kinds of the wobble periods. One is a period of 12 months, and the other is a period of 433 days, about 14 months [Chandler 891]. The former, called annual wobble, is obviously affected by the seasonal climate. The latter, called Chandler wobble, has not been solved the problem for more than one hundred years. The Chandler wobble is a small deviation that amounts to change of about 9 meters at the point in the surface of the rotation axis of the Earth.

In 2000, Gross found that two-thirds of the Chandler wobble was caused by fluctuating pressure on the seabed. The remaining third is due to atmospheric fluctuations. The wobble, in fact, produces a very small ocean tide with an amplitude of approximately 6 mm, called a "pole tide" [Gross 2000]. While it must be maintained by changes in the mass distribution or angular momentum of the Earth's outer core, atmosphere, oceans, or crust, for a long time the actual source was unclear, since no available motions seemed to be coherent with what was driving the wobble.

It is inferred from the phenomenon in which the same side of the Moon always faces the Earth that means the Moon and the Earth rotate synchronously. The same phenomenon will happen to the Earth and the dark planet that both rotate synchronously, but the rotation axes of both are impossible coinciding with each other; in

other words, an angle between the two rotation axes produces the Chandler wobble as the precession and nutation because of the Sun and the Moon on non-parallel rotation axes with the Earth's. Therefore, the effect of Chandler wobble may confirm the existence of a dark planet inside the Earth but in the other Cosmos.

1.7 According to "The Big Bang Theory" Dark Energy Should Be the Residual Energy of the Universe Today

In 1930s, Lemaître proposed "The Big Bang Theory". In the beginning of the Big Bang, the Universe were made up of very high temperature and hot energy with uniformity and isotropy, but no matter (Lemaître 1927). When this hot energy expands very quickly outwards, an exponential inflation occurs [Guth 1982]. As the Universe expands rapidly and temperature decreases, the distribution of energy changes slightly, according to Einstein's famous equation ($E=MC^2$) for energy and mass interchange gradually, creating the earliest substances. In 1964, the discovery of Cosmic Microwave Background by Radio astronomers Penzias and Wilson was the most important evidence to test the Big Bang Theory [Penzias & Wilson 1965]. Then more and more astronomical and physical evidence came out, such as Cosmic Background Explorer (COBE) [Bennet 1993], WMAP and Planck Satellite, when their detected spectrum was measured to map its black body radiation curve, the Big Bang Theory became more complete, and scientists believed in it.

In 2018, plank satellite detects tiny temperature fluctuations in the radiation of the Universe.

These distributions of fluctuation reflect the baryon density of the Universe before galaxies have yet to form. Normal matter from galaxies and stars accounts for only 4.94 % of the Universe's composition, with the rest missing substance, including dark matter, which accounts for 26.57 %, and mysterious dark energy, which accounts for 68.34% [Aghanim *et al.* 2020].

Dark energy is one of the most mysterious observations in physics today. To research dark energy, we apply the table of cosmological parameters of WMAP results and Planck Satellite results, whose Hubble constants nearly gradually decrease, are selected one set at each detection, and are showed as the following.

The table of cosmological parameters from WMAP and Planck Satellite

Parameter	Source Symbol	1-year WMAP [Spergel 2003]	3-year WMAP [Spergel 2007]	5-year WMAP [Komatsu 2009]	7-year WMAP [Komatsu 2011]	9-year WMAP [Bennett 2013]	Planck 2013 [Ade 2014]	Planck 2015 [Ade 2016]	Planck 2018 [Aghanim 2020]
Hubble constant ($100h$ Mpc^{-1} km s^{-1})	H_o	71.0	704	70.5	70.2	70.0	68.14	67.31	67.32
Physical baryon density	$\Omega_b h^2$	0.0224	0.02186	0.02267	0.02255	0.02264	0.022242	0.02222	0.02238
Physical cold dark matter density	$\Omega_c h^2$	–	–	0.1131	0.1126	0.1138	0.11805	0.1197	0.12011
Physical Matter density	$\Omega_m h^2$	0.135	0.1324	0.1358	0.1352	0.1364	–	0.1426	0.14314
Dark energy. density/Critical density	Ω_Λ	73.22%	73.2%	72.6%	72.5%	72.1%	69.64%	68.5%	68.42%
Matter density/Critical density	Ω_m	26.78%	26.8%	27.32%	27.43%	27.9%	30.36%	31.5%	31.58
Baryon density/Critical density	Ω_b	4.44%	4.41%	4.56%	4.58%	4.63%	4.79%	4.9%	4.94%
Cold dark matter density/Critical density	Ω_c	22.34%	22.39%	22.8%	22.9%	23.3%	25.43%	26.42%	26.64%
Age of the Universe (Gyr)	t_o	13.70	13.23%	13.72	13.76	13.74	13.784	13.80	13.80

From the table, the dark energy density Ω_Λ from 1-year WMAP results to Planck 2018 results, the value from 73.22% decreases gradually down to 68.42%, decreasing 4.8%. But the total matter density Ω_m from 1-year WMAP results to Planck 2018 results, the value from 26.78% increases gradually up to 31.58%, increasing 4.8%. As the Universe expands rapidly, the temperature drops, gradually cools down, then energy transforms into the building blocks of matter. From the table, dark energy transforms into matter at the same percentage of the Universe's content, that is consistent with the narration of the Big Bang Theory.

The Planck 2018 results VI cosmological parameters are taken as the current situation of the Universe. We may imagine that at the firstly time of the Big Bang, the full energy (100% energy density) of the Universe gradually loses, after 13.8 billion years later, remains 68.42% energy density, which is called dark energy density, and creates 31.58% total matter density, so we should take the current dark energy as the residual energy of the Universe today.

1.8 The 3-Cosmic Framework of the Universe Can Also Hold Dark Energy

After the Big Bang, 68.42% dark energy density Ω_Λ is remainder today, but the lost 31.58% dark energy density transforms into matter density Ω_m, which contains 4.94 % baryon (normal matter) density Ω_b in our Cosmos and 26.57 % cold dark matter density Ω_c in other spaces than ours and 0.15% others as massive neutrinos density Ω_ν.

According to the table of Cosmological Parameters from 1-year WMAP results to Planck

2018 results, cold dark matter density Ω_c from the value 22.34% increases gradually up to 26.64%, increasing 4.3%, and baryon density Ω_b in our Cosmos from the value 4.44% increases gradually up to 4.94%, only increasing 0.5%, which compares to increasing rate of cold dark matter density Ω_c about 1:8.6. Because matter transforms from energy after Big Bang, the Ω_b increasing value is so small that indicates energy in our Cosmos very poor. Temperature is a display of the thermal motion of microscopic particles, therefore hot energy must display its high temperature. After WMAP and Planck Satellite detected, the current actual temperature of CMB is 2.725 Kelvin, that is very close to the absolute zero (0°K = −273.15℃), therefore, energy is also poor that cannot contribute to expand of our Cosmos at an accelerating rate.

Under the 3-cosmic framework of the Universe, the rate of expansion in a high-energy-density Cosmos will be much higher than that of a low-energy-density Cosmos as ours. According to the property of fundamental interaction forces, except gravitational force, the other fundamental forces (including strong nuclear force, weak nuclear force, and electromagnetic force) cannot penetrate into the other Cosmoses, therefore, the energy of one Cosmos cannot affect another Cosmos. So, the high-energy-density Cosmos cannot directly contribute to the expansion of our low-energy-density Cosmos. But when the high-energy-density Cosmos rapidly expands, its matter (i.e., dark matter) will expand at the same pace. From the data of 2018 Planck result, there is only normal matter 15.64% of total matter in our Cosmos, however there are large amounts of dark matter 84.36% in other Cosmoses, which use gravity to drag on the stars of our Cosmos away at an accelerated pace, that causes the effect of pulling our Cosmos accelerating expansion.

II. DISCUSSION AND RESULT

1. In classical physics, matter is made up of particles, which are entities that conform to a simple orbit, and can calculate their motion, velocity, angle, and speed at any one time, for example, an elementary particle in atom — electron, in Newton's classical mechanics, rotates around the nucleus in a circular orbit, and the position, momentum and orbit of each particle are fully predictable, and it is only in a single place at the same time. This idea is like the case in our solar system, but beginning in the 1920s, it is known from quantum experiments that in the atomic structure, each electron surrounds the nucleus, not in a stable orbit, but appears intermittently in different places, which can only be counted by probability or statistics; in other words, the elementary particles do not have a purely exact position. The only explanation is that these particles exist not only in our Cosmos, but also shave other Cosmoses, indicating the existence of multiverse in space.
2. Energy causes the Universe expansion because of its high temperature, but matter makes each other's shrinkage because of the gravity, however, current 68.42% dark energy density is bigger than 31.58% total matter density about 36.84%, therefore, this much dark energy certainly will put the Universe rapid expansion. According to the Big Bang Theory, dark energy will decrease gradually down, but matter increases gradually up, when dark energy deceases to below 50% or less, and total matter increases to bigger than 50% or more, the Universe may stop to expand, and turn around to collapse in a "Big Crunch" due to the gravity.
3. From this study, the hypothesis of the 3-cosmic framework of the Universe maybe enables a new way to deal with some problems in astrophysics as following:

3.1 An invisible companion star of Cygnus X-1 may be a dark matter

In 1979, Stokes and Michalsky detected that Cygnus X-1 is a hot super giant star orbited by an invisible companion star in a period of 5.6 days.

Its mass can be estimated from the Doppler shifts in the spectrum of the visible super giant star. The mass of Cygnus X-1 is about nine times of the Sun [Stokes & Michalsky 1979]. In 1990, when astronomers Kippenhahn and Weigert observed Cygnus X-1 star, they saw that its interior was like the normal planet, but when they observed its

motion, and found an invisible companion star about eight times the mass of the Sun, orbiting it [Kippenhahn & Weigert 1990].

Far from the maximum mass of a neutron star or a white dwarf, and in the optical identification and some other doubtful points, the companion star is considered not to be a black hole, but gravity affects the operation of Cygnus X-1 star. If we consider the companion star of Cygnus X-1 maybe a dark matter in the Cosmos other than ours, and its gravity affects Cygnus X-1, the problem should be solved.

3.2 Dark matter may be in Hyades supercluster

In 1993, when Casertano and colleagues observed the Hyades cluster in Taurus's orientation, they discovered hundreds of stars that did not belong to this star cluster, known as the Hyades group, and synchronized around the center of the Milky Way. A local mass enhancement of at least (5～10) $\times 10^5$ solar masses, with a radius of about 100 parsec, can trap stars with an origin related to that of the Hyades cluster and explains the excess of stars with velocities near the Hyades velocity that constitutes the Hyades supercluster. Part of this mass enhancement can be in visible stars, but a substantial fraction is likely to be in the form of dark matter. According to the theory of star cluster generation, the Hyades group has been able to develop into the spherical distribution that we can observe today. The results are calculated, and it claims to have a large cluster of dark matter, about a few hundred light-years in diameter, running in synchronization with Hyades clusters in the solar system, which is only about 150 light-years old [Casertano *et al.* 1993].

This dark matter should be in another Universe than ours.

3.3 The existence of a dark planet X can solve some problems in solar system

From old data of Comet Halley's period scientist predicted an invisible planet X [Brady 1971, 1972].

A proposed dark planet X may affect the motion of Neptune and Uranus [Flandern 1981; Anderson 1988]. Pioneer 10 and 11 was pulled back to the direction of the Sun [Anderson *et al.* 2002]. If we consider a dark matter X, which orbits around the Sun in the other Cosmos than ours, then its gravity will sometimes affect the motion of Halley's Comet, Neptune, Uranus, Pioneer 10 and 11 spacecrafts, therefore, the problem of the invisible object may be solved, and that can solve some problems of astronomical observation.

III. CONCLUSION

Based on the applications of ten-dimensional spacetime of String theory, the 3-cosmic framework of the Universe should enable a new way to break the bottleneck of research in the space of the Universe. According to the data, from 1st year WMAP results (2003) to Planck Satellite 2018 results, cold dark matter density increases gradually about 4.3%, which implies to be in the high-energy-density Cosmoses, comparing to baryon density increasing gradually about 0.5%, which is in our low-energy-density Cosmos.

Because the high-energy-density Cosmoses rapidly expands, its matter (dark matter) should subject to a "drag" on the stars of our Cosmos that causes the effect of pulling our Cosmos accelerating expansion.

From this study, the problems of dark matter and dark energy in astrophysics may be roughly solved as above, but that still needs to be proved by the fine outcomes of physicists' new research.

REFERENCES

1. Anderson, John, 1988. Planet X - Fact or Fiction? *Planetary Report*, 8, (4), 6-9.
2. Anderson, John D. *et al.*, 2002. Study of the anomalous acceleration of Pioneer 10 and 11, *Phys. Rev.* D65: 082004, LA-UR-00-5654.
3. Bartusiak, Marcia, 1988. Wanted: Dark Matter, *Discover*, Dec. 1988. p. 63-69.
4. Bennet, C. L. *et al.,* 1993. Scientific results from the Cosmic Background Explorer, *PNAS* 1993 Jun 1; 90, (11): 4766-4773.
5. Bennett, C. L., *et al.*, 2013. Nine-Year Wilkinson Microwave Anisotropy Probe (WMAP) Observations: Final Maps and Results, *The Astrophysical Journal Supplement Series,* Volume 208, Number 2. P.

46, Table 17. Cosmological Parameter Summary (WMAP).
6. Brady, Joseph L., 1971. The orbit of Halley's Comet and apparition of 1896, *Astronomical Journal,* 76, No. 8. 728-739.
7. Brady, Joseph L., 1972.The Effect of Trans-plutonian Planet on Halley's Comet. *Publication of the Astronomical Society of the Pacific*. 34. No. 498, 314-322.
8. Caetano, S., Iben, I. and Shilds, A., 1993.The Hyades Cluster-Supercluster Connection: Evidence for a Local Concentration of Dark Matter, *Astrophysical Journal*. Part 1, 410, 90-98.
9. Chandler, S. C., 1891. On the variation of latitude, *Astronomical Journal*, 11, 59-61, 65-70.
10. Clowe, Douglas; Bradac, M., Gonzalez, A. H. *et al.,* 2006. A direct empirical proof of the existence of dark matter, *Astrophys J Lett*., 648 (2): L109-L113.
11. Deutsch, David, 2010. Apart from Universes /Many Worlds? Everett, Quantum Theory, and Reality, In S. Saunders; J. Barrett; A. Kent; D. Wallace (eds.), *Oxford University Press*. pp. 542-552.
12. Dvali, Georgi, 2004. Out of the Darkness, *Scientific American*, February 2004, 68-75.
13. Everett, Hugh, 1957. Relative State Formulation of Quantum Mechanics. *Reviews of Modern Physics*. 29, 454-462.
14. Flandern, T.V., 1981. The renewal of the Trans-Neptunian planet search, *Bulletin of the American Astronomical Society* 12, 830.
15. Gross, Richard S., 2000. The Excitation of the Chandler Wobble, *Geophysical Research Letters*, 27, (15), 2329-2332.
16. Guth, Alan H., 1982. Fluctuation in the New inflationary, Physical Review Letters, Volume 49, Number 15, 1110-1113.
17. Ho, Hsien-Jung, 2019. Based on the Space-Time of String Theory Exploring Dark Matter inside the Earth, *Journal of Scientific and Engineering Research*, 2019, 6(8):166-191.
18. Kapteyn, Jacobus Cornelius, 1922. First attempt at a theory of the arrangement and motion of the sidereal system, *Astrophysical Journal,* 55: 302-327.
19. Kippenhahn, Rudolf and Weigert, Alfred, 1990. Stellar Structure and Evolution, *Springer Publishing House*, Berlin.
20. Komatsu, E., *et al.*, 2009. Five-Year Wilkinson Microwave Anisotropy Probe (WMAP) Observations: Cosmological Interpretation, *The Astrophysical Journal Supplement Series*, Volume 180, p. 371, Table 14. Comparison of ΛCDM Parameters from WMAP+BAO+SN with Various SN Compilations (Union).
21. Komatsu, E., *et al.*, 2011. Seven-Year Wilkinson Microwave Anisotropy Probe (WMAP) Observations: Cosmological Interpretation, *the Astrophysical Journal Supplement Series*, Volume 192, Number 2. p.3, Table 1. Summary of the Cosmological Parameters of ΛCDM Model (WMAP+BAO+H_0 Mean).
22. Leake, Jonathan, 2013. Cosmic map reveals first evidence of other universes, *The Sunday Times,* 19 May 2013.
23. Lemaître, Georges, 1927. Un Univers homogène de masse constante et de rayon croissant rendant compte de la vitesse radiale des nébuleuses extra-galactiques, Annales de la Société Scientifique de Bruxelles, A47, p. 49-59.
24. Mersini-Houghton, Laura, 2008. Birth of the Universe from the Multiverse, *Department of Physics and Astronomy of North Carolina University*, September 22, 2008.
25. Oort, Jan H., 1932, The force exerted by the stellar system in the direction perpendicular to the galactic plane and some related problems, *Bulletin of the Astronomical Institutes of the Netherlands,* Vol. 6, p. 249-287.
26. Penzias, A. A. and Wilson, R.W., 1965. A Measurement of Excess Antenna Temperature at 4080 Mc/s. *Astrophysical Journal,* 142: p. 419-421.
27. Perlmutter, S. *et al.* 1999. Measurements of Ω and Λ from 42 High-Redshift Supernovae, *The Astrophysical Journal*, Volume 517, Number 2, 517, 565-586.
28. Planck Collaboration: Ade, P. A. R. *et al.*, 2014. Planck 2013 results. I. Overview of products and scientific results, *Astronomy &*

Astrophysics, Volume 571, A1, Table 10. Cosmological parameter values for the Planck-only best-fit 6-parameter ΛCDM model and for the Planck best-fit cosmology including external data sets, Planck (CMB + lensing), Best fit.
29. Planck Collaboration: Ade, P.A.R., *et al.*, 2016. Planck 2015 results. XIII. Cosmological parameters, *Astronomy & Astrophysics,* Volume 594, A13, p. 32, Table 4. Parameters of the base ΛCDM cosmology computed from the 2015 baseline Planck likelihoods (Planck TT+ low P).
30. Planck Collaboration: Afghanis, N., *et al.*, 2020. Planck 2018 results. VI. Cosmological parameters, *Astronomy & Astrophysics*, Volume 641, A6, p. 7, Table 1. Base-ΛCDM cosmological parameters from Planck TT,TE,EE+lowE+lensing. (Plik best fit).
31. Rise's, Adam G. *et al.,* 1998. Observational Evidence from Supernovae for an Accelerating Universe and a Cosmological Constant, *The Astronomical Journal,* Volume 116, Number 3, 116 1009.
32. Rudnick, Lawrence; Shea Brown, Liliya R. Williams, 2007. Extragalactic Radio Sources and the WMAP Cold Spot, *The Astrophysical Journal,* Volume 671, Number 1, 40.
33. Scheck, J. and Schwarz, J.H., 1975. Dual field theory of quarks and gluons, *Physics Letters*, 57, B, 463-466.
34. Siegfried, T., 1999. Hidden Space Dimensions May Permit Parallel Universes, Explain Cosmic Mysteries. *The Dallas Morning News*, 5 July 1999.
35. Sparge, D.N., *et al.*, 2003. First Year Wilkinson Microwave Anisotropy Probe (WMAP) Observations: Determination of Cosmological Parameters, *The Astrophysical Journal Supplement Series*, Volume 148, No 1, p. 175-194, Table 10. Basic and Derived Cosmological Parameters: Running Spectral Index Model.
36. Spergel, D.N., *et al.,* 2007. Three-Year Wilkinson Microwave Anisotropy Probe (WMAP) Observations: Implications for Cosmology, *The Astrophysical Journal Supplement Series*, Volume 170, p. 380, Table 2. Power-Law CDM Model Parameters and 68% Confidence Intervals, 3 Year + ALL Mean.
37. Stokes, G.M. & Michalsky, J.J., 1979. Cygnus X-1. Genus: X-ray binary, species: black hole? *Mercury* 8, p. 60-61.
38. Stsrobinskii A.A. and Zel'dovich, Za. B., 1988. Quantum Effects in Cosmology, *Nature* 331, 25.
39. Susskind, Leonard, 2006. Father of String Theory Muses on the Megaverse. *The New York Academy of Science Publications*, April 14, 2006.
40. Woit, Peter, 2013. The "Dark Flow" & Existence of Other Universes —New Claims of Hard Evidence, *New Scientist*, June 03, 2013.
41. Zwicky, F., 1937. On the Masses of Nebulae and of Clusters of Nebulae. *Astrophysical Journal*, 86, 217.

This page is intentionally left blank

GPU Accelerated Numerical Simulation of Local Scours Near Hydraulic Structures

Vladimir Prokofev

ABSTRACT

A module of sediments transport allowing to simulate the dynamics of local bed scours in proximity to hydraulic structures has been integrated into the three-dimensional non- hydrostatic multilayer open flow model. The sediment transport calculation is performed based on the formulas that apply the value of bed-shear stress. The slope slide in the scour hole and the alteration of the critical shear stress depending on the local bed inclination and flow speed direction are taken into account. This numerical model has been implemented completely by means of a GPU which allows to perform complicated 3D calculations within a reasonable time period. The results of testing performed based on the publicly available experimental data are given: comparison of the dynamics of bed transformation behind the apron as influenced by jet current is performed; development of local scours in proximity to the vertical circular pile is validated based on the results of large-scale experiments.

Keywords: local scours; GPU calculations; non-hydrostatic; openCL; sediment transport; three-dimensional multilayer model.

Classification: DDC Code: 621.51 LCC Code: TJ840'

Language: English

LJP Copyright ID: 392923
Print ISSN: 2631-8474
Online ISSN: 2631-8482

London Journal of Engineering Research

Volume 22 | Issue 8 | Compilation 1.0

GPU Accelerated Numerical Simulation of Local Scours Near Hydraulic Structures

Vladimir Prokofev

ABSTRACT

A module of sediments transport allowing to simulate the dynamics of local bed scours in proximity to hydraulic structures has been integrated into the three-dimensional non- hydrostatic multilayer open flow model. The sediment transport calculation is performed based on the formulas that apply the value of bed-shear stress. The slope slide in the scour hole and the alteration of the critical shear stress depending on the local bed inclination and flow speed direction are taken into account. This numerical model has been implemented completely by means of a GPU which allows to perform complicated 3D calculations within a reasonable time period. The results of testing performed based on the publicly available experimental data are given: comparison of the dynamics of bed transformation behind the apron as influenced by jet current is performed; development of local scours in proximity to the vertical circular pile is validated based on the results of large-scale experiments.

Keywords: local scours; GPU calculations; non-hydrostatic; openCL; sediment transport; three-dimensional multilayer model.

Author: Post-doctoral Researcher. *RusHYDRO, Hydraulic department of Vedeneev VNIIG, Russia.*

I. INTRODUCTION

Simulation of sediment transport and development of bed scours in proximity to hydraulic structures (HS) based on both physical and numerical models pertains to one of the most complicated and controversial fields of open flow hydraulics. Flow hydrodynamics – flow field, distribution of hydrodynamic pressure values and turbulence parameters in a flow – are simulated quite successfully by means of many modern numerical models including three-dimensional ones. The only difficulty that still remains is a significant time required to perform calculations for 3D tasks related to hydrodynamics which can equal a period of several days or even dozens of days. Using graphical processing units (GPU) allows to circumvent this restriction – Prokofyev (2017).

Numerical simulation of suspended and bedload sediments transport represents a more complicated task. There are dozens of formulas and models allowing to forecast bed deformations. However, calculations performed using such formulas and models are at the same time characterized by significant scatter of forecasting results, by one order or even more, especially in cases when not only the final depth of the scour holes or the height of the sediment deposits, but also simulation of their development in time are at issue. The criterion for estimation of the practical applicability of a particular model in HS engineering practice is validation of this model based on experimental data – field data or laboratory data.

There are cases when a numerical model is calibrated prior to its application for bed scour calculations with regard to a particular HS, which is quite logical. Still, in most cases initial data are not sufficient or reliable enough to perform such calibration. Moreover, even when the data set required for calibration is available, it is preferable that the model which has been tested based on experimental material be used as a baseline model for bed scours. It is also desirable that the set of free parameters of the model to be calibrated require no adjustment for each individual experiment *and be universal.* The present research is dedicated

to development of such baseline model and its testing based on experimental data obtained by third-party authors.

II. EDDY VISCOSITY SIMULATION

RANS numerical models for open flow hydrodynamics, both planimetric and three-dimensional, are well known. 2.5D description of a hydrodynamic model applying the so-called σ-coordinates for vertical discretization has been written by Audusse et al. (2011); the designation 2.5D corresponds to the use of a multilayer model in approximation of hydrostatic distribution of pressure over the flow depth. But in their turn, more complicated 3D multilayer open flow models consider the difference between the distribution of pressure over the flow depth and the hydrostatic one (Stelling & Zijlema, 2008; Ma et al., 2012; Prokofev, 2018), which requires that the Poisson equation be solved at each time step with the purpose of non-hydrostatic pressure correction. It was a full 3D model of open flow hydrodynamics that was taken as a basis for the sediments transport and bed scours model, and due to its stricter requirements to computational resources, it was fully implemented for the performance of calculations in a graphical processing unit – GPU (Prokofyev, 2017). We are not going to specify its description again here, f.e. by giving mass and momentum exchange equations in case of multilayer vertical discretization, but we are going to focus only on the modifications introduced to the model and its peculiarities that are important when bed scours simulation is performed. We shall specify that the algorithm is based on an explicit second order time accuracy prediction-correction scheme. During each time step, the simplest iteration method that is quickly convergent and efficiently implemented for GPU is used for solving the Poisson equation with the purpose of non-hydrostatic pressure correction (Prokofev, 2018). The model ensures conservation (exact fulfillment of the conservation laws for a discrete form) of exchange of mass, momentum and other substances.

First of all, the model shall be supplemented with the eddy viscosity calculation module based on the widely used *k*-ε turbulence model. Eddy viscosity is written as an (Belov & Kudriavtsev, 1987; Lin & Liu, 1998)

$$\nu_t = C_\mu \cdot k^2 \big/ \varepsilon \ ,$$

equation for exchange of turbulence kinetic energy k (TKE) and its dissipation rate ε :

$$\frac{\partial k}{\partial t} + \nabla \bullet \left(\boldsymbol{u} \cdot k \right) = \nabla \bullet \left[\left(\nu + \frac{\nu_t}{\sigma_k} \right) \nabla k \right] + Prod - \varepsilon \ , \tag{1}$$

$$\frac{\partial \varepsilon}{\partial t} + \nabla \bullet \left(\boldsymbol{u} \cdot \varepsilon \right) = \nabla \bullet \left[\left(\nu + \frac{\nu_t}{\sigma_\varepsilon} \right) \nabla \varepsilon \right] + C_{1\varepsilon} \frac{\varepsilon}{k} Prod - C_{2\varepsilon} \frac{\varepsilon^2}{k} \ . \tag{2}$$

In case of equations (1) and (2): t – time, ν – liquid kinematic viscosity, while the turbulent production rate $Prod$ for an incompressible liquid is defined using the magnitude of the strain-rate tensor S:

$$Prod = \nu_t S^2; \quad S^2 = \left(\frac{\partial u_i}{\partial x_j} + \frac{\partial u_j}{\partial x_i} \right) \frac{\partial u_i}{\partial x_j} \ , \tag{3}$$

where x_i – coordinate, u_i – current velocity vector components $\boldsymbol{u}$, summation is performed over the $i = 1,2,3$ repeated index. Standard set of constants for the *k*-ε turbulence model: $C_\mu = 0.09;\ \sigma_k = 1.0;\ \sigma_\varepsilon = 1.3;\ \ C_{1\varepsilon} = 1.44;\ C_{2\varepsilon} = 1.92$. Wu et al. (2004) compare other

London Journal of Engineering Research

types of the *k*-ε turbulence model, f.e. the Non-equilibrium *k*-ε model and RNG turbulence model which differ primarily from the standard one in the set of these 4 constants. In particular, the following values are assumed for the RNG model: $C_\mu = 0.085$; $\sigma_k = 0.7179$; $\sigma_\varepsilon = 0.7179$; $C_{2\varepsilon} = 1.68$, and the constant $C_{1\varepsilon}$ becomes the parameter depending from the value *S* in this particular point (Wu et al., 2004; WAQUA/TRIWAQ, n.d.):

$$C_{1\varepsilon} = 1.42 - \frac{\eta\left(1-\eta/4.38\right)}{1+0.015\cdot\eta^3}, \quad \eta = \frac{k\cdot S}{\varepsilon}.$$

The wall functions technique is widely used for setting boundary conditions for the turbulence parameters *k* and ε at the bed (Belov & Kudriavtsev, 1987; Wu et al., 2004; Kuzmin et al., 2007). In our research, we apply multilayer flow depth discretization (Audusse et al., 2011; Prokofev, 2018), so the use of the above-mentioned method comes down to special recording of the (1) and (2) discrete equation analogs in the lower (near-bottom) layer and TKE production rate (3). The TKE dissipation rate exchange equation ε (2) in the lower computation layer is not solved. Instead of this, ε in the middle of the layer is calculated directly using the value *k* in the middle of the relevant layer that has already been defined by applying the exchange equation (1) (Belov & Kudriavtsev, 1987; Wu et al., 2004):

$$\varepsilon = C_\mu^{3/4}\cdot k^{3/2} \Big/ \left(\mathrm{K}\cdot z^+\right), \tag{4}$$

where $\mathrm{K} = 0.41$ – Von Karman constant, z^+ – distance from the reference computation node to the bed. In case of near-bed computation layer, it is considered that the convective and diffusion exchange *k* through the lower surface of the layer is absent. The strain-rate tensor *S* components (3) defined trough derivatives of bed-wise tangent velocity components cannot be precisely calculated in case of the near-bed layer using the finite differences: the current velocity increases too rapidly as moving up from the bed in compliance with the logarithmic law. That is why the wall-functions technique (Belov & Kudriavtsev, 1987) is used here as well, so that the derivatives that are out of the viscous sublayer are calculated based on the logarithmic near-bed velocity profile (Kim et al., 2017; Török et al., 2017]:

$$z = z^+ : \quad \frac{\partial \boldsymbol{V}}{\partial N} = \frac{\boldsymbol{V}}{z^+\ln\left(z^+/z_0\right)}, \tag{5}$$

where $\boldsymbol{V}$ – current velocity vector in the mesh node that is the closest to the bed, situated at the distance of $z^+ > z_0$ from the bed, *N* – hereinafter represents the boundary normal, z_0 – bed roughness parameter. The last example is in some cases expressed as $k_s/30$, where k_s is the Nikuradse's roughness parameter (Kim et al., 2017). In case of condition (5) the velocity along the bed is taken as the rate $\boldsymbol{V}$, so the local slope angle is considered. The bed-shear stress required to solve the system of hydrodynamic equations may be expressed through the value of TKE or the flow speed in the near-bed computation node in case the *k*-ε model is applied (the one belonging to the previous time step is taken) (Wu et al., 2004; Belov & Kudriavtsev, 1987, p.133):

$$\boldsymbol{\tau} = \boldsymbol{V}\cdot\rho\cdot\mathrm{K}\cdot C_\mu^{1/4}\cdot\sqrt{k} \Big/ \ln\left(z^+/z_0\right), \tag{6}$$

where ρ – water density. Török et al. (2017) use $|\boldsymbol{\tau}| = \rho\cdot k\sqrt{C_\mu}$ instead of (6), but within the context of the present research such recording format is less convenient: it does not define the direction of $\boldsymbol{\tau}$ (Belov & Kudriavtsev, 1987).

London Journal of Engineering Research

In case of free surface, soft boundary conditions are commonly used for the turbulence parameters k and ε (Lin & Liu, 1998) – absence of their convective and diffusion exchange through the upper boundary of the surface computation layer:

$$\partial k / \partial N = \partial \varepsilon / \partial N = 0 \quad . \tag{7}$$

The specific distribution of k, ε, ν_t, V over the flow depth obtained through experiments under conditions of a uniform steady current in an open channel can be found in the research paper by Violeau & Issa (2007). These values show that the condition (7) which is widely used on the free surface referring to k is characterized by limited applicability; Török et al. (2017) set $k = 0$ on the surface. The turbulent production rate *Prod* (3) in the upper layer was calculated using the standard procedure: wall functions were not involved. Setting soft boundary condition (7) for ε on a free surface also represents a disputable issue: such a condition corresponds to the predominance of turbulence with the vertical axis of eddy currents. If the eddy exchange based on the flow depth is the main factor and this exchange is defined by eddy currents with the horizontal axis, it is more logical to set condition (4) for ε on a free surface and consider z^+ to be the distance from the computation node in the middle of the upper layer to the surface. The horizontal and vertical scales of turbulence can be significantly different (Voltsinger et al., 1989), in other words, eddy exchange is anisotropic and that is why in some cases 2 models are used to describe it: separately for horizontal and vertical directions (Rodriguez-Cuevas et al., 2014; WAQUA/TRIWAQ, n.d.).

In case of the impermeable boundaries of the computation domain (vertical walls), the boundary conditions set for the k и ε turbulence parameters were set to be same as those for the bed, however, additional TKE production rate was not calculated using the (5) formula: the walls were assumed to be smooth. In case of open vertical boundaries of the computation domain, the soft boundary conditions (7) were set in cases of outflow. In case of inflow through the boundary, a profile of k and ε that was close to the equilibrium one was set (Kuzmin et al., 2007):

$$k = \frac{U_*^2}{\sqrt{C_\mu}} \quad , \quad \varepsilon = \frac{C_\mu^{3/4} \cdot k^{3/2}}{\mathrm{K} \cdot h(1-\sigma)\sigma} \quad , \tag{8}$$

where h – depth in area of the boundary with inflow, $U_* = \sqrt{\tau / \rho}$ – bed-shear velocity, σ – dimensionless distance from the middle of the relevant computation layer to the bed (normalized for h: at the bed $\sigma = 0$, on free surface $\sigma = 1$). Based on test calculations, a soft boundary condition may also be set for k in case of sub-critical inflow: $\partial k / \partial N = 0$, and ε is to be determined based on (8) through k (TKE) in the near-boundary computation node, taking the relevant value from the previous time step.

The discrete form of the exchange equation for the k and ε turbulence parameters is written applying a conservative format, the same as in case of exchange equations for the momentum components or other substance in numerical multilayer open flow models (Audusse et al., 2011). In case of horizontal coordinates, the finite volume method (FV) is used while in case of vertical coordinates adaptive mesh is used (σ-coordinates), Prokofev (2018). In this case, the convective and diffusion exchange of the turbulence parameters between the computation layers is taken into account. In order to increase the scheme accuracy to the second order of magnitude when recording convective fluxes through the FV cell faces and between the layers, the TVD reconstruction is used (Kulikovskii et al., 2001).

In case of approximation of depth, bed levels and horizontal components of the current rate in the FV cell faces, the UNO scheme was used (Kulikovskii et al., 2001, p.115) as it ensures the highest accuracy of fluxes approximation and is better for description of the eddy

current structures which are formed for example when flowing around the circular cylinder. As opposed to less complicated reconstruction schemes (used for k, ε and convective exchange between the computation nodes), a 5 point skeleton instead of a 3 point one is generated; the points are located along the computation mesh line that passes through the FV cell face. We are going to express the values in the above-mentioned points that were already obtained during the previous time step using the following $Z_m;\ m=1,2,3,4,5$: in order to perform reconstruction, the derivative $\partial Z/\partial m$ in Z_3 point shall be determined. In case of standard 3 point schemes of TVD reconstruction, this derivative is determined by means of increment addition in order to ensure stability

$$dZ_3 = \text{Limiter}\left(Z_4 - Z_3,\ Z_3 - Z_2\right).$$

In this case, the function Limiter (A,B) that depends on the two parameters represents a limiter, f.e. the simplest MinMod. The above-mentioned limiter and other well-known limiters are specified in the book Kulikovskii et al. (2001). In case of the 5 point UNO scheme, the three additional parameters are determined first

$$D_m = \left(Z_{m-1} + Z_{m+1}\right)/2 - Z_m; \qquad m = 2,3,4 \quad ,$$

followed by the necessary increment value in the point Z_3

$$dZ_3 = \text{Limiter}\left[Z_3 - Z_2 + \text{Limiter}\left(D_2, D_3\right),\ Z_4 - Z_3 - \text{Limiter}\left(D_3, D_4\right)\right].$$

As the Limiter (A,B) for practical calculations, the Van Leer limiter can be taken, however, the same approximation accuracy with lower pulsations in the field of a moving bore (test task) is provided by the next limiter. In case of different values of the parameters A and B, it normally equals zero but in other cases the

$$\text{Limiter}\left(A,B\right) = 0.5 \times \begin{cases} \min\left(A, \alpha B\right) + \min\left(B, \alpha A\right)\ , & A > 0 \\ \max\left(A, \alpha B\right) + \max\left(B, \alpha A\right)\ , & A < 0 \end{cases}.$$

Parameter α may be represented by any value from the range [1..2]; we used the value $\alpha = \sqrt{2}$. This limiter shall not be confused with the well known SuperBee limiter: even with $\alpha = 2$ they are not congruent. In proximity to the boundaries of the computation domain, the 5 point reconstruction scheme has to be transformed into a 3 point one become a 5 point skeleton cannot be constructed.

The multilayer open flow model written using adaptive σ-coordinates allows for using the vertical mesh with condensation near the free surface (which may be useful when solving wave problems) and/or near the bed. The computation mesh condensation near the bed allows to save computational resources when solving tasks related to transport of sediments and bed scours. We applied mesh condensation near the bed based on hyperbolic functions:

$$\sigma\left(l\right) = \sinh\left(\beta l / L\right)/\sinh\left(\beta\right)\ , \qquad 0 \le l \le L\ , \tag{9}$$

$$\beta = \text{arccosh}\left(E\right), \qquad E = \Delta\sigma^{\max}/\Delta\sigma^{\min}\ .$$

Here: L – number of computation layers, the layers are given numbers from 0 (near the bed) to L-1; the parameter E sets the required mesh condensation, namely a relation between the thickness of the layer near the free surface versus the thickness of the near-bed layer. The dimensionless coordinate related, for example, to the medium level of the 3rd layer is located as per (9), the same as $\sigma\left(3.5\right)$, and the same coordinate of the lower boundary is $\sigma\left(3.0\right)$.

London Journal of Engineering Research

III. TRANSPORT OF SUSPENDED AND BEDLOAD SEDIMENTS

In addition to the *k*-ε module of the turbulence model, a computation module for sediment transport and bed scours has been added to the multilayer open flow model. Let's focus on some of its peculiarities that are important when simulating local bed scours in the context of the text tasks given below:

- procedure for re-calculation of the suspended load transport into erosion rate: volume of soil that is converted into a suspended state near the bed per unit time;
- consideration of the local bed slope during calculation of a critical shear stresses;
- simulation of slides of soil slopes formed in the context of re-formation of the bed in cases when their angle reaches the limit value.

The particle fall velocity is calculated using the Soulsby's formula (1997)

$$w = \frac{\nu}{d}\left(\sqrt{10.36^2 + 1.094 \cdot D_*^3} - 10.36\right), \tag{10}$$

where d – diameter of sediment particles, $D_* = d\left(\varphi_\rho \cdot g / \nu^2\right)^{1/3}$ – dimensionless diameter of particles, $\varphi_\rho = (\rho_s - \rho)/\rho$, ρ_s – sediment skeleton density, g – gravity acceleration, ν – kinematic water viscosity calculated using the Poiseuille's formula at the temperature T set in degrees C

$$\nu = 1.78 \times 10^{-6} \Big/ \left(1 + 0.0337 \cdot T + 0.000221\sqrt{T}\right), \ (\mathrm{m^2\,s^{-1}}). \tag{11}$$

In order to calculate the suspended load transport rate the Van Rijn's formula (2012), for example, can be used

$$q_s = 0.008 \cdot \overline{V} \cdot d \cdot M_e^{2.4} \cdot D_*^{-0.6}, \tag{12}$$

where the dimensionless mobility parameter of sediment particles with the depth-averaged flow speed is $\overline{V}$

$$M_e = \left(\overline{V} - V_{CR}\right) / \sqrt{\varphi_\rho \cdot g \cdot d}.$$

The dimensionless diameter D_* and the particle fall velocity w (10) are significantly dependent on the water kinematic viscosity (11) and consequently on its temperature. Depth averaged critical velocity corresponding to the initiation of the particles motion for Van Rijn's formula (12)

$$V_{CR} = 5.75 \cdot \mathrm{Lg}_{10}\left(2h/d\right)\sqrt{\theta_{CR} \cdot \varphi_\rho \cdot g \cdot d},$$

where the dimensionless critical Shields's parameter is

$$\theta_{CR} = 0.3/\left(1 + 1.2\,D_*\right) + 0.055\left[1 - \exp\left(-0.02 D_*\right)\right]. \tag{13}$$

Apart from Van Rijn's formula (12), there are at least several dozens of other formulas allowing to estimate the suspended load particles transport, generated based on both field data and laboratory measurements carried out in hydraulic flumes just like in (12). However, in case of such an averaged format the connection between the depth-averaged suspended sediment transport load q_s and the depth-average flow speed $\overline{V}$ (or even the bed-shear stress measured with regard to such a speed) cannot be used directly in a numerical 3D convective-diffusion model of suspended particles exchange. In case of such a model, it is necessary to connect, for example, the local value of bed-shear stress τ with the lifted particle's flux from the packed bed in the near-bed layer. For this purpose, it will be required to adapt formula (12) or any other similar one to re-calculate the suspended load transport of the flow into its *erosion rate.* Taking into account that Van Rijn's (2012) experiments were carried out under a

London Journal of Engineering Research

uniform and steady flow condition, we can take the profile of the eddy viscosity distribution over the flow depth using Montgomery's parabolic formula (Voltsinger et al., 1989):

$$\nu_t(\sigma) = \mathrm{K} \cdot h \cdot U_* (1-\sigma)\sigma \ . \tag{14}$$

The steady state distribution of volumetric concentrations of suspended particles $c(\sigma)$ over the depth in a uniform flow shall be compliant with the stationary one-dimensional convective and diffusion vertical exchange equation (Van Rijn, 2012):

$$\frac{\nu_t(\sigma)}{h}\frac{dc}{d\sigma} = -w \cdot c \ . \tag{15}$$

If we put the turbulence viscosity profile (14) into this equation, once the variables and integration values are substituted, we can find an analytical solution (15) – Rouse's *equilibrium* concentrations profile (Van Rijn, 2012; Delft3D-FLOW, 2005; Amoudry, 2008)

$$c(\sigma) = c_0 \left[\frac{\sigma_0(1-\sigma)}{\sigma(1-\sigma_0)}\right]^{\frac{w}{\mathrm{K}U_*}} , \tag{16}$$

where c_0 – concentration at a dimensionless distance from the bed σ_0, in our case this may be a medium level in the lower computation layer. A *non-equilibrium* profile is used in Delft3D-FLOW (2005) as well when the power indicator (16) is defined in the course of calculations related to the vertical concentrations gradient during the previous time step: we do not need it *now*. The concentration profile (16) is characterized by singularity at $\sigma \to 0$, that is why in order to evaluate the relation between the suspended load transport q_s and the near-bed concentration c_0, Rouse's profile, when the w and U_* values were known, was integrated within the range $[\sigma_{\min} \ldots 1]$:

$$q_s = c_0 \cdot h \int_{\sigma_{\min}}^{1} V(\sigma)\left[\frac{\sigma_0(1-\sigma)}{\sigma(1-\sigma_0)}\right]^{\frac{w}{\mathrm{K}U_*}} d\sigma \, . \tag{17}$$

Where $V(\sigma)$ – velocity profile. Logarithmic profile, for example. With the σ_0, $\sigma_{\min}$ parameters set and the bed-shear velocity U_* that also defines the $V(\sigma)$, numerical integration (17) can be carried out using the simplest quadrature formulas. It gives linear connection $c_0 = r \cdot q_s$. The $\sigma_{\min} \le \sigma_0$ parameter was set to be equal to 0.005, and in case of additional test calculations for suspended sediments (*test 2* below) it varied for evaluating the influence of $\sigma_{\min}$ on the results: it was not found. This is explained by the fact that in the area near the bed $V(\sigma) \to 0$, that is why singularity does not show itself in case of expression under integral sign (17); standard profiles $V(\sigma), c(\sigma)$ and their derivatives are specified in Van Rijn (2012).

A similar but not identical procedure for defining concentrations for near-bed computation layers with the use of Rouse profile (16) can be found in the description Delft3D-FLOW (2005), and in that case the concentration at the low level σ_0 is therein called a "reference" one (see also Van Rijn, 2012; Amoudry, 2008). Thus in case of an experiment with a *uniform current*, we can move from suspended load transport rate q_s calculated using (12) or any other empirical formula into the reference concentration c_0 near the bed, for example in the middle of the near-bed computation layer. When the empirical

London Journal of Engineering Research

formula for q_s is generated based on depth-averaged flow speeds, as in our case (12), but not based on bed-shear stresses τ, first of all re-calculation is to be performed $\overline{V} = f(\tau)$. It is clear that if during such a laboratory experiment the flow transports a quantity of suspended sediments complying with its transport rate, dynamic equilibrium of sediment particles elevation and sedimentation is observed in the near-bed layer, in other words the flow erosion rate that we require – rate of particles elevation from the bed $V_{lift} = w \cdot c_0$.

Basically, we just re-interpret the numerous laboratory data regarding *uniform* currents with a *steady state* concentration profile (16) obtained before: not only do we take the suspended transport rate q_s from such data but we re-calculate it into the erosion rate $V_{lift} = f(\tau)$. And then we use the erosion rate during 3D simulation of suspended sediments transfer for more complicated currents different from uniform ones. Amoudry (2008) and Wei et al. (2014) use other formulas for calculation V_{lift} directly through the bed-shear stress τ. But in case of a test example with a uniform steady current, inside a hydraulic flume, these do not provide the same suspended load transport values q_s as in case of 'classic' formulas like (12) or similar. Moreover, formulas for direct calculation V_{lift} involve a number of empirical parameters that are hard to define.

The equation for convective-diffusion exchange of suspended sediments is recorded using the same form as in case of (1), (2):

$$\frac{\partial c}{\partial t} + \nabla \bullet \left[\left(\boldsymbol{u} - w \cdot \boldsymbol{I_Z} \right) c \right] = \nabla \bullet \left[\left(\nu + \nu_t \right) \nabla c \right] \quad , \tag{18}$$

where c – dimensionless volumetric concentration of suspended particles, $\boldsymbol{I_Z}$ – singular vector directed upwards. A format of recording this equation in a conservative form with regard to vertical multilayer flow discretization is specified by Audusse et al., 2011 and Prokofev (2018): the format is standard just like in case of (1), (2). The source term for suspended sediments elevated from the bed by the flow, is not included into the right part (18): it is described using the lower boundary condition. That is why the discrete form of (18) recorded for the lower (near-bed) computation layer includes the supplement V_{lift} instead of convective exchange through the lower surface of this computation layer congruent with the bed.

There are also dozens of empirical formulas for evaluation of bedload sediment transport. For example, the famous software *Flow-3D*® (Wei et al., 2014) uses the formula by Meyer-Peter & Müller (1948), and based on this formula the specific sediments transport ($m^2 s^{-1}$) is calculated based on the established bed-shear stress:

$$q_b = \beta_n \left(\theta - \theta_{CR} \right)^{1.5} \sqrt{\varphi_\rho \cdot g \cdot d^3} \ , \ \text{where} \ \ \theta = \tau / \left(\rho \cdot \varphi_\rho \cdot g \cdot d \right) \quad . \tag{19}$$

Where β_n – dimensionless empirical order 8 coefficient, and the Shields's critical parameter θ_{CR} is proposed to be taken being equal to 0.047 as per the original research by Meyer-Peter & Müller, however, in the later research, for example Wei et al. (2014) it is calculated using the formula by (13) Soulsby (13) (1987), like in case of suspended sediments. For comparison, let's also mention Van Rijn's formula (1984) for bedload sediment transport used by Ahmad et al. (2014) and in the model COHERENS (n.d., Chapter 7):

$$q_b = \frac{0.053}{D_*^{0.3}} \left(\frac{\theta - \theta_{CR}}{\theta_{CR}} \right)^{2.1} \sqrt{\varphi_\rho \cdot g \cdot d^3} \quad . \tag{20}$$

As compared to formula (19), it is significantly different both in its dependence on the particles diameter and indicator of the power to which bed-shear stresses are raised: 2.1 vs 1.5.

In the works by Wei et al. (2014), Ahmad et al. (2014), Zhou (2017), dedicated to studying of 3D numerical simulation of local bed scours due to sediments transport, the critical bed-shear stress or the Shields's critical parameter (13) are normally adjusted with regard to local bed slopes. In case when the angle of an underwater slope is close to the limit one (steepest slope angle) and the current velocity is directed 'down grade', θ_{CR} shall be reduced down to 0. In case when the flow direction is reverse, it is vice versa: θ_{CR} shall increased by two times at the limit. Zhou (2017) specifies that such adjustment is highly important for correct simulation of local scours. Figure 1a shows a diagram for angle designations related to inclined slopes and the flow speed vector. Shields's critical parameter is adjusted based on Soulsby's formula (1997) which is also applied by Wei et al. (2014) и Ahmad et al. (2014)

$$\theta'_{CR} = \frac{\theta_{CR}}{T_m}\left(\cos(\psi)\,\sin(\chi) + \sqrt{\cos^2(\chi)T_m^2 - \sin^2(\psi)\,\sin^2(\chi)}\right) . \qquad (21)$$

Where $T_m = \mathrm{tg}(\chi_{\max})$ – steepest slope angle tangent for packed bed sediments under water (steepest slope angle before grains slide by themselves); is normally $\chi_{\max}$ is set within the range of [28º…32º], $0 \le \chi \le \chi_{\max}$. The adjustment multiplier for θ_{CR} in formula (21) never falls outside the range of [0…2]. In case of sediments (bedload and suspended) transport formulas of type (19), this multiplier is directly used for θ_{CR} as per (21). In case of formulas of type (20) containing θ_{CR} in the denominator, it may only be applied to θ_{CR} contained in the numerator. It is convenient to determine the trigonometric functions included into (21) in the course of practical calculations using scalar products:

$$\cos(\psi) = \frac{\langle \boldsymbol{V}, \boldsymbol{G} \rangle}{|\boldsymbol{V}| \cdot |\boldsymbol{G}|}, \quad \sin^2(\psi) = 1 - \cos^2(\psi),$$

$$\cos^2(\chi) = \left(|\boldsymbol{G}|^2 + 1\right)^{-1}, \quad \sin(\chi) = \sqrt{1 - \cos^2(\chi)},$$

where $\boldsymbol{G} = \nabla Z^b$ – gradient vector for bed surface.

As per Zhou (2017), consideration of steep slope slides formed during bed scour in the numerical model is as important as adjustment of θ_{CR} with regard to local bed slopes as per (21). A diagram of the above mentioned process is given in Fig. 1b: for purposes of simplicity the representation is one-dimensional. The digits given in circles 1 and 2 are used to mark a pair of neighboring nodes of the computation mesh – FV centers. The tangent of the bed inclination angle between the two points is determined based on the bed levels Z_1^b and Z_2^b in these points: $T_{12} = \left(Z_2^b - Z_1^b\right)/\Delta x$. In case $|T_{12}| > T_m$, the slope slide process is included which means that bed levels adjustment is performed, considering T_{12}, for the value of

$$\Delta Z_1^b = \begin{bmatrix} (T_{12} - T_m)/2, & T_{12} > 0 \\ (T_{12} + T_m)/2, & T_{12} < 0 \end{bmatrix}, \qquad \Delta Z_2^b = -\Delta Z_1^b .$$

In the software code that implements such a method, these adjustment levels inside each time step are first recorded in *slide*-array in the form of a bed map and then, once the time step is completed (when all computation nodes are processed), *slide* adjustment is added to current

bed levels. In reality, in case of slope slide, sediments from point 3 not shown on Fig. 1b may be transferred to point 2. This may again lead to violation of the condition $|T_{12}| \le T_m$, but in a specific number of time steps its implementation can be ensured anyway. In case the task is not one-dimensional, slopes starting in this point directed to neighboring nodes are compared to the limit ones, including diagonal directions: in case of the FV regular mesh there are 8 such directions. In case of a curvilinear mesh, *slide* adjustment Z_1^b and Z_2^b is a little more complicated: it is required to take into account the ratio between the areas of the neighboring FV (1 and 2) in order to ensure the sediments mass conservation (scheme conservation) in case of slope slide.

After the dimensionless concentration of suspended sediments during another time step is calculated using the exchange equation (18) and the bedload sediment transport is determined, for example, based on (19), changes of bed levels Z^b are calculated using Exner's equation (Ahmad et al., 2014; Zhou, 2017)

$$\frac{\partial Z^b}{\partial t} = \frac{F}{1-p}\left[-\nabla \bullet \left(q_b \frac{\boldsymbol{\tau}}{|\boldsymbol{\tau}|}\right) - V_{lift}^0 + c_0 \cdot w\right], \qquad (22)$$

where p – soil porosity of 0.4 order of magnitude, $F \ge 1$ – boost factor for bed scours, V_{lift}^0 and c_0 – erosion rate for suspended sediments and their dimensionless concentration at the reference level σ_0. The approach that uses reference levels is specified in the description Delft3D-FLOW (2005). What is important is that this reference level has to be the same when defining the rate of elevation of suspended particles from the bed V_{lift} and their sedimentation – the last term (22). For example, in case of a multilayer model this may be an average level for the lower computation layer: earlier we used it to define V_{lift}. In case of single-layer (planimetric, 2D) models we deal with depth averaged concentrations of suspended sediments $c_m = q_s / q$ where $q = h \cdot \overline{V}$ – specific water discharge (Van Rijn, 2012). We can set, for example, $\sigma_0 = 0.05$. In this case V_{lift}^0 is brought to the erosion level, as it was described earlier, by integration (17) of the Rouse's profile (16) and, in the same manner, in case of the profile (16) transfer from c_m to near-bed concentrations of suspended sediments c_0 at the same level is performed $\sigma_0 = 0.05$: $c_0 = r \cdot c_m$, $r > 1$.

It is important to clarify that we only use Rouse's equilibrium concentrations profile (16) in two cases:

- in case of *interpretation* of data obtained during laboratory experiments involving suspended sediments which is allowable as the current is uniform under such conditions and the concentration profile is steady state;
- in case of a single-layer (planimetric, 2D) task when there is no other way to consider the non-uniformity of distribution of suspended sediments over the depth.

In a 3D case (multilayer model) it is clear that the distribution of concentrations of suspended sediments over the flow depth is more complicated: we take this into account when solving the 3D equation (18), and we only use the equilibrium profile (16) for re-calculation q_s into the erosion rate of the flow $V_{lift}^0(\tau)$.

The first term in the right part (22) reflects the contribution into the bed scours of bedload sediment transport directed along the bed-shear stress vector $\boldsymbol{\tau}$. The boost factor F can be used for demanding computation tasks to reduce the time needed for calculation of bed

scours related to sediments transport (Zhou, 2017, p.64). Such scours take place slowly as compared to the time necessary for the hydrodynamic part of the task to adapt to bed transformations. So in case of some tasks, once check calculations are performed one can take, for example, *F=10* and consider this time boost factor when interpreting the obtained results related to bed scours. The excessive value *F* may lead to calculations instability.

The divergence discrete form in the right part (22) is recorded using the central difference scheme. There was no need to use Zhou's (2017) filter for smoothing the oscillations of increments of the bed levels when solving Exner's equation (22). Once bed scours are calculated using the equation (22), the above described *slide* adjustment of the bed levels is performed additionally: consideration of the bed slides that had a slope angle higher than the limit one during the previous time step.

IV. VALIDATION OF A 3D NUMERICAL MODEL

The multilayer open flow model that was taken as a basis had already been tested earlier by comparing the calculation results with analytic solutions and experimental data. In particular, Prokofev (2017, 2018) validated the hydrodynamic pressure calculation module using wave problems where the difference of the pressure distribution over the flow depth from the hydrostatic one plays a key role. Let's focus only on additional validation of the new software modules described herein: calculation of turbulence parameters and sediments transport simulation.

4.1 Case 1. Turbulence model validation

A standard test to check the applicability of the turbulence model (1)-(5) is a task involving flowing around the spur-dyke by the open flow (Wu et al., 2004) or a task involving the formation of a recirculation zone under a flow in a sudden-expanded flume (Fe et al., 2000; Wu et al., 2004). Calculations were performed for both scenarios. For example, we compared the results of the numerical experiment involving flowing around spur-dyke, as in the research conducted by Wu et al. (2004) with the results of the laboratory experiment A1 by Rajaratnam & Nwachukwu (1983). A hydraulic flume with the width of 0.92 m and length of 37 m; a spur-dyke represented by an aluminum plate with the width of 3 mm and length of 0.152 m is installed in the middle of the flume orthogonally in relation to one of the walls. Flow depth – 0.189 m, discharge rate in the flume – 0.0453 m^3 s^{-1}. During the numerical experiment, a specific discharge level for the inflow (left) boundary was set, and the logarithmic depth profile of the normal velocity component $V_x(\sigma)$ was set, the shear components related to this boundary are $V_y = V_z = 0$. In case of the outflow (right) boundary, only the depth of the flow was registered. The bed roughness coefficient in the Manning formula is $n = 0.012$ $m^{-1/3}s$. In order to find the relevant roughness parameter z_0 in (5), (6) for this *n*, we are going to integrate the logarithmic velocity profile as per *z* within the range $[z_0 \ldots h]$ (Ahmad et al., 2014; Zhou, 2017); this profile provides a good description of the current not only in proximity to the bed but also over the whole depth:

$$U(z) = \frac{U_*}{\mathrm{K}} \ln\left(\frac{z}{z_0}\right).$$

If we compare the linear connection $\overline{U(z)} = a \cdot U_*$ that we obtained with Manning's formula for bed roughness, we find an exponential dependency of re-calculation $n \to z_0$:

$$z_0 = h / \exp\left(\frac{h^{1/6} \cdot \mathrm{K}}{n\sqrt{g}} + 1 \right) \quad . \tag{23}$$

In case of the specified depth parameter h, the formula (23) provides: $z_0 \approx 0.018$ mm.

The length of the calculation domain is 12 m, out of which 4 m are located to the left of the spur-dyke. In case of discretization based on planimetric coordinates a regular orthogonal mesh with 250×60 nodes was used that has a condensation similar to (9) in the spur-dyke area: along the flow axis, the ratio among the computational mesh steps is $\Delta x_{\max} / \Delta x_{\min} = 5.39$, in case of the flume cross section it is $\Delta y_{\max} / \Delta y_{\min} = 2.28$. In vertical direction, a uniform (without condensation) division into 10 layers was used. Similar tasks can be solved in a single-layer (planimetric) configuration and the 10 layers in our case were taken only for validation of the 3D turbulence model. The length of the recirculation zone that forms behind the spur-dyke depends significantly on the choice of the turbulence model and the boundary conditions related to this model; the boundary conditions (7) were set for the free surface. Based on the experimental results obtained by A1 Rajaratnam & Nwachukwu (1983), the length of the recirculation zone is about 2 m: from the spur-dyke downstream. Based on our calculations, its length was 1.85 m in case of using the standard k-ε turbulence model and 2.30 m when using its RNG-type or the non-equilibrium k-ε model. It is impossible to obtain a stable recirculation zone in calculations without taking the viscosity into account and the simplest single-parameter eddy viscosity models reduce its length significantly. Based on our calculations, the maximum value of eddy viscosity in the flow core after the spur-dyke reaches 0.0018 m^2s^{-1} (standard k-ε model), which is a little lower than the value obtained in the calculations by Wu et al. (2004) by means of the same model in a planimetric task: 0.0022 m^2s^{-1}, but close to the calculations by Wu et al. (2004) for the k-ε-RNG model (0.0017 m^2s^{-1}). The time spent by Nvidia GeForce GTX-1080ti GPU to solve this task with the 2.5D configuration does not exceed 5 minutes.

4.2 Case 2. Suspended transport model validation

It is difficult to find any published experimental data where the leading role would be played by suspended sediment transport: normally experiments involve large grain sand when scour deformations are defined primarily by the bedload sediments moving. Nevertheless it is desirable that the method for calculation of suspended sediment concentrations provided herein be also tested at least based on a virtual task. We can at the same time make sure that the software implementation of the k-ε turbulence model described ensures correct vertical distribution of eddy viscosity $\nu_t(\sigma)$: the previous *test 1* could be considered with a planimetric 2D configuration as well, so it only confirms the correctness of distribution simulation $\nu_t(x, y)$. Let's consider uniform steady current in a provisional hydraulic flume with the length of 150 m, flow depth of 3 m and depth-averaged current velocity of 1.5 m s^{-1}. If the bed roughness coefficient based on Manning's formula is $n = 0.016$ $m^{-1/3}s$, the roughness parameter as per (23) is $z_0 \approx 0.06$ mm. The bed-shear velocity at the specified parameters is $U_* \approx 0.062$ m s^{-1}. Let's assume that the flume smooth bottom is covered with even-grained sand $d = 0.1$ mm, $\rho_s = 2650$ kg m^{-3}. At the water temperature of T = 12ºC as

per (11) – $\nu = 1.2 \times 10^{-6}\,\mathrm{m^2 s^{-1}}$, while the grain fall velocity (10) of such sand is $w = 6.65 \times 10^{-3}\,\mathrm{m\ s^{-1}}$. The Rouse's parameter is $w/(U_* \mathrm{K}) \approx 0.27 < 1$, so one can expect that bed particles will transfer into a suspended state. Let's assume that a steady profile over the depth (16) of the sediment particles volumetric concentrations was set for the inlet flume cross section.

We are going to use the numerical scheme provided above involving the *k*-ε turbulence model and the empirical formula (12) to calculate the concentration profile in the outlet section: as the current is uniform, it is expected to represent the same Rouse's equilibrium profile as in case of the inlet to the hydraulic flume. During this test, calculations were performed with regard to the vertical longitudinal cross section of the flume only and the flume was uniformly divided into 15 layers depthwise: in fact, this is a 2D task. Calculation results are summarized in Fig. 2. Rouse's reference profile (16) is shown for which the constant c_0 corresponds to the suspended load transport q_s calculated using Van Rijn's empirical formula. Moreover, Fig. 2 shows the concentration profiles at the outlet of a virtual hydraulic flume obtained using a 15 layer numerical model. The first one was obtained based on soft boundary conditions (7) on the free surface which provides the distribution $\nu_t(\sigma)$ in proximity to it that is different from (14). As is shown in Fig. 2, this leads to deviations of the calculated concentration profile from Rouse's profile based on (14) and this only refers to the area near the free surface: $\sigma > 0.8$. The second concentration profile was obtained with the conditions (7) for *k* and (4) for ε on the free surface – such a possibility was discussed above, which provided vertical distribution of eddy viscosity (14). The second profile is almost identical to the Rouse's reference profile: the insignificant difference that is present is related to the choice of quite a rough (uniform) mesh in the vertical direction. All nodes of this mesh are marked with squares in Fig. 2. Moreover, the *k*-ε turbulence model is not even supposed to provide any perfect match of $\nu_t(\sigma)$ with the single-parameter Montgomery's formula (14) which also leads to insignificant differences among particle concentration profiles in Fig. 2. If we refuse to use the *k*-ε turbulence model and only use the equilibrium profile $\nu_t(\sigma)$ (14), the sediment concentration profile at the outlet boundary will be equal to the Rouse's reference profile (16). This proves that the diffusion components of the exchange equation (18) are approximated with a relatively high level of precision.

In addition to the above, during *test 2* depth-averaged concentrations of suspended particles c_m were compared: the concentration found using the (12) empirical formula and the one found through numerical integration (17) of the calculated concentration profile at the outlet of a provisional hydraulic flume. Their values are: 5.3×10^{-4} and 5.2×10^{-4}, respectively. This good coincidence is not that evident. First of all, each time prior to solving the exchange equation (18), re-calculation of the flow suspended load transport q_s was performed at every next time step with the concentration at the reference level of σ_0, and integration (17) was only performed up to the level $\sigma_{\min}$ – see the description above. Second, the profile $\nu_t(\sigma)$ in proximity to the outlet boundary calculated using the *k*-ε model could be significantly different from the profile (14) at the inlet, in case of mistakes in the algorithm, which would inevitably lead to differences among depth-averaged concentrations.

4.3 Case 3. Scour in a flume: GPU utilized 2D calculations

Test 3 gives a schematic description of formation dynamics of a scour hole and the dune behind it located after the rigid bed area (apron) in the tail race of the hydrosystem with bottom spillway. Vertical section of the laboratory bench of Chatterjee et al. (1994) is given in Fig. 3. The results of the experiment #2 pertaining to this research will be used for validation of numerical models of Abdelaziz et al. (2010), Wei et al. (2014), Zhou (2017). During the experiment, the flow depth h = 0.291 m is recorded at the right outlet boundary. The submerged water jet comes out through the narrow slit near the bed with the height of 2 cm and rate of 1.56 m s^{-1}; the area above the inlet gate is represented by a smooth wall. At a distance of 0.66 m from this wall, the bed is rigid and smooth, then it is made of sand with a median grain diameter of $d_{50} = 0.76$ mm, $\rho_s = 2650$ kg m^{-3}. In accordance with Zhou's (2017) numerical experiment, the sand porosity is $p = 0.43$ and the steepest slope angle is $\chi_{\max} = 29^{o}$.

The sand grain fall velocity found as per (10) with $\nu = 1.2 \times 10^{-6}$ $m^2 s^{-1}$ is w=0.098 m s^{-1}, which corresponds to the data given in the table but is slightly lower than the value used by Zhou (2017) and specified by Chatterjee et al. (1994) that is w=0.122 m s^{-1}. This is not crucial for numerical experiments as during such an experiment the movement of sediments is mostly forced and the calculation formulas for their transport (19) or (20) do not contain the particle fall velocity. Just like in previous *test 2*, here we can use a 2D numerical model for the longitudinal vertical cross section. On the left, the computation domain is limited by the coordinate $x = -0.66$ m that corresponds to the narrow slit with jet outlet. The distribution $V_x(\sigma)$ is set at this boundary and it is uniform within the gate. The right outlet boundary was selected at the point $x = +1.34$ m where the flow comes out freely, and only the water surface level is registered in the numerical model. The end of the rigid bed area is shown by $x = 0$ – Fig. 3. The mesh pitch along the longitudinal coordinate is $\Delta x = 4$ mm, so in total there are 500 finite volumes (FV) with regard to x. 40 computation layers with condensation near the bed were used for the vertical coordinate: when the parameter E=6 is set in (9), the mesh node that is the closest to the bed is located at about 1.5 mm from the bed and the thickness of the near-bed computation layer is about 3 mm (these values may change during transformation of the movable bed). For comparison: Zhou (2017) managed to achieve a remarkable consistency between the numerical simulation results and the experimental data using a more detailed computational mesh with the pitch of $\Delta x = 3$ mm across the longitudinal coordinate and $\Delta z = 2$ mm in vertical direction using a uniform division into 145 layers. Regarding bed transformation equation (22), we set F = 1, so boost was not used in *test 3*. In order to describe the bedload transport in *test 3* and the next *test 4*, empirical formula (19) with the parameter $\beta_n = 4.5$ was used. This value is lower than the value recommended by Wei et al. (2014) and Meyer-Peter & Müller (1948), which is equal to $\beta_n = 8$, but ensures better correspondence to the experiment. The roughness parameter for a rigid smooth bed area is $z_0 = 0.003$ mm, while in case of a sand bed based on the recommendations given by Wei et al. (2014) and Zhou (2017) the value $k_s = 2.5 \cdot d_{50}$, $z_0 = k_s / 30 = 0.063$ mm was used. This is important as z_0 is directly used when calculating bed-shear stresses (6) and these stresses are included into the bedload transport formula raised to the power of 1.5 (19) or even 2.1 (20). When working with formulas of types (19) or (20) that are based on the local value of bed-shear stress one cannot choose the

bed friction parameter z_0 separately from the sand grain median diameter (Zhou, 2017, p.55) for example by means of connecting it with a randomly chosen friction coefficient *n* using formula (23). In more complicated cases when the bed contains large uneven areas (riffles, ridges) friction parameters are set separately (COHERENS, n.d., p.312): 'global' k_b – for the hydrodynamic part of the task and k_s – for sediment transport calculation; k_s is lower; in publications by Van Rijn (2012), Zhou (2017) and the description of COHERENS it is designated using the term '*skin friction*'.

In calculations for *test 3*, the *k*-ε-RNG turbulence model (1)-(3) was used with the soft boundary conditions (7) on the free surface. The longitudinal profiles of the movable areas of the bed for 1, 3, 5, 8, 12, 20 and 30 minute time points obtained based on the calculation results are given in Fig. 4. The agreement with the bed levels recorded during the experiment that are marked with squares on the same figure is quite satisfactory. The dune slope located downstream has an angle that is close to the limit one equal to 29º. Using the *k*-ε turbulence model validated in *tests 1 and 2* during numerical simulation within the context of this experiment plays a key role: simulation of jet current without it, based on single-parameter models used for eddy viscosity ν_t calculation, *failed*. In case of *test 3*, taking into account the non-hydrostatic amendments to the pressure value (Prokofev, 2018) is also mandatory. The adjustment (21) approximates the computation data to the experimental ones significantly: if it is not used, their agreement is much worse that in Fig. 4. The influence of suspended sediments on the calculation results in *test 3* is extremely low.

The full computation time within *test 3* for the above mentioned GPU Nvidia does not exceed 3.5 hours[1] or 10 hours when using a *laptop* with the AMD[2] Radeon R9 M275x graphics processing unit. Analogous calculations performed by Zhou (2017, p.83) using the *OpenFOAM*® open code took 160 hours when using an 8-core CPU even with the algorithm multisequencing and boost activation $F = 5$ in (22). Prokofev (2017, 2018) already specified high efficiency of GPU utilization in algorithms based on an explicit scheme with a random order of computation node processing at each time step.

Let's analyze the numerical simulation results provided by other authors for *test 3*. Zhou (2017, p. 90) provides diagrams similar to Fig. 4 and they demonstrate almost full agreement with the experimental data obtained by Chatterjee et al. (1994). However, it remains unclear why in case of 1 minute time step the lower dune slope has an angle that is larger than the limit one equal to 29º. In case of a physical experiment, this may be explained by both a measurement error and incompleteness of the slope slide process. But how could such an 'extreme' slope be obtained using a numerical model where the slope slide is considered instantaneous (Zhou, 2017, p.60 & Appendix B)?

Abdelaziz et al. (2010) and Wei et al. (2014) when simulating *test 3* used adaptation of the well-known commercial software *Flow-3D*® designed by *Flow Science*: a sediment transport module is integrated into it. Abdelaziz et al. (2010) only managed to obtain agreement between the scour depth and the dune's crest with the experiment values related to initial time steps of 1…8 minutes (full experiment time is 60 minutes). The calculated bed transformation profile itself is far from the value obtained in the experiment, which is directly specified by Abdelaziz et al. (2010) in the conclusions.

Finally, Wei et al. (2014) also specify their results for numerical simulation for *test 3*. Unfortunately, the figures containing consecutive changes of the bed profile obtained from

[1] The time is specified for calculations involving not 1 but 3 vertical cross sections: the minimum quantity allowed by our software.

[2] OpenCL language is used which works over Nvidia, AMD, INTEL processing units.

Flow-3D® are nor superimposed over the experimental curves contained therein. There is visual similarity and the steepest slope angle is well observed. At the same time, analysis of the figures provided by Wei et al. (2014, Fig.8) shows that during the first minute the simulated dune's crest shifts from the rigid bed area by $x_c = 39$ cm (see scheme in Fig. 3) instead of 24 cm as in the physical experiment, and within 3 minutes the dune's crest shifts from the apron by $x_c = 42$ cm instead of the 30 cm calculated during the same experiment.

Then the dune movement in the numerical simulation by Wei et al. (2014) gets slower and after 30 minutes it almost stops: 2-cm displacement during the next 30 minutes instead of 8 cm as shown in the measurements. In other words, no reliable consistency between the results obtained by Wei et al. (2014) and the experimental data related to the dune movement *dynamics* is observed, though, just like in our research, the same bedload transport formula (19)[3] and the same adjustment θ_{CR} (21) were used and the slide of steep slopes was taken into account; it was not considered by Abdelaziz et al. (2010).

The analysis that was performed shows that *test 3* is quite complicated for validation of computation algorithms and the software packages.

4.4 Case 4. Scour around big vertical cylinders: GPU based 3D simulation

With the purpose of approbation of sediment transport numerical models and movable bed transformations, simulation of bed scours in a hydraulic flume in proximity to the circular cylinder (pile) is widely used. In most cases, the data obtained in small-scale physical experiments are used for comparison when the cylinder diameter does not exceed 0.2 m (Ahmad et al., 2014; Kim et al., 2017; Zhou, 2017). In proximity to the pile, a complex condition of eddy currents is observed: downstream currents and whirlwinds with a horizontal axis predominate near its front, while behind the pile, there are unstable eddy currents with a vertical axis (Zhou, 2017). In case of such a task, numerical simulation can be performed only with a 3D configuration, it is mandatory to take into account the difference between the vertical distribution of hydrodynamic pressure and the hydrostatic pressure and use the turbulence model for the hydrodynamic model closure. These calculations require significant computation efforts, f.e. Zhou (2017, p.142) spent 1,160 hours (1.5 months) to perform erosion simulation in proximity to the cylinder with the diameter of 0.1 m using the *OpenFOAM*® open code and an 8-core CPU. This simulation covered only the first 30 minutes of the 3 hours of the whole physical experiment duration.

The most interesting experimental data related to transformation of sand bed in proximity to circular cylinders with various diameters as influenced by stationary currents in a hydraulic fume are given in the report by Sheppard (2003). The research was performed at the University of Florida (USA) and completed in 2003. The experiments were performed in a hydraulic flume with the width of 6.1 m, depth of 6.4 m and length of 38.4 m, with 9.8 m occupied by the movable area. Sand bed erosion with a median grain diameter of d_{50}= 0.22 mm, 0.8 mm and 2.9 mm was studied in proximity to circular cylinders with the diameter of 0.114 m, 0.305 m and 0.915 m, and various combinations were analyzed. Flow depth and speed varied: in total, 14 tests were performed and the duration of some of these tests amounted to 579 hours (experiment #14). All the necessary flow physical parameters, including the water temperature, were registered – ref. to (11); by means of an acoustic transponder and two miniature video cameras, the development of scour deformations in time was observed. The flow speed was defined based on two electromagnetic flow meters:

[3] Wei et al. (2014) applied formula (19) with $\beta_n = 8.0$ (default value).

western/eastern, and the discharge was measured based on the measurement weir. The time dependences of the maximum scour depth value are given in the report by Sheppard (2003) in the form of tables and graphics.

In order perform validation of the numerical model, we chose four tests from the report by Sheppard (2003), involving circular cylinders with the biggest diameter of 0.915 m: these are experiments #3, #4, #7 and #14. For all the relevant numerical tests, the following was used:

- The *k*-ε-RNG turbulence model with the boundary conditions (7) on the free surface;
- in case of the inlet boundary – logarithmic distribution of longitudinal velocities $V_x(\sigma)$, tangential velocity components $V_y = V_z = 0$;
- in case of the outlet boundary, only the water surface level was fixed;
- the lateral walls of the hydraulic flume and cylinder surface are smooth (which means that additional TKE production rate is absent) and impermeable;
- Van Rijn's formula (12) for description of the movement of suspended sediments[4];
- Meyer-Peter & Müller formula (18) for bedload sediment transport with the parameter $\beta_n = 4.5$ – like in previous *test 3*: as it was already specified in the introduction, we are not trying to adjust the numerical model to each particular experiment but carry out its *calibration only once;*
- sand bed roughness parameter $z_0 = k_s / 30$, where $k_s = 2.5 \cdot d_{50}$: the same as in *test 3*;
- porosity for quartz sand $p = 0.4$, steepest slope angle $\chi_{\max} = 30^{\circ}$;
- boost factor *F* in (22): during the first 2.5 minutes, the current stabilizes and the bed erosion is not active, *F*=0; during the next 2.5 minutes, bed scours boost is activated with *F*=10; then, during 25 hours *F*=60 is applied (1 minute of hydrodynamic computation corresponds to 1 hour of morphometrical computation), and then – *F*=180; during the final bed scour stage even *F*=360 may be set which does not cause algorithm instability or affect the results;
- uniform orthogonal mesh along the planimetric coordinates 541×254 of nodes for the computational domain $x \in [-6, +7]\,\text{m}$, $y \in [-3.05, +3.05]\,\text{m}$; condensation of the horizontal mesh in proximity to the cylinder that has its center in *x=y=0* was not applied: the UNO flux reconstruction scheme described above ensures sufficient accuracy of approximations; computational mesh pitch $\Delta x = \Delta y = 0.024$ m;
- condensation parameter near the bed of the vertical computational mesh in (9) *E* = 6.

Now let us list the parameters that differ in experiments #3, #4, #7 and #14.

Experiment #3: median grain diameter of the bed material $d_{50} = 0.8$ mm, average flow depth $h = 1.27$ m, water temperature[5] $T = 8.5\,^{\circ}\text{C}$, depth averaged flow speed $\overline{V} = 0.4\ \text{m s}^{-1}$ – was taken as an average value between the western and the eastern velocity sensor); experiment duration $t_{\max} = 362$ hours; in vertical direction we used $L = 36$ computation layers.

[4] In case of the experiments selected, suspended sediments do not play any significant role.

[5] The experiments themselves were performed at the USGS Laboratory, Massachusetts, not in Florida.

London Journal of Engineering Research

Experiment #4: $d_{50} = 0.8$ mm, $h = 0.87$ m, $T = 0.5$ °C, $\overline{V} = 0.365$ m s^{-1}, $t_{\max} = 164$ hours: the report by Sheppard (2003) specifies the time equal to $t_{\max} = 143$ hours, but data for 21 more hours are also given; L=25.

Experiment #7: $d_{50} = 2.9$ mm, $h = 1.22$ m, $T = 0.7$ °C, $\overline{V} = 0.755$ m s^{-1}, $t_{\max} = 188$ hours; $L = 36$.

Experiment #14: $d_{50} = 0.22$ mm, $h = 1.81$ m, $T = 23$ °C, $\overline{V} = 0.3$ m s^{-1}, $t_{\max} = 579$ hours; $L = 45$.

The computation time when using the Nvidia GeForce GTX-1080ti game graphics processor unit in case of #3, #4 and #7 experiments amounted to 82, 23.5 and 53 hours respectively. This is a relatively short time period for such large scale 3D tasks, and the major part of this time period is spent on solving the Poisson's equation for non-hydrostatic pressure correction by using the simplest iteration method (Prokofev, 2018). As even when the boost factor F in (22) is considered, the bed transformation rate is extremely slow, the task is close to a stationary one and the iterations converge very fast. For purpose of achieving the *correction* of the pressure 10^{-6} (the correction *convergence* is compared to the hydrostatic pressure at the same depth), 12 iterations are more than adequate for each time step.

Calculations related to experiment #14 take longer time: its duration at the laboratory is longer and when performing calculations more layers in vertical direction are required as the flow deeper. It seems that high computation efforts are the reason why we have not found any publications where any experiment described in the report by Sheppard (2003) would be reproduced using a numerical model. Nevertheless, application of GPU (Prokofyev, 2017) allows to simulate experiment #14 as well within 7 days of computation, which is quite acceptable. In this case, only 14% (1.5Gb) of GPU RAM were loaded.

The dynamics of the scour hole depth obtained as a result of numerical simulation of the maximum depth per the computation domain is given in Fig. 5-6. It also contains symbols corresponding to the experimental data by Sheppard (2003). In general, the agreement may be considered good, and in case of experiment #14 it is almost full. The highest disagreement with the test results is observed at the scour initial phase: it reaches about 10% in case of experiments #3, #4 and #7. The final depth of the scour hole is calculated better: the error is up to 5% in case of experiments #3 and #14, and in case of #4 and #7 it is negligible. The average curve slope, namely the calculated erosion rate agrees well with the experimental data. The scour curve pulsations for experiment #4 in Fig. 5 are related to the movement of riffles on the scour hole bed; a 3D visualization of transformations is referred to in (Prokofev, 2019). For clarity, Fig. 5-6 contains the second curve (lower continuous line): it refers to scour dynamics at a fixed point $x = -0.41$ m, $y = +0.41$ m,, which means approximately in the score hole focus – near the cylinder front at the angle of 45º from the axis of the hydraulic flume. There, these bed scour pulsations manifest themselves more, as compared to the upper curve of the maximum scours.

It is interesting that in case of experiment #14 the sand is 13 times finer as compared to #7: the range of grain diameters is quite wide. Nevertheless, we managed to achieve good agreement between the calculation results and the data gathered in each of the four experiments, without changing the empirical parameters selected during the primary (*single*) calibration during *test 3*.

The choice of the boundary conditions type for the k, ε turbulence parameters on the free surface has little influence on the results of *tests 3 and 4*. The role of suspended sediments (considered by us) is insignificant, in the course of numerical research by Ahmad et

al. (2014) in respect of bed scours near the cylinder $D = 0.2$ m with sand $d_{50} = 0.92$ mm, suspended sediments were not taken into account at all.

V. CONCLUSIONS

The use of even the simplest empirical formulas for sediment transport in 3D numerical models in combination with the modern computation technologies (OpenCL, CUDA) allows to simulate complicated scours of a movable bed within a reasonable time period ensuring sufficient accuracy.

The algorithm described herein can find practical use in forecasting of local scours in proximity to bridge supports, breakwater pier heads, in a hydrosystem's tail races after the bottom spillways, and other tasks where three-dimensional current effects play a significant role. Further direction for research is validation of the algorithm based on the experimental data where the movable bed transformations are also provided by waves (Ahmad et al., 2014). The method included into the software package already allows to perform such calculations (Prokofev, 2017, 2018).

VI. SUPPLEMENTAL DATA

Supporting materials for test calculations of Case 1 involving flowing around the spur-dyke and a test involving the formation of a recirculation zone in case of a flow in the sudden-expanded flume can be accessed from Prokofev (2019). Additional graphical materials, including current plans and bed scour process animation, given in the test Case 4 are available at the same source. Moreover, the text files available referred to in Prokofev (2019) contain the saved data of laboratory experiments for validation of Case 3 and Case 4.

Notation

c = suspended sediment's volumetric concentration (-)
c_m = depth averaged suspended sediment's concentration (-)
c_0 = volumetric concentration at reference level σ_0 (-)
$C_\mu, C_{1\varepsilon}, C_{2\varepsilon}$ = turbulence's model constants (-)
FV = finite volume (mesh cell)
d = sand particle size (m)
d_{50} = median grain size (m)
D_* = dimensionless sand particle size (-)
E = vertical σ- mesh thickening factor (-)
F = bed transformation boost parameter (-)
g = gravity acceleration (m s^{-2})
$\boldsymbol{G}$ = bed slope gradient vector (-)
h = flow depth (m)
k = turbulence kinetic energy, TKE (m^2s^{-2})
k_s = Nikuradse's roughness height (m)
K = Von Karman's constant = 0.41 (-)
L = vertical σ- mesh layers amount (-)
M_e = sediment's mobility parameter (-)
n = Manning formula's friction coefficient ($m^{-1/3}s$)

London Journal of Engineering Research

q_b = bedload sediment transport rate (m^2s^{-1})
q_s = suspended load sediment transport rate (m^2s^{-1})
p = packed sand bed porocity (-)
$Prod$ = TKE generation source term (m^2s^{-3})
t = time (s)
T = water temperatute (ºC)
T_m = tangent of the steepest slope angle (-)
$\boldsymbol{u}$ = liquid current velocity vector $[u_1, u_2, u_3]$ ($m\ s^{-1}$)
U_* = bed shear velocity ($m\ s^{-1}$)
$\boldsymbol{V}$ = current velocity vector in a near-bed calculation layer ($m\ s^{-1}$)
$\overline{V}$ = depth averaged current velocity ($m\ s^{-1}$)
$V(\sigma)$ = vertical profile of the longitudional current velocity ($m\ s^{-1}$)
V_{CR} = depth averaged critical velocity ($m\ s^{-1}$)
V_{lift} = lifting velocity for a suspended particles: erosion rate ($m\ s^{-1}$)
V_{lift}^0 = lifting velocity at the reference level σ_0 ($m\ s^{-1}$)
w = sand particle fall velocity ($m\ s^{-1}$)
x, y, z = coordinates (m)
z^+ = distance from the bed to the nearest mesh node (m)
z_0 = bed roughness parameter (m)
β_n = calibration factor for bedload transport formula (-)
$\Delta x, \Delta y$ = mesh cell (FV) sizes for x and y directions (m)
ε = TKE dissipation rate (m^2s^{-3})
θ_{CR} = critical Shields parameter (-)
ν = water kinematic viscosity (m^2s^{-1})
ν_t = eddy viscosity (m^2s^{-1})
ρ = water density ($kg\ m^{-3}$)
ρ_s = sediment grains density ($kg\ m^{-3}$)
σ = dimensionless vertical coordinate [0…1] (-)
σ_0 = dimensionless reference level (-)
σ_k, σ_ε = turbulence's model constants (-)
τ = bed shear stress ($N\ m^{-2}$)
φ_ρ = relative density (-)
χ_{max} = steepest slope angle before grains slide by themselves (deg)

REFERENCES

1. Abdelaziz, S., Bui, M.D., Rutschmann, P. (2010). Numerical simulation of scour development due to submerged horizontal jet. *River Flow - Dittrich, Koll, Aberle & Geisenhainer (eds), Bundesanstalt für Wasserbau, ISBN 978-3-939230-00-7,* 1597-1604.
2. Ahmad, N., Bihs, H. , Kamath, A., Arntsen, Ø.A. (2014). 3D Numerical modelling of pile scour with free surface profile under waves and current using the level set method in model REEF3D. 8p. Retrieved from http://eprints.hrwallingford.co.uk/1575/1/PA_3_20-Ahamd-N.pdf.

3. Amoudry, L. (2008). A review on coastal sediment transport modelling. *Proudmat Oceanofgaphic laboratory, #189*. Retrieved from http://nora.nerc.ac.uk/id/eprint/8360/1/POL_ID_189.pdf
4. Audusse, E., Bristeau, M-O., Perthame, B., Sainte-Marie, J. (2011). A multilayer Saint- Venant system with mass exchanges for shallow water flows. Derivation and numerical validation. *ESAIM: M2AN, v.45(1),* 169-200. Retrieved from https://arxiv.org/pdf/0901.3887.pdf
5. Belov, I.A., Kudriavtsev, N.A. (1987). *Teplootdacha i soprotivlenie paketov trub [Heat transfer and resistance of pipe packages]*. Leningrad, RUS: Energoatomizdat, 223p.
6. Chatterjee, S.S., Ghosh, S.N., Chatterjee, M. (1994). Local scour due to submerged horizontal jet. *Journal of Hydraulic Engineering, 120(8),* 973-992.
7. COHERENS. (n.d.) Chapter 7. Sediment transport model. *Royal Belgian Institute of natural science*. Retrieved from https://odnature.naturalsciences.be/downloads/coherens/documentation/chapter7.pdf
8. Delft3D-FLOW. (2005). Chapter 11: 3D Sediment transport and morphology. *User manual. Delft hydraulics*. Retrieved from ftp://ftp.coastal.la.gov/Whiskey%20Island/TE-47/Appendix%20A%20-%20D3D%20Sediment%20transport%20and%20morphology.pdf.
9. Fe, J., Navarrina, F., Puertas, J., Vellando, P., Ruiz, D. (2000). Experimental validation of two depth averaged turbulence models. *International Journal for Numerical Methods in Fluids,* 00:1-6, 25p.
10. Kim, H.S., Roh, M., Nabi, M. (2017). Computational modeling of flow and scour around two cylinders in staggered array. *Water, 9(654),* 19p.
11. Kulikovskii, A.G., Pogorelov, N.V., Semenov, A.IU. (2001). *Matematicheskie voprosy chislennogo resheniia giperbolicheskikh system uravnenii [Mathematical problems of numerical solution of the hyperbolic systems of equations]*. Moscow, RUS: Fizmatlit, 608p.
12. Kuzmin, D., Mierka, O., Turek, S. (2007). On the implementation of the κ-ε turbulence model in incompressible flow solvers based on a finite element discretization. *International Journal of Computing Science and Mathematics, vol. 1(2)*. DOI: 10.1504/IJCSM.2007.016531.
13. Lin, P., Liu, P.L.-F. (1998). A numerical study of breaking waves in surf zone. *Journal of Fluid Mechanics, vol.359*. 239-264.
14. Ma, G., Shi, F., Kirby, J.T. (2012). Shock-capturing non-hydrostatic model for fully dispersive surface wave processes. *Ocean Modeling, vol.43-44*. 22-35.
15. Meyer-Peter, E., Müller, R. (1948). Formulas for bed load transport. *Stockholm: Proc. 2nd Meeting International Association of Hydraulic Research*. 39–64.
16. Prokofev, V. (2018). Multilayer open flow model: A simple pressure correction method for wave problems. *International Journal for Numerical Methods in Fluids, vol.86(8)*. 518- 540.
17. Prokofev, V. Supporting materials. (2019) : http://gofile.me/2Zesj/xH3BDPpqv
18. Prokofyev, V.A. (2017). GPU utilization for speed up the solution of the three-dimensional engineering tasks of open flows hydraulics. *Matematicheskoe modelirovanie [Mathematical modeling], vol.29(8)*. 74-94. http://mi.mathnet.ru/eng/mm/v29/i8/p74
19. Rajaratnam, N., Nwachukwu, B.A. (1983). Flow near groin-like structures. *Journal of Hydraulic Engineering, 109(3)*. 463-481.
20. Rodriguez-Cuevas, C., Couder-Castañeda, C., Flores-Mendez, E., Herrera-Díaz, I.E., Cisneros-AlmazanR. (2014). Modelling shallow water wakes using a hybrid turbulence model. *Journal of Applied Mathematics, ID 714031*. 10p.
21. Sheppard, D.M. (2003). Large scale and live bed local pier scour experiments. Phase1: large scale, clear water scour experiments. *Final report. University of Florida*, 199p. Retrieved from https://fdotwww.blob.core.windows.net/sitefinity/docs/default- ource/content/structures/structuresresearchcenter/final- reports/bb473_rpt1.pdf?sfvrsn=d9346f23_0

22. Soulsby, R. (1997). *Dynamics of marine sands*. London: Thomas Telford Publications.
23. Stelling, G., Zijlema, M. (2008). Efficient computation of surf zone waves using the nonlinear shallow water equations with non-hydrostatic pressure. *Coastal Engineering, vol.55*. 780- 790.
24. Török, G.T., Baranya, S., Rüther, N. (2017). 3D CFD modeling of local scouring, bed armoring and sediment deposition. *Water, 9(56)*. 23p.
25. Van Rijn, L.C. (2012). Simple general formulae for sand transport in rivers, estuaries and coastal waters [Monograph]. Retrieved from http://www.leovanrijn-sediment.com/papers/Formulaesandtransport.pdf
26. Violeau, D., Issa, R. (2007). Numerical modelling of complex turbulent free-surface flows with the SPH method: an overview. *International Journal for Numerical Methods in Fluids, vol.53*. 277-304.
27. Voltsinger, N.E., Klevannyi, K.A., Pelinovskii, E.N. (1989). *Dlinnovolnovaia dinamika pribrezhnoi zony [Long-wave dynamics of the coastal zone]*. Leningrad, RUS: Gidrometeoizdat, 273p.
28. WAQUA/TRIWAQ (n.d.) - two- and three-dimensional shallow water flow model. Technical documentation. *SIMONA report #99-01, Rijkswaterstaat*. Retrieved from http://simona.deltares.nl/release/doc/techdoc/waquapublic/sim1999-01.pdf
29. Wei, G., Brethour, J., Grünzner, M., Burnham, J. (2014). Sedimentation scour model. *Flow Science report, #03-14*. Retrieved from. https://www.flow3d.com/wp-content/uploads/2014/06/Sedimentation-Scour-Model.pdf
30. Wu, W., Wang, P., Chiba, N. (2004). Comparison of five depth-averaged 2-D turbulence models for river flows. *Archives of Hydro-Engineering and Environmental Mechanics, vol.51(2)*. 183-200.
31. Zhou, Lu. (2017). Numerical modelling of scour in steady flows. *These de doctorat, Ecole Doctorale #162*. Lyon: L'Universite de Lyon. Retrieved from https://tel.archives-ouvertes.fr/tel-01598600/file/TH_T2567_lzhou.pdf

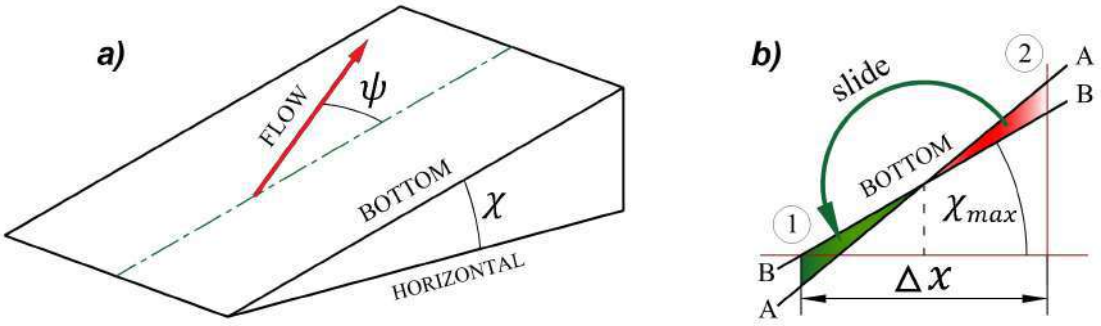

Figure 1: a) diagram of inclined bed for the adjustment of the Shields critical parameter using Soulsby's formula (21); b) the bed slope slide A-A with an angle higher than the steepest slope angle χ_{max} into the stable position B-B; the FV cell face is shown with a dotted line

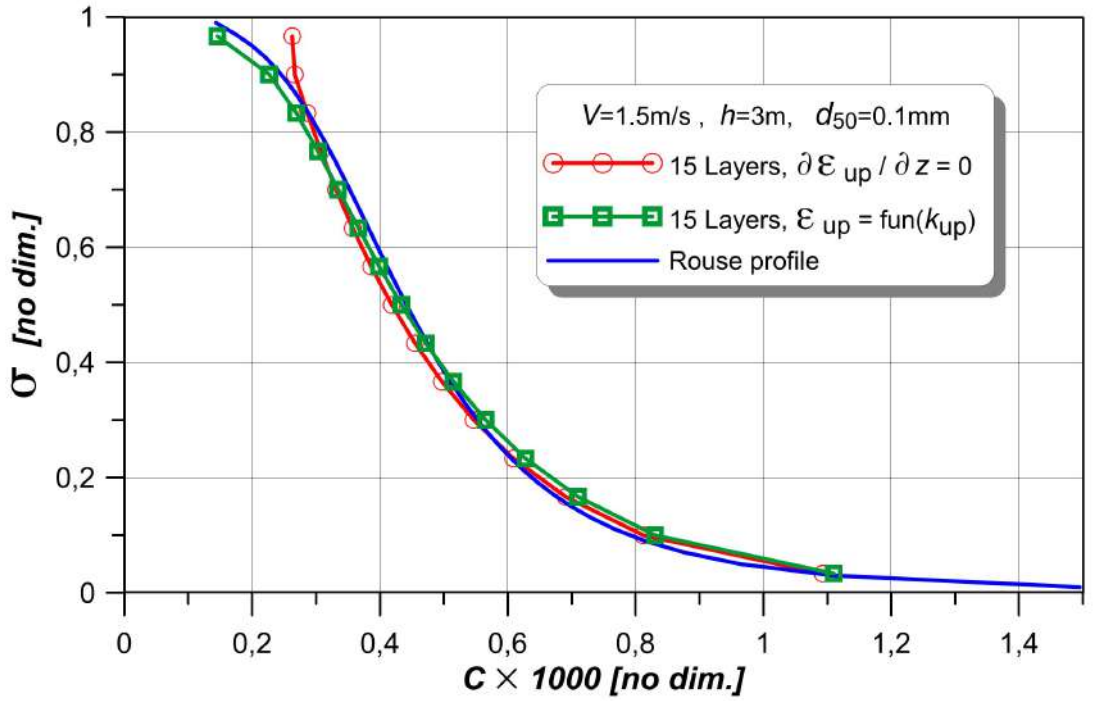

Figure 2: Steady state depth distribution of the suspended particles volumetric concentrations in uniform flow for various calculation schemes

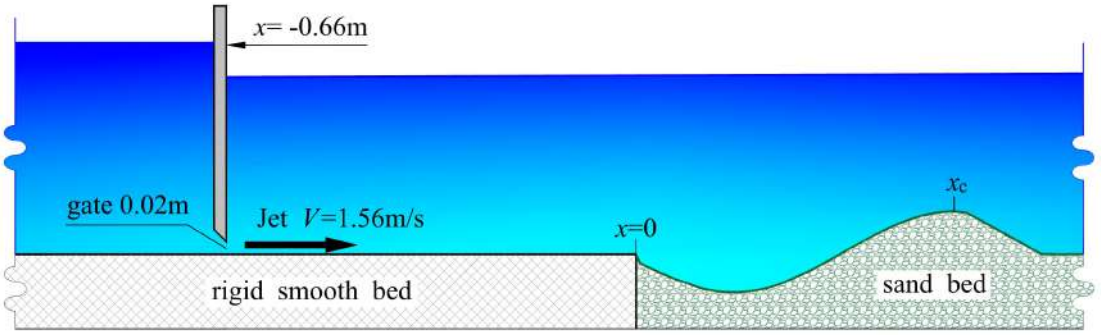

Figure 3: Design of the laboratory experiment by Chatterjee et al. (1994); the scales along x and z are the same; the bed computation profile corresponding to a 30 minute time period is used on the right

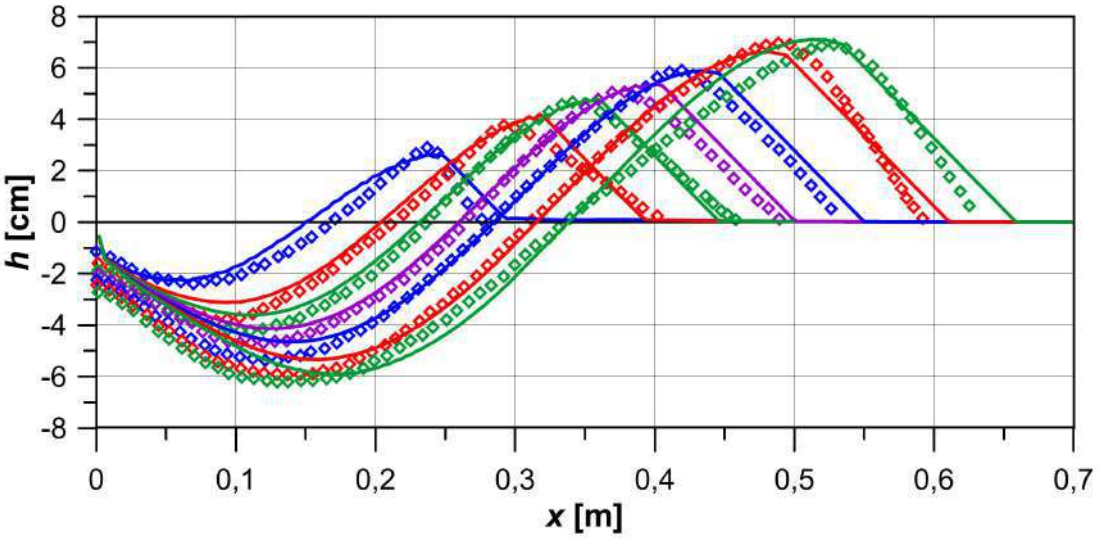

Figure 4: Longitudinal profiles of a movable bed for the time periods of 1, 3, 5, 8, 12, 20 and 30 minutes: obtained in a numerical experiment (continuous lines) and registered in the hydraulic flume by Chatterjee et al. (1994) (squares)

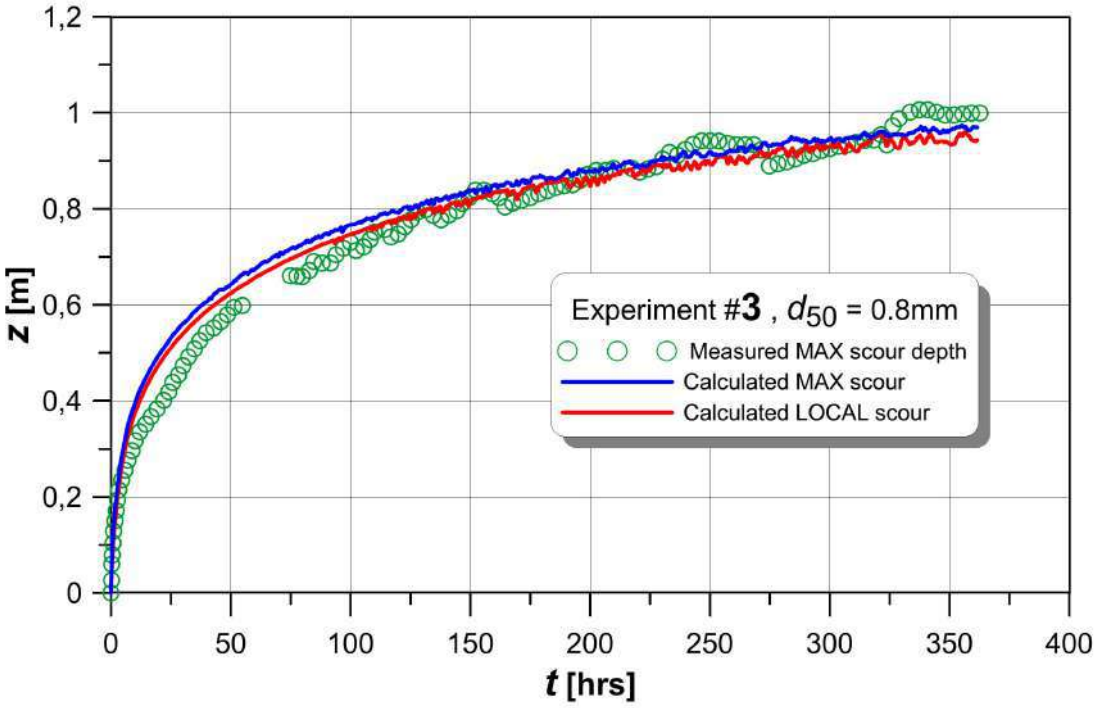

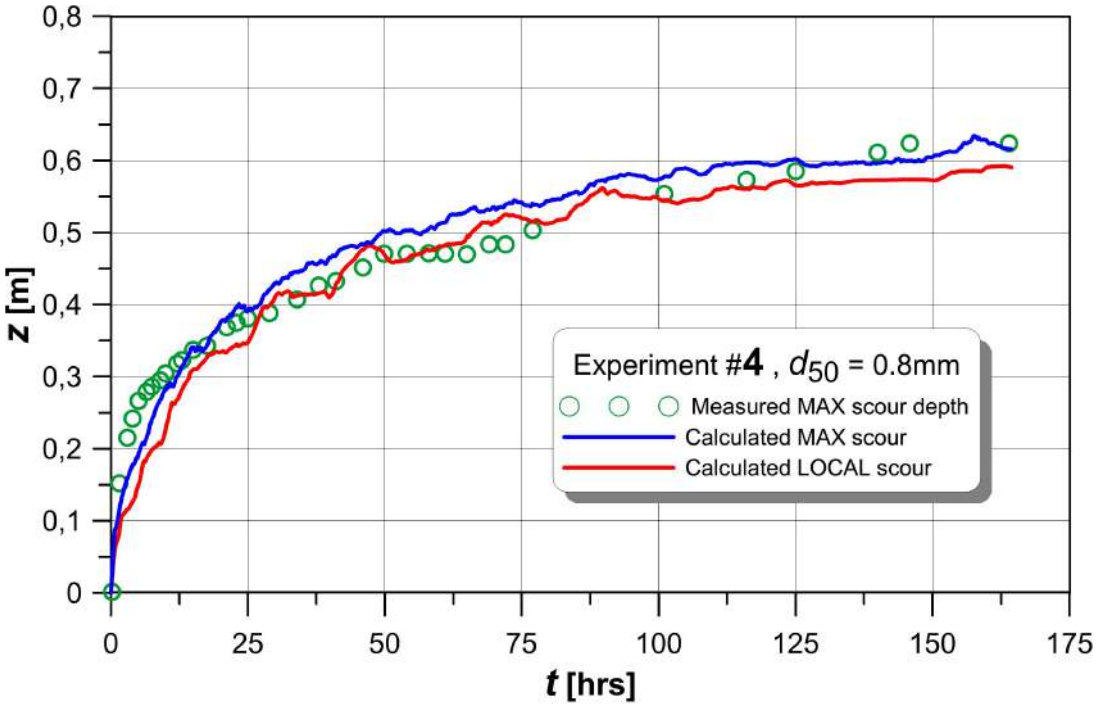

Figure 5: Simulation of bed scour dynamics near the circular pile D = 0.915 m for experiments #3, #4 from Sheppard's (2003) report; upper continuous line – maximum scour depth per the computational domain, lower line – scour depth at the fixed point x = ⁑ 0.41 m, y = +0.41 m

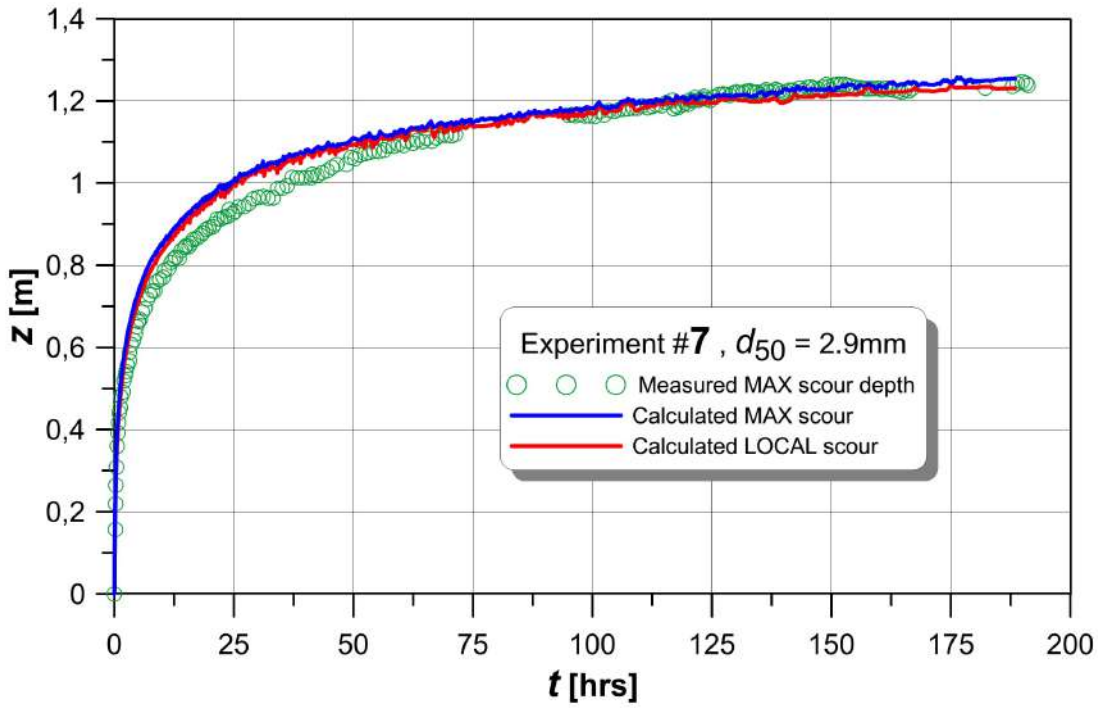

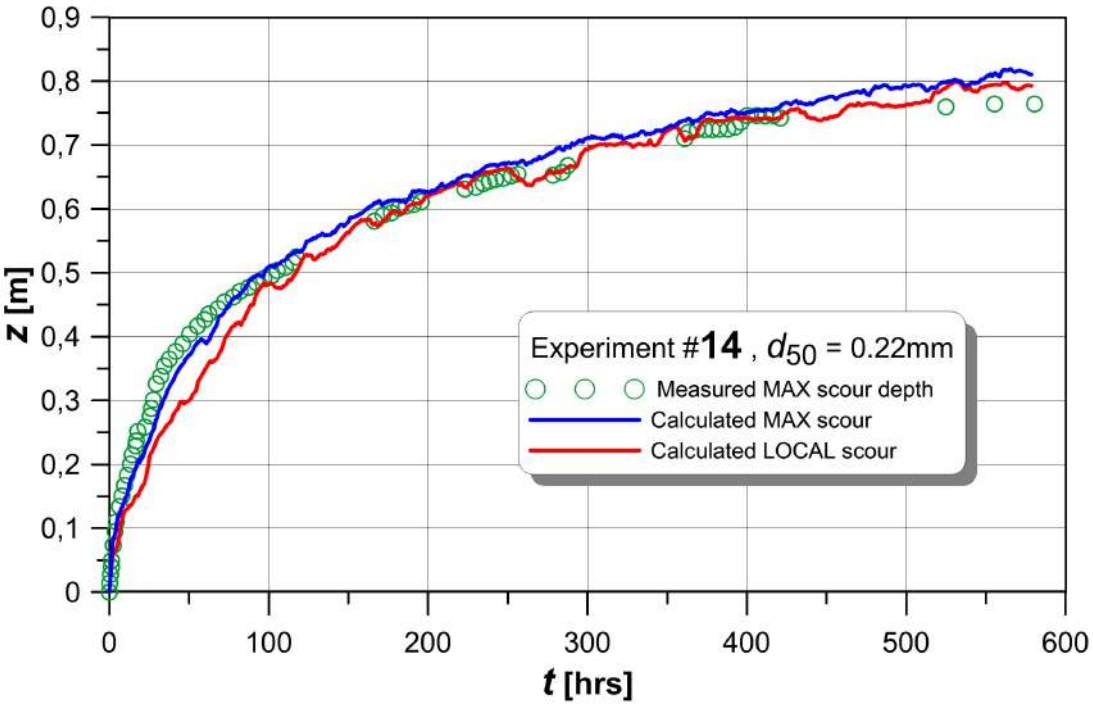

Figure 6: Simulation of bed scour dynamics near the circular pile experiments #7 and #14 from Sheppard's (2003) report D = 0.915 m for

FTIR Spectra Analysis of Zinc Substituted Barium Nickel Ferrite

Sadiq. H. Khoreem, A. H. AL-Hammadi & W. F.Al-Eryani

Sana'a University

ABSTRACT

Nano - crystalline BaNix-2ZnxFe16O27 (where x = 0.0, 0.4, 0.8, 1.2, 1.6, and 2.0) w-type hexa-ferrite samples were generated using the typical standard ceramic methodology. Fourier transform infrared spectroscopy (FTIR) is a method which is used to identify the characteristic functional groups from the spectral bands that allow us to know the conjugation between the nanoparticles and the adsorbed biomolecules. It is used to detect different functional groups in Barium ferrites. The FTIR spectrum is recorded between 400 and 4000 cm−1. The result shows the two main bands of absorption. The high-frequency band in the range 550-600 cm- 1 and a low-frequency band at around 400 cm-1 were assigned to tetrahedral v1 and octahedral v2 sites, respectively, which illustrated the formation of the ferrite phase.

Keywords: barium nickel ferrite; ftir spectra; Debye temperature; force constants.

Classification: DDC Code: 543.56 LCC Code: QD96

Language: English

London Journals Press

LJP Copyright ID: 392924
Print ISSN: 2631-8474
Online ISSN: 2631-8482

London Journal of Engineering Research

Volume 22 | Issue 8 | Compilation 1.0

FTIR Spectra Analysis of Zinc Substituted Barium Nickel Ferrite

Sadiq. H. Khoreem [α], A. H. AL-Hammadi[σ] & W. F.Al-Eryani[ρ]

ABSTRACT

Nano - crystalline BaNix-2ZnxFe16O27 (where x = 0.0, 0.4, 0.8, 1.2, 1.6, and 2.0) w-type hexa-ferrite samples were generated using the typical standard ceramic methodology. Fourier transform infrared spectroscopy (FTIR) is a method which is used to identify the characteristic functional groups from the spectral bands that allow us to know the conjugation between the nanoparticles and the adsorbed biomolecules. It is used to detect different functional groups in Barium ferrites. The FTIR spectrum is recorded between 400 and 4000 cm^{-1}. The result shows the two main bands of absorption. The high-frequency band in the range 550-600 cm^{-1} and a low-frequency band at around 400 cm^{-1} were assigned to tetrahedral ν_1 and octahedral ν_2 sites, respectively, which illustrated the formation of the ferrite phase.

These two prominent bands are attributed to the intrinsic vibrations of tetrahedral and octahedral metal- oxygen bands in the crystal lattices of the BaNix-2ZnxFe16O27 hexagonal ferrite, respectively high frequency and low-frequency band . These two prominent peaks indicate the formation of hexa-ferrite. The stretching vibrations of metal-oxygen bonds is the reason for these peaks. The force constants (F_{Cons}) were calculated for tetrahedral F_{tet} sites and octahedral F_{oct} sites and were found to decrease with increasing Zn ions. The observed decrease in θ_D with zinc concentration suggests enhancement of the lattice vibrations due to Zn substitution. It can be seen that θ_D decreases with increasing Zn concentration.

Keywords: FTIR Spectra; Barium-Nickel ferrite; Debye temperature; Force constants.

Author α: Department of Optical and Vision Sciences, Faculty of Medicine, Al-Razi University, Sanaa, Yemen.

σ: Physics Department, Faculty of Science, Sana'a University, Sana'a, Yeme.

ρ: Physics Department, Faculty of Science, Saada University, Saada, Yemen.

I. INTRODUCTION

The improvement of ferrite nanoparticles' electrical and magnetic properties, as well as their good physical features, has given them confidence and the ability to have a lot of interest in their study. The w- type Hexa-ferrites have been used in a wide range of scientific, technological, and industrial applications, including those for humidity sensors, recording disks, microwave devices, catalysts, information storage, magnetic resonance imaging, ceramic coatings for solar cells, optoelectronic devices, and electronic devices. [1,–2]. Due to their sensible transmission in the optical portion of the spectrum as compared to other categories of materials, the optical characteristics of dielectric materials in general attracted attention. The optical constants, such as the absorption coefficient, transmission, reflection, and index of refraction, are crucial characteristics to explain the optical properties of ferrite materials[1,2].

The optical properties of the dielectric materials generally became of interest because of their Sensible transmission within the optical part of the spectrum as compared with different categories of materials. So that to study the optical properties of the ferrite materials, the optical constant such as absorption coefficient, transmission, reflection, and index of refraction are vital parameters to explain the optical properties of the ferrite materials [3]. The reportable by NARANG et al. about the Ni-Zn ferrites was different by the substitution of Zn^{2+}, ions, which prefer tetrahedral sites, with divalent

metal ions that either adopt octahedral positions or inhibit grain growth, and the magnetic properties were tailored with careful addition [4].

SHAUKAT, S. F., et al. reported the Cr-substituted W-type hexaferrite for the chemical composition (BaNi2CrxFe16-xO27.IR spectrum for sample revealed two well-defined absorption peaks which correspond to tetrahedral A- and octahedral B-sites present in W-type hexagonal lattice [5]. Muajsam, et al. synthesis the Ba-doped Co–Zn ferrite nanoparticles using the sol-gel auto combustion technique. The single-phase formation of the samples with F*d*3m space group was confirmed by X-ray diffraction (XRD) and fourier transformation infrared (FTIR) spectra display presence of two strong peaks around 430 cm^{-1} and 580 cm^{-1} that proved the formation of ferrite structure [6]. The general behavior for the nickel ferrites prefers to occupy the octahedral sites while the zinc prefers to occupy the tetrahedral site. The interactions between the tetrahedral ions and octahedral sites will alter the electrical and magnetic properties of ferrites. The octahedral sites are occupied by Ni^{2+} and $Fe^{3+,}$ whereas the tetrahedral sites are occupied through Zn^{2+} and Fe^{3+}. The properties of the ferrite are also strongly dependent on the synthesis method, sintering temperature, chemical composition, and so on. [7–9]. The infrared spectroscopic technique is based upon the fact that a chemical substance shows marked selective absorption in the infrared region.

Various bands present in the IR spectrum correspond to the characteristic functional groups and bonds present in the chemical substance. The infrared spectra are useful for determining the local symmetry and noncrystalline solids and studying the ordering phenomena in ferrite. In the present study, we investigated and discussed the fourier Fourier transformation infrared (FT-IR) spectra of the BaNix-2ZnxFe16O27 Hexagonal ferrites, where x = 0.0 ,0.4 0.8, 1.2, 1.6 and 2) 1.0 in the step of 0.20, which have been synthesis by the ceramic method.

II. MATERIALS AND METHODS

The samples used in this work had been prepared by the well-known ceramic method. with a high purity of BaCO3, ZnO, NiO, and Fe2O3 had been mixed according to their molecular weight ratio to obtain different compositions according to the following relation.

BaCo3+(2-x)(NiO)+x(ZnO)+8Fe2O3-»BaNi(2-x) .ZnxFe16O27+CO2↑

where x = 0.0, 0.4, 0.8, 1.2, 1.6, and 2. The weights of the mixed oxides in grams for each composition of the prepared system BaNi2-xZnxFe16O27. The oxides have been mixed and ground to a fine powder using a gate mortar made of carborundum for one hour for each sample, and then each sample was grounded again for five hours using a mechanical grinding machine. The mixture powder was pre-sintered in the air at 950 °C± 10°C for six hours after which it slowly cooled to room temperature. The aggregate was grounded again for five hours for each sample with the usage of the mechanical grinding gadget to get a totally nice powder. After that it was sintered at 1250°C± 10°C for 4 hours and slowly cooled to room temperature. The samples were made according to the technique of Stimson and Schiedt; 2.5 mg of the ferrite was mixed with 0.8 g of powdered KBr, and placed in a cylindrical die of 20 mm diameter. Then pressed for about 10 min at 18 tons/cm^2. C1ear disks of approximately 1 mm thickness were obtained with the usable transmission. FT-IR spectra of finely fine powder of all the compositions were recorded in the range of 4000 cm^{-1} to 400 cm^{-1}, measurements were made at room temperature.

III. RESULTS AND DISCUSSION

The formation of the surface functional group was confirmed by IR spectroscopy. To detect the metal-oxygen bond of the formed hexagonal BaNix-2ZnxFe16O27 phase materials, A few milligrams of BaNix-2ZnxFe16O27 powder mixed with anhydrous KBr powder and made in the form of a pellet for measurement. The FT-IR spectra were analyzed in the wavenumber range between 4000 and 400 cm^{-1} for the samples

shown in Figure 1. Generally, Figure 1. and Table.1, displays that each one the samples have M – O (metallic-oxygen) bond and the C = O bond. This proves a bond between the Fe, Ba, Ni, and Zn metals with oxygen in the specimen. The sample exhibits absorption bands from the ferrite compounds. Generally, two significant peaks can be observed at (430 - 439.69 &580 - 595 cm^{-1}) are observed. The peaks appearing between 400 and 600 cm^{-1} are the result of the vibration of metal-oxygen bond, which gives the idea of the formation of the ferrite phase[10].

These two prominent bands are attributed to the intrinsic vibrations of tetrahedral and octahedral metal- oxygen band in the crystal lattices of the Ba Nix-2 Zn Fe 16 27 hexagonal ferrite, respectively high frequency and low-frequency band [11-13]. These two prominent peaks indicate the formation of hexaferrite. The stretching vibrations of metal-oxygen bonds is the reason for these peaks.

The absorption peak at 1430 cm^{-1} is due to C–O asymmetric stretching vibration in the BaCO3. The absorption bands peaks around 1624cm^{-1} and 3449 cm^{-1} are due to stretching vibrations of water mode O-H. The H–O–H and O–H stretching vibration at wavenumbers around 3342 cm^{-1} and 1664 cm^{-1} due to the water and polyol in the precursor [14,15]. Bands located at 3435 cm^{-1} and 1590 cm^{-1} are due to the presence of O-H stretching vibration of (O– H) group of residual water and anti-symmetrical stretching vibration of CO2, respectively [16]. Also are assigned to stretching and bending vibration of H2O absorbed from the atmosphere when the samples were kept and ground in the air due to the high surface area of these materials [17]. The peak at 2348 cm^{-1} occurs as a result of the presence of CO2 in the prepared sample [18].

The absorption band at 2900 cm^{-1} is assigned to the C–H stretching vibration [19]. The band positions v1-v2 increase slightly as x increases; this is due to the fact that Zn^{2+} is lighter atomic weight compared to host Ni^{2+}, and that the wavenumber is inversely proportional to the atomic weight [20].

3.1 Force constants

The variation in wavenumbers (ν_1& ν_2) with zinc concentration(x) for all samples is shown in Figure 2.a. From the figure.2.a, it has been observed that the ν_2 shift towards lower frequencies however, ν_1 shift towards higher frequencies with zinc concentration (x) is expected because of a large ionic radius of Zn^{2+} ion samples [21]. The values of the force constants (Ftet and Foct) for the band Fe^{3+} - O^{2-} at tetrahedral and octahedral sites are calculated using the relation [22,23].

$$Ftet = 4\,\pi^2 c^2 \nu_1^2\,\mu \quad (1)$$

$$Foct = 4\pi^2 c^2 \nu_2^2 \mu \quad (2)$$

where Ftet is the tetrahedral force constant and Foct is the octahedral force constant, and c=2.99x10^{10} cm/s, is the speed of light, whereas ν_1 and ν_2 is the band wavenumber in cm^{-1} and μ is the reduced mass for Fe^{3+} ions and O^{2-} ions (2.061x10^{-23} g).

The values of force constant for tetrahedral (Ftet) and octahedral (Foct) sites are listed in Table 1. The variety in force constant with zinc concentration(x) for all samples at tetrahedral and octahedral sites was displayed in Figure 2.b.

From the figure.2.b, it is observed that Ftet declines with an increase in zinc ion concentration. This conduct can be attributed to the variety in cation oxygen bond length [24].

Since the bond length (A-O) increased with an expansion in zinc concentration, the energy required to break longer bonds is less, supporting a decrease in the force constant of tetrahedral sites.

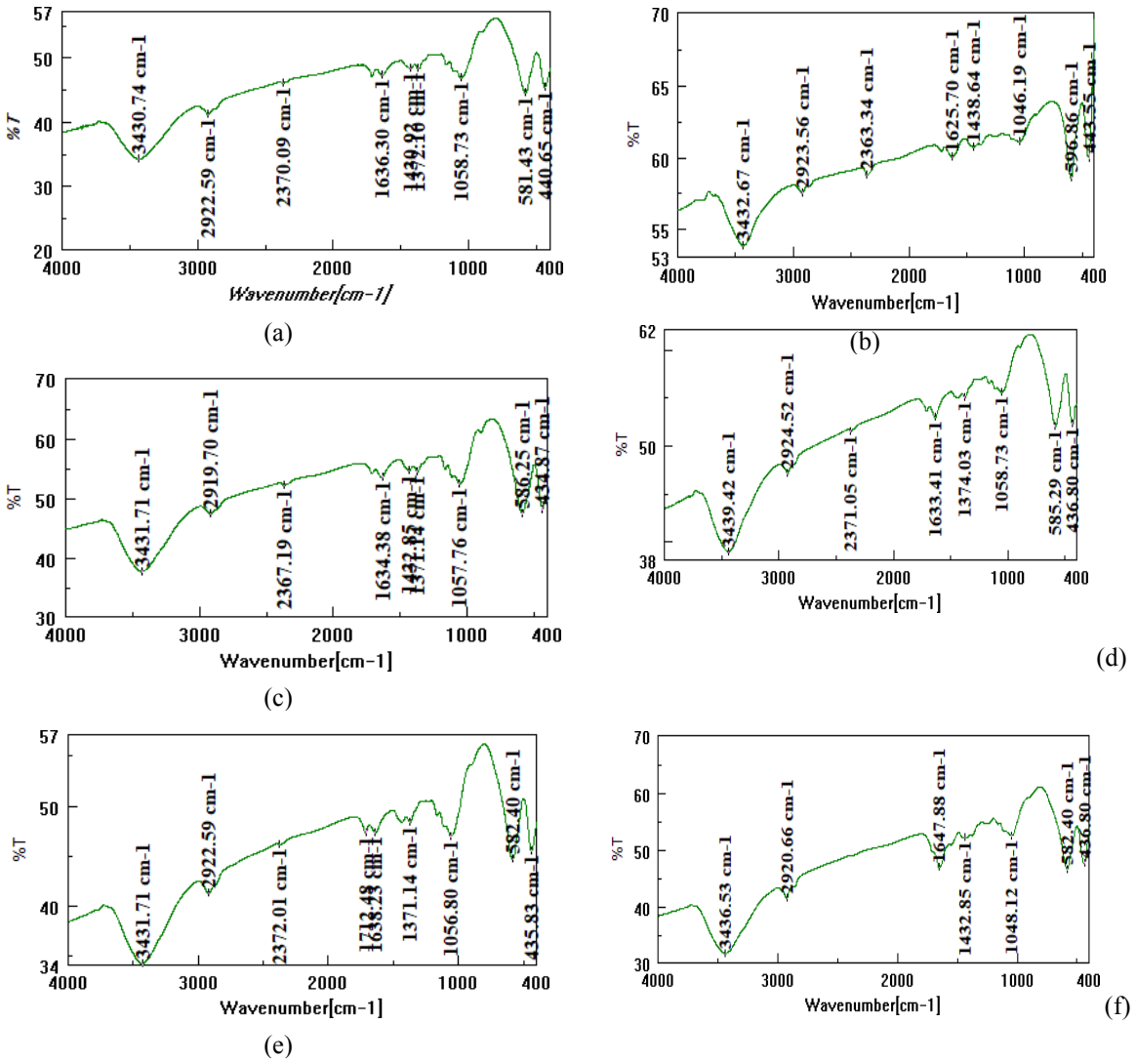

Figure 1: (a,b,c,d,andf) IR pattern BaNix-2ZnxFe16O27 (x = 0, 0.4, 0.8, 1.2, 1.6 & 2) ferrites. (a) x=0.0; (b) x=0.4;. (c) x=0 .8; (d) x=1.2; (e) x=1.6; (f) x=2.0

The change in the band position is due to the change in the Fe^{3+}-O^{2-} internuclear distances for the tetrahedral and octahedral sites, respectively [25,26]. Normally, it is expected that a rise in band length ought to result in a decrease in force constant. If the radius of the impurity ion is larger than the displaced ion, then the bond length increases, lowering the force constant for either site or a reduction in the repulsive forces between the ions leading to lower electrostatic energy implying a lower wavenumber. The reverse will hold if a smaller impurity ion replaces a metal ion of the regular lattice. A decrease in wavenumber and force constant is expected with zinc substitution because of its larger ionic radius(0.74Å) than the displaced Ni^{2+} ion (0.69 Å) [14]. The positions of absorption bands in terms of wavenumber vtet and voct for all samples are summarized in table_ 1. From Table 1, it is clear that the position of the vtet and voct band is shifted with the incorporation of Zn ions in the Ni matrix. The same behavior was reported in previous work of different ferrite systems [27,28]. FT-IR results clearly indicate that Ni ions are stabilized in the Oh crystal field, whereas Zn ions prefer Td sites because of their ability to form covalent bonds [29-32]. The small shift in band positions for Ba-Zn-Ni ferrites is observed as a function of Zn content (x) (Table 1), and it may be caused by differences in the ionic distances Fe B-O and Fe A-O, which are equal to 0.199 nm and 0.189 nm respectively [33]. This reason can also cause the stronger covalent bonding of Fe^{3+} ions at the tetrahedral sites than at the octahedral sites.

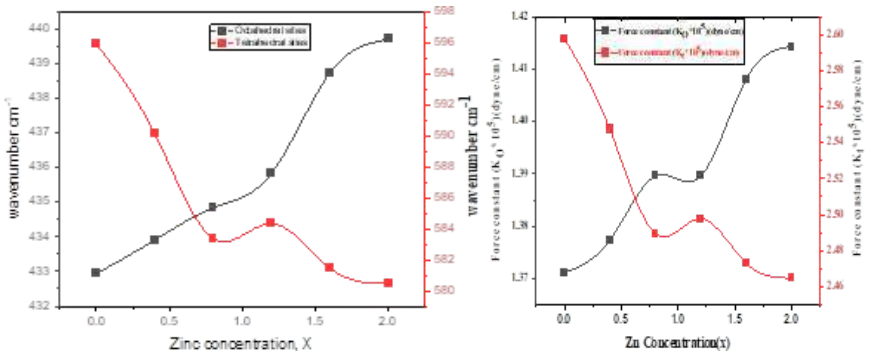

Figure 2: (a)Variation of wave numbers at A and B sites with zinc concentration. (b) force constants with Zinc concentration (x) at tetrahedral and octahedral site.

Debye temperature is an essential parameter to study lattice vibrations [34]. The Debye temperature (θD) for BaNix-2ZnxFe16O27 (x = 0, 0.4, 0.8, 1.2, 1.6, 2) ferrites was obtained by using the next relation [35,36]

$$\theta_D = \frac{hc\nu_{av}}{K_B}$$

where h is Plank constant (h = 6.626 ×10^{-34} J.s), KB is Boltzmann constant (KB =1.3806×10^{-23} J K^{-1}), c is velocity of light (c =2.99 ×10^{10} cm s^{-1}) and vav is average wave-number of bands (cm^{-1}).

The calculated values of the debye temperature (θD)for the samples are depicted in figure.3. It can be noticed that with increasing zinc content θD decreases from 738.19 K (for x = 0.0; to 731.96 K (for x = 1.2), and after that remains constant. These values have a great importance to determine the conduction mechanism of these ferrites. It can be linked to a decrease in wavenumber of the peak usually attributed to Me-O bond vibration in the tetrahedral site. The observed decrease in θD (Table 1) with zinc concentration suggests enhancement of the lattice vibrations due to Zn-substitution. It can be seen that θD decreases with increasing Zn concentration.

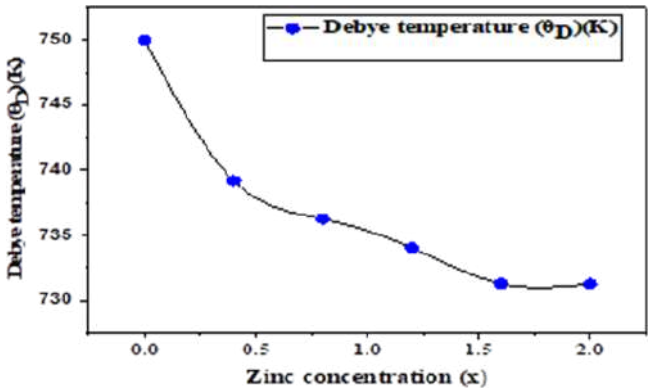

Figure 3: Variation Debye temperature (θ_D)(K)with increasing Zinc concentration (x)

These behaviors can be discussed based on a specific heat theory. According to this theory, electrons absorb part of the heat and θD may decrease with increasing zinc ions concentration; this suggests that the conduction for these samples is due to electrons (i.e., n- type) [37].

Table 1: Calculated force constants of tetrahedral and octahedral sites; Debye temperature

Composition	Absorption band (Wave number)	Force constants	Absorption band (Wave number)	Force constants	Debye temperature (θ_D)
x	v_2 (cm^{-1})	F_{octa} dyn/cm (x 10^5)	v_1 (cm^{-1})	F_{tet} dyn/cm (x 10^5)	θ_D (K)
X=0	432.94	1.36139	595.86	2.57910	738.1946
X=0.4	433.905	1.36747	590.111	2.52927	734.7363
X=0.8	434.834	1.37333	583.31	2.47174	730.5597
X=1.2	435.834	1.37965	584.35	2.47992	731.9688
X=1.6	438.726	1.39802	581.43	2.45543	731.9688
X=2	439.69	1.40417	580.49	2.44729	731.96888

IV. CONCLUSIONS

FT-IR spectra of the samples have been analyzed in the frequency range (400-4000) cm^{-1}. The two main bands of absorption corresponding to tetrahedral *v1* and octahedral *v2* were observed, which illustrated the formation of the ferrite phase. The high-frequency band in the range, 550-600 cm^{-1} and a low-frequency band at around 400 cm^{-1} were assigned to tetrahedral *v1* and octahedral *v2* sites, respectively. The force constants were calculated for tetrahedral Ftet sites, and octahedral Foct sites and frequencies show that Kt decreases with tetrahedral bond length and KO increases with octahedral bond length.with increasing Zn ions. Debye temperature (θD) has also been estimated as a function of composition at room temperature using FTIR spectra. The behavior of Debye temperature θ_D showed that electrons should make a significant contribution to the specific heat.

Conflicts of Interest

The authors declare no conflict of interest."

REFERENCES

1. Dhiman, P.; Jasrotia, R.; Goyal, D.; Mola, G.T. Hexagonal Ferrites, Synthesis, Properties and Their Applications. Ferrite: Nanostructures with Tunable Properties and Diverse Applications 2021, 112.
2. Bharati, V.A.; Somvanshi, S.B.; Humble, A.V.; Murumkar, V.D.; Sondur, V.V.; Jadhav, K.M. Influence of trivalent Al–Cr co-substitution on the structural, morphological and Mössbauer properties of nickel ferrite nanoparticles. Journal of Alloys and Compounds 2020, 821, https:// doi.org/10.1016/j.jallcom.2019.153501.
3. Kulkarni, A.B.; Mathad, S.N. Effect of cadmium doping on structural and magnetic studies of Co-Ni ferrites. Science of Sintering 2021, 53, 407-418.
4. Narang, S.B.; Pubby, K. Nickel Spinel Ferrites: A review. Journal of Magnetism and Magnetic Materials 2021, 519, https://doi.org/10.1016/j.jmmm.2020.167163.
5. Rehman, A.u.; Shaukat, S.F.; Haidarah, A.S.; Akhtar, M.N.; Ahmad, M. Synthesis and investigations of structural, magnetic and dielectric properties of Cr-substituted W-type Hexaferrites for high frequency applications. Journal of Electroceramics 2021, 46, 93- 106, https://doi.org/10.1007/s10832-021-00246-7.
6. Batoo, K.M.; Hadi, M.; Verma, R.; Chauhan, A.; Kumar, R.; Singh, M.; Aldossary, O.M. Improved microwave absorption and EMI shielding properties of Ba-doped Co–Zn ferrite. Ceramics International 2022, 48, 3328-3343, https://doi.org/10.1016/j.Ceramint.2021.10.108.
7. Costa, A.C.F.M.; Silva, V.J.; Cornejo, D.R.; Morelli, M.R.; Kiminami, R.H.G.A.; Gama, L. Magnetic and structural properties of NiFe2O4 ferrite nanopowder doped with Zn2+. Journal of Magnetism and Magnetic Materials 2008, 320, e370-e372, https://doi.org/10.1016/j.jmmm.2008.02.159.
8. AL-Hammadi , A.H.; Khoreem , Sadiq H. Investigations on Optical and Electrical Conductivity of Ba/Ni/Zn/Fe16O27 Ferrite Nanoparticles. Biointerface Res Appl Chem 2022, 13, 168, doi:10.33263/BRIAC132.168.

9. Sattibabu, B.; Rao, T.D.; Das, T.; Chatterjee, M.; Bhatnagar, A.K.; Rayaprol, S.; Das, D. Synthesis and magnetic properties of nanostructured Ni1-xZnxFe2O4 (x = 0.4, 0.5 and 0.6). AIP Conference Proceedings 2020, 2269, https://doi.org/10.1063/5.0019566.
10. Tchouang, T.C.T.; Sharma, J.; Mohammed, J.; Kumar, S.; Srivastava, A.K. Effect of temperature on the magnetic properties of nano-sized M-type barium hexagonal ferrites. AIP Conference Proceedings 2017, 1860, https://doi.org/10.1063/1.4990307.
11. Zhang, C.; Shi, J.; Yang, X.; De, L.; Wang, X. Effects of calcination temperature and solution pH value on the structural and magnetic properties of Ba2Co2Fe12O22 ferrite via EDTA-complexing process. Materials Chemistry and Physics 2010, 123, 551-556, https://doi.org/10.1016/ j.matchem phys.2010.05.013.
12. Ramzan, M.; Arshad, M.I.; Mahmood, K.; Amin, N.; Khan, M.I.; Iqbal, F.; Ajaz-un-Nabi, M. Investigation of Structural and Optical Properties of Pr3+-Substituted M-Type Ba–Ni Nano-Ferrites. Journal of Superconductivity and Novel Magnetism 2021, 34, 1759-1764, https://doi.org/10.1007/s10948-020-05751-4.
13. Mosleh, Z.; Kameli, P.; Poorbaferani, A.; Ranjbar, M.; Salamati, H. Structural, magnetic and microwave absorption properties of Ce-doped barium hexaferrite. Journal of Magnetism and Magnetic Materials 2016, 397, 101-107, https://doi.org/10.1016/j.jmmm.2015.08.078.
14. Fatima, N.; Khan, H.M.; Laref, A.; Alhashim, H.H.; Zahid, M.; Nadeem, M.; Akhtar, T.; Anjum, R. Synthesis And Characterization Of Cobalt Substituted W Type Hexagonal Ferrites. Digest Journal of Nanomaterials & Biostructures (DJNB) 2021, 16.
15. Huang, X.; Zhang, J.; Wang, L.; Zhang, Q. Simple and reproducible preparation of barium hexagonal ferrite by adsorbent combustion method. Journal of Alloys and Compounds 2012, 540, 137-140, https://doi.org/10.1016/j.jallcom.2012.05.015.
16. da Costa Lima, R.; Pinho, M.S.; Ogasawara, T. Thermal characterization of the intermediary products of the synthesis of Zn-substituted barium hexaferrite. Journal of Thermal Analysis and Calorimetry 2009, 97, 131, https://doi.org/10.1007/s10973-009- 0256-4.
17. Simonescu, C.M.; Tătăruş, A.; Culiţă, D.C.; Stănică, N.; Butoi, B.; Kuncser, A. Facile Synthesis of Cobalt Ferrite (CoFe2O4) Nanoparticles in the Presence of Sodium Bis (2- ethyl-hexyl) Sulfosuccinate and Their Application in Dyes Removal from Single and Binary Aqueous Solutions. Nanomaterials 2021,11, https://doi.org/10.3390/nano11113128.
18. Davarpanah, E.; Armandi, M.; Hernández, S.; Fino, D.; Arletti, R.; Bensaid, S.; Piumetti, M. CO2 capture on natural zeolite clinoptilolite: Effect of temperature and role of the adsorption sites. Journal of Environmental Management 2020, 275, https://doi.org/10.1016/j.jenvman.2020.111229.
19. Barbe, A.; Mikhailenko, S.; Starikova, E.; Teterev, V. Infrared spectra of 16O3 in the 900 - 5600 cm−1 range revisited: Empirical corrections to the S&MPO and HITRAN 2020 line lists. Journal of Quantitative Spectroscopy and Radiative Transfer 2021, 276, https://doi.org/10.1016/j.jqsrt.2021.107936.
20. Chavan, V.C.; Shirsath, S.E.; Mane, M.L.; Kadam, R.H.; More, S.S. Transformation of hexagonal to mixed spinel crystal structure and magnetic properties of Co2+ substituted BaFe12O19. Journal of Magnetism and Magnetic Materials 2016, 398, 32-37, https://doi.org/10.1016/j.jmmm.2015.09.002.
21. Balavijayalakshmi, J.; Suriyanarayanan, N.; Jayaprakash, R. Effects of sintering on structural and magnetic properties of Cu substituted cobalt–nickel mixed ferrite nanoparticles. Journal of Magnetism and Magnetic Materials 2014, 362, 135-140, https://doi.org/10.1016/j.jmmm.2014.03.005.
22. Raje Shaikh, B.B.; Chishty, S.Q. Auto-ignition synthesis of rare-earth metal-doped Ni– Zn spinel ferrites for electronic applications. Journal of Materials Science: Materials in

Electronics 2021, 32, 23999-24010, https://doi.org/10.1007/s10854-021-06863-w.
23. Chacko, B.; Roy, A.; Melbin Richard, A.; Swathy, J.; Avanish, B.T.; Madhuri, W. Bismuth modified zinc ferrites for low-temperature ceramic co-firing technology. Materials Chemistry and Physics 2022, 276, https://doi.org/10.1016/j.matchemphys.2021.125401.
24. Ladgaonkar, B.P.; Kolekar, C.B.; Vaingankar, A.S. Infrared absorption spectroscopic study of Nd3+ substituted Zn-Mg ferrites. Bulletin of Materials Science 2002, 25, 351- 354, https://doi.org/10.1007/BF02704131.
25. Shannon, R.D. Revised effective ionic radii and systematic studies of interatomic distances in halides and chalcogenides. Acta Crystallographica Section A 1976, 32, 751-767, https://doi.org/10.1107/S0567739476001551.
26. Warhate, V.V.; Badwaik, D.S.; Chopne, S.R. Thermal and infrared spectral analysis of TiCo doped NiZn Y-type strontium hexaferrite synthesized by sol gel auto-combustion. Materials Today: Proceedings 2020, 29, 1055-1058, https://doi.org/10.1016/j.matpr.2020.04.712.
27. Abou-Elsaad, N.I.; Nawara, A.S.; Mazen, S.A. Synthesis, structural characterization, and magnetic properties of Ni–Zn nanoferrites substituted with different metal ions (Mn2+, Co2+, and Cu2+). Journal of Physics and Chemistry of Solids 2020, 146, https://doi.org/10.1016/j.jpcs.2020.109620.
28. Abul-Magd, A.A.; Morshidi, H.Y.; Abdel-Ghany, A.M. The role of NiO on the structural and optical properties of sodium zinc borate glasses. Optical Materials 2020, 109, https://doi.org/10.1016/j.optmat.2020.110301.
29. Dawoud, H.A.; Abu Ouda, L.S.; Shaat, S.K. FT-IR studies of nickel substituted polycrystalline zinc spinel ferrites for structural and vibrational investigations. Chemical Science Transactions 2017, 6.
30. Aly, K.I.; Sayed, M.M.; Mohamed, M.G.; Kuo, S.W.; Younis, O. A facile synthetic route and dual function of network luminescent porous polyester and copolyester containing porphyrin moiety for metal ions sensor and dyes adsorption. Microporous and Mesoporous Materials 2020, 298, https://doi.org/10.1016/j.micromeso.2020.110063.
31. Venkataraju, C.; Paulsingh, R. FTIR and EPR Studies of Nickel Substituted Nanostructured Mn Zn Ferrite. Journal of Nanoscience 2014, 2014, 1-5, https://doi.org/10.1155/2014/815385.
32. Kargar, H.; Behjatmanesh-Ardakani, R.; Torabi, V.; Sarvian, A.; Kazemi, Z.; Chavoshpour-Natanzi, Z.; Mirkhani, V.; Sahraei, A.; Nawaz Tahir, M.; Ashfaq, M. Novel copper(II) and zinc(II) complexes of halogenated bidentate N,O-donor Schiff base ligands: Synthesis, characterization, crystal structures, DNA binding, molecular docking, DFT and TD-DFT computational studies. Inorganica Chimica Acta 2021, 514, https://doi.org/10.1016/j.ica.2020.120004.
33. Ardit, M.; Zanelli, C.; Conte, S.; Molinari, C.; Cruciani, G.; Dondi, M. Ceramization of hazardous elements: Benefits and pitfalls of inertisation through silicate ceramics. Journal of Hazardous Materials 2022, 423, https://doi.org/10.1016/j.jhazmat.2021.126851.
34. Modi, K.B.; Raval, P.Y.; Shah, S.J.; Kathad, C.R.; Dulera, S.V.; Popat, M.V.; Zankat, K.B.; Saija, K.G.; Pathak, T.K.; Vasoya, N.H.; Lakhani, V.K.; Chandra, U.; Jha, P.K. Raman and Mossbauer Spectroscopy and X-ray Diffractometry Studies on Quenched Copper–Ferri–Aluminates. *Inorganic Chemistry* 2015, 54, 1543-1555, https://doi.org/10.1021/ic502497a.
35. Tatarchuk, T.; Bououdina, M.; Macyk, W.; Shyichuk, O.; Paliychuk, N.; Yaremiy, I.; Al-Najar, B.; Pacia, M. Structural, Optical, and Magnetic Properties of Zn-Doped CoFe2O4 *Nanoparticles*. *Nanoscale Research Letters* 2017, 12, 141–151, https://doi.org/10.1186/s11671-017-1899-x.
36. Tatarchuk, T.R.; Paliychuk, N.D.; Bououdina, M.; Al-Najar, B.; Pacia, M.; Macyk, W.; Shyichuk, A. Effect of cobalt substitution on structural, elastic, magnetic and optical properties of zinc ferrite nanoparticles. *Journal of Alloys and Compounds* 2018, 731,

1256-1266, https://doi.org/10.1016/j.Jallcom.2017.10.103.
37. Gamal, W.M.; El-Bassiouny, A.A.H.; Abdelsalam, H.K.; Wahab, S.M.A.E. Role of elastic and optical properties on silver nanoferrite and nanochromis for optical switch device applications. Journal of Materials Science: *Materials in Electronics* 2021, 32, 21590-21602, https://doi.org/10.1007/s10854-021-06667-y.

This page is intentionally left blank

Determination of Soil Erosion and Sediment Yield by Rusle using Gis and Remote Sensing- A Case Study of Lake Tana Basin

A S Shobary, A S Elsharkawy, H E M El-Hanafy & O M Moussa

ABSTRACT

Soil erosion is a severe and uninterrupted problem that threatens the environment all over the world. Sedimentation has a great effect on basins with large surface areas. Lake Tana basin is one of these lake basins with a surface area of about 15935 km2. The main objective of this study was to assess soil erosion and concentration of sediment yield of lake Tana basin and map their spatial distribution. The study was conducted by integrating Geographic Information System (GIS), remote sensing, and the Revised Universal Soil Loss equation (RUSLE). Data sets of rainfall, soil, topography, cover management, and conservation practices were integrated and modeled in GIS. Soil loss, sediment delivery ratio (SDR), and sediment yield were estimated. The results showed that the computed mean annual soil loss was 79.3 t.ha-1.y-1. Six classes of soil erosion were classified: very low (0-5), low (5-10), moderate (10-15), moderately high (15-20), high (20-40) and very high (>40) t.ha-1.y-1. About 57.5% of the study area is under low erosion risk (0-10 t.ha-1.y-1), whereas about 40.3% of the study area is under high and very high erosion risk. SDR was estimated, based on the mainstream slope, and found to be 0.281. The findings of the study also showed that the average annual sediment yield of the lake Tana basin is approximately 22.28 t.ha-1.y-1. The results of this study can benefit policymakers to investigate erosional risk areas and take the best appropriate decisions to control soil erosion risk in these regions.

Keywords: soil erosion, sediment yield, RUSLE, SDR, GIS, lake tana basin.

Classification: FOR Code: 050399

Language: English

LJP Copyright ID: 392925
Print ISSN: 2631-8474
Online ISSN: 2631-8482

London Journal of Engineering Research

Volume 22 | Issue 8 | Compilation 1.0

Determination of Soil Erosion and Sediment Yield by Rusle using Gis and Remote Sensing- A Case Study of Lake Tana Basin

A S Shobary[α], A S Elsharkawy[σ], H E M El-Hanafy[ρ] & O M Moussa[Ꞷ]

ABSTRACT

Soil erosion is a severe and uninterrupted problem that threatens the environment all over the world. Sedimentation has a great effect on basins with large surface areas. Lake Tana basin is one of these lake basins with a surface area of about 15935 km². The main objective of this study was to assess soil erosion and concentration of sediment yield of lake Tana basin and map their spatial distribution.

The study was conducted by integrating Geographic Information System (GIS), remote sensing, and the Revised Universal Soil Loss equation (RUSLE). Data sets of rainfall, soil, topography, cover management, and conservation practices were integrated and modeled in GIS. Soil loss, sediment delivery ratio (SDR), and sediment yield were estimated. The results showed that the computed mean annual soil loss was 79.3 $t.ha^{-1}.y^{-1}$. Six classes of soil erosion were classified: very low (0-5), low (5-10), moderate (10-15), moderately high (15-20), high (20-40) and very high (>40) $t.ha^{-1}.y^{-1}$. About 57.5% of the study area is under low erosion risk (0-10 $t.ha^{-1}.y^{-1}$), whereas about 40.3% of the study area is under high and very high erosion risk. SDR was estimated, based on the mainstream slope, and found to be 0.281. The findings of the study also showed that the average annual sediment yield of the lake Tana basin is approximately 22.28 $t.ha^{-1}.y^{-1}$. The results of this study can benefit policymakers to investigate erosional risk areas and take the best appropriate decisions to control soil erosion risk in these regions.

Keywords: soil erosion, sediment yield, RUSLE, SDR, GIS, lake tana basin.

Author α σ ρ Ꞷ: Department of Civil Engineering, Military Technical College, Cairo, Egypt.

I. INTRODUCTION

Soil erosion is the biggest economic challenge that threatens developing countries as it is a dangerous issue in agriculture [1]. Runoff affects soil erosion severely as it is considered a world land dissolution problem [2]. The runoff is an essential factor for soil erosion as it controls the acceleration of erosion rates from high land regions to low ones [3]. Furthermore, human also causes erosion in regions by construction works, dense agriculture production, mining, and intensive population density [4]. Soil erosion accelerated severely in the 20th century over the world [5]. The world mean annual soil erosion varies from 12 to 15 $t.ha^{-1}$ [6]. The annual soil loss was estimated approximately between 0.9-0.95 mm by FAO [7]. FAO also demonstrated that the world annual soil loss by water effect ranges from 20 to 30 gigatonnes [7]. Suppression of erosion and sedimentation is important as they affect the richness of land and water goodness [8]. Soil erosion has a negative effect on agriculture aspect, ecosystems and results in sedimentation boost [9]. Soil erosion causes spoiling crops production and decreases fertile lands, which results in food insecurity [7, 10]. Soil erosion and sedimentation have a direct effect on the cycle of soil nutrients [11]. Therefore , it is obligatory to find solutions to reduce the calamitous effects of soil erosion [12].

Various processes of soil erosion are the cause of the problems related to on-site and off-site [13]. On-site problems are represented inland decay and reducing agriculture production, while off-site problems are related to reducing the lifespan of reservoirs [14]. Soil erosion causes loss in dams and reservoirs storing tendency [15]. Reports have indicated that the global annual loss in storage capacity of reservoirs, related to sedimentation, is about 0.5-1.0 %, and it is expected that, through the coming 20-30 years, the majority of the world's reservoirs capacity would be lost [13]. Findings of studies have shown that the range of sediment deposition of rivers and reservoirs in Africa is between 0.002 and 157 $t.ha^{-1}.y^{-1}$ [16]. Siltation due to water erosion threatens about 19% of Africa reservoirs [7]. Soil erosion has a great impact on the environment as it is resulted in landslides in valleys [17]. Therefore, the determination of soil erosion is an important solution for conservation soil as its spatial distribution assessment can help in advancing protecting policy framework [13].

There are many methods for assessing soil erosion and sediment yield [18]. In the few recent decades, among these methods, the RUSLE model is the most commonly acceptable method around the world [19, 20]. The RUSLE model is the most convenient method for developing countries that suffer from lack of data [21]. The use of the RUSLE model has been advanced from small watersheds to large watersheds to assess mean annual soil loss at the long term [22]. The RUSLE method depends on various factors: rainfall erosivity, slope length-steepness, soil erodibility, crop management factor, and conservation support practice factor [23]. RUSLE can be integrated with GIS and remote sensing techniques to assess sediment yield in a watershed [24]. GIS helps the RUSLE to get more precise outputs [25]. Lewoy Tsegaye and Rishikesh Bharti used the RUSLE and GIS-based approach to assess soil erosion and sediment yield in the Anjeb watershed, northwest Ethiopia [13]. RUSLE, integrated with GIS, model was used by Meena Kumari et al. to determine the concentration of soil loss and sediment yield in the Kolleru lake basin [22].

This research aims to assess soil loss and sediment yield and spatial distribution to investigate the erosional risk zones. The objectives of this study were obtained by: (1) applying integration between the RUSLE model and techniques of GIS and remote sensing to assess soil erosion, (2) recognizing the spatial distribution of soil loss across lake Tana basin, (3) computing SDR factor, (4) determining the concentration of sediment yield and its spatial distribution through the study area.

II. STUDY AREA

Lake Tana is considered the largest freshwater lake in Ethiopia, an with area of about 3000 km^2. It is 78 km long, 67 km wide and 14 km in depth. However, the Nile Basin has many lakes; Lake Tana is the third biggest one. In the northwestern part of Ethiopia, the Lake Tana Basin is situated. Gilgel Abbay, which flows into Lake Tana, is the main source of the Blue Nile (Abbay). Gumera, Ribb, and Megech are also the main rivers that flow into Lake Tana. Lake Tana Basin, which contains lake Tana, lies at latitude 10° 57' 0" and 12° 46' 48" and longitude 36 53' 24" and 38 15' 0". In northeastern of the Abbay Basin, Lake Tana Basin lies with a drainage area of about 15935 km^2. It rises at elevations ranging from 1701 m up to 4108 m above mean sea level as shown in **Figure 1**. The area surrounding the lake is flat, unlike highlands in the north and the east. Its average annual precipitation is 1634 mm, with a higher amount in the south, unlike the north which has a lower amount of rainfall. The area around the lake has a maximum temperature with a range from 14° C to 27° C. The more you get away from the lake, the temperature gets cooler and varies from 1° C to 12° C. It has an average annual potential evapotranspiration of about 1288 mm. Lake Tana has various soil types such Luvisols, Vertisols, Alisols and Cambisols, but the most common soil type is Haplic Luvisols. Chromic Luvisols is considered the second dominant soil type, after Haplic Luvisols, in lake Tana. The geology of lake Tana is prevails Basalt. In the eastern and northeastern part of the basin, Marsh soil is found. In the center of the basin and around the lake, Alluvial deposits are spread.

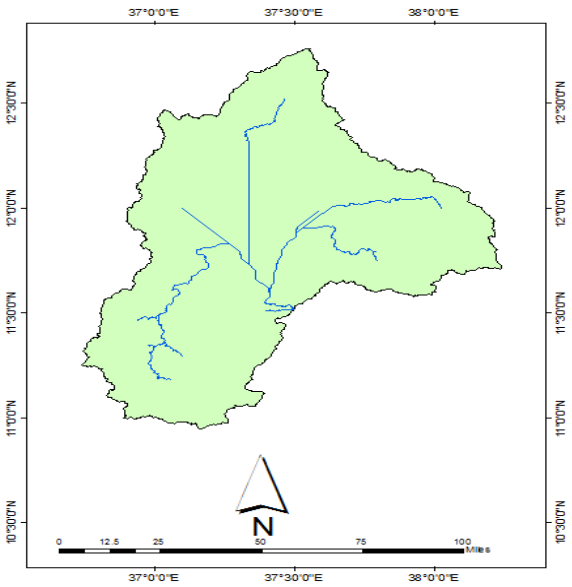

Figure 1: Map of the study area

III. METHODOLOGY

3.1 Soil erosion model – RUSLE

Renard et al. advanced an empirical model, Revised Universal Soil Loss (RUSLE), to assess the mean annual soil loss of watersheds [26]. Soil loss is considered a huge problem in many regions on earth. Laflen and Molden studied and inherited all likely applications of RUSLE to deal with soil loss problems [27]. RUSLE application was investigated in Tigray Region, situated in the highlands of Ethiopia, after adaptation USLE by Hurni [28]. The RUSLE equation estimates mean annual soil loss, which depends on various factors, and is expressed as **equation (1)**

$$A=R*K*LS*C*P \quad (1)$$

Where A is the average annual soil loss (tons per hectare per year), R is the rainfall-runoff erosivity factor (MJ mm h^{-1} ha^{-1} $year^{-1}$), K is the soil erodibility factor (tons ha^{-1} MJ^{-1} mm^{-1}), LS is the slope length-steepness factor (dimensionless), C is the cover and cropping-management factor (dimensionless), P is the support practice factor (dimensionless). **Figure 2** shows the model integrated by GIS and remote sensing to estimate soil loss.

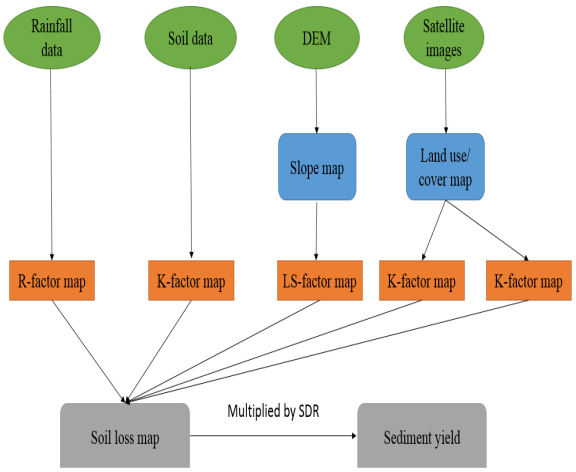

Figure 2: Methodology diagram of soil loss

3.1.1 Rainfall erosivity factor (R)

The rainfall erosivity factor (R) determines the impact of precipitation events and quantifies the amount of possible runoff [29]. In the case of rare rainfall data, a regression equation can be applied to assess the value of the rainfall erosivity factor [30]. Hurni used spatial regression analysis, depending on Ethiopian conditions, to develop a model determining rainfall erosivity factor due to lack of rainfall data [28]. Hurni depended, in his model, on mean annual rainfall data [28]. The equation of the model, derived by Hurni, is expressed as [28]:

$$R = (0.562*P)-8.12 \quad (2)$$

Where R is the rainfall-runoff erosivity factor and P is the mean annual rainfall.

Average annual rainfall data was collected from four rainfall stations as shown in

No	Station name	location		Mean annual rainfall (mm)
		longitude	latitude	
1	Addiet Canna	37° 29'	11° 16'	1494.2
2	Bahir Dar	37° 24'	11° 36'	1430
3	Debre Tabor	38° 01'	11° 51'	1270.1
4	Werota	37° 42'	11° 55'	1203.5

Table 1 and was processed through ArcGIS 10.3 by the Inverse Distance Weighted method (IDW) to produce continuous rainfall data. The R-value was estimated for each grid cell from the uninterrupted rainfall data using equation (2) with the help of the raster calculator tool.

Table 1: Rainfall stations around Lake Tana basin

No	Station name	location		Mean annual rainfall (mm)
		longitude	latitude	
1	Addiet Canna	37° 29'	11° 16'	1494.2
2	Bahir Dar	37° 24'	11° 36'	1430
3	Debre Tabor	38° 01'	11° 51'	1270.1
4	Werota	37° 42'	11° 55'	1203.5

3.1.2 Slope length-steepness factor (LS)

LS factor is the topographic factor that demonstrates the percentage of soil loss per unit area in a field with given standard conditions of slope length of 22.13 m and slope steepness of 9% [19]. Slope length factor (L) represents the impact of slope length on erosion. Slope length is defined as the distance from the start point of overland flow to the point that its slope decreases to the range that deposition begins. There is a positive relation between slope length and soil loss, as when slope length increases, soil loss also increases [31].

Slope steepness factor (S) represents the impact of slope steepness on soil erosion. Soil loss is greatly affected more by slope steepness than by slope length. Soil loss increases as soil steepness increases.

Robert PS et al. linked soil loss with slope length only as when they calculated the topographic sub-factor of slope length; they did not consider the three-dimensional complex terrains in that calculation [32]. Some other researchers observed flow converges and diverges, so they pretended that soil loss is independent on slope length for the three-dimensional complex nature of the terrain. Zhang et al. developed an algorithm to compute LS as they denounced the USLE and RUSLE methods for estimating slope length-steepness factor [33]. Furthermore, limits of estimating slope length in USLE were reanalyzed by calculating accumulated uphill length from cells that interpret convergence of flow paths and area of deposition [34]. Then, the upslope contributing area replaced slope length. In this

study, LS factor estimation equation (3) (developed by Desmet and Groves [35], Moore and Bruch [36, 37], Mitasova and Mitas [38], and Simms et al. [39]) was used equation (3).

$$LS=As/22.130.6*\sin B /0.08961.3 \quad (3)$$

Where LS is the slope length-steepness factor, A is the basin area, and B is the slope angle.
LS factor was estimated through ArcGIS with the help of raster calculator tool by using equation (4) supposed by Mitasova and Mits [40] and Simms et al. [39]

$$\text{POW flow accumulation*cell size/22.13. } 0.6*\text{POWsin slope*0.01745/0.0896. } 1.3 \quad (4)$$

A 30-m resolution DEM was used to prepare the LS factor map through ArcGIS. Arc Hydro tool was used to extract flow accumulation after filling gaps and flow direction were conducted in ArcGIS. Grid cells number is demonstrated by flow accumulation, and 30*30 contributing area is represented by cell size.

3.1.3 Soil erodibility factor (K)

Soil erodibility factor has a great effect on soil erosion through the properties and characteristics of soil. It depends on percentages of silt, sand, and clay as well soil texture. Distribution of particle size and permeability of soil affect soil erodibility factor [41]. In this study, the soil data was derived from global soil raster data downloaded from Harmonized World Soil Database-Food and Agriculture, HWSD FAO, soil web browser. The soil properties data was analyzed by the method depending on the percentages of sand, silt, clay, and organic carbon fraction as shown in equations (5)-(8). Then, the soil erodibility factor was estimated by equation (9).

$$f_{csand} = \left\{0.2 + .3 \exp exp\left[-0.25 m_s\left(1 - \frac{m_{silt}}{100}\right)\right]\right\} \quad (5)$$

$$f_{cl-si} = \left(\frac{m_{silt}}{m_c + m_{silt}}\right)^2 \quad (6)$$

$$f_{orgC} = \left\{1 - \frac{0.25 orgC}{orgC + exp[3.72 - 2.95 orgC]}\right\} \quad (7)$$

$$f_{hisand} = \left\{1 - \frac{0.7\left(1 - \frac{m_s}{100}\right)}{\left(1 - \frac{m_s}{100}\right) + exp\left[-5.51 + 22.9\left(1 - \frac{m_s}{100}\right)\right]}\right\} \quad (8)$$

$$K = f_{csand} * f_{cl-si} * f_{orgC} * f_{hisand} \quad (9)$$

Where K is the soil erodibility factor, f_{csand} is the high-coarse sand content in soil, f_{cl-si} is the clay and silt in content soil, f_{orgC} is the organic carbon content in soil, f_{hisand} is the high sand content in soil, m_s is the percentage of sand fraction content (%), m_{silt} is the percentage of silt fraction content (%), mc is the percentage of clay fraction content (%), and orgC is the percentage of the organic carbon content of the layer (%).

3.1.4 Crop cover and management factor (C)

The crop cover and management factor is defined as the proportion of soil loss from land with particular vegetation and uninterrupted heath [19]. C factor is the only parameter that can be changed over time in most conditions and has a great role in keeping strategy development. C factor map was derived based on the land use and land cover of the lake Tana basin. Six land cover classes were targeted, namely, urban, barren, water, forest, crops, and grass [42]. A supervised maximum likelihood classification method was used. Then, a raster map of land use and land cover was converted into a vector, values of the C factor were assigned and the C factor map was generated.

3.1.5 Conservation support practice factor (P)

Conservation support practice factor is defined as the ratio of soil loss by particular support practice to the correspondent loss of up and downslope farming [19]. The P factor considers the control practices which minimize the rainfall and runoff power of erosion by their effect on runoff velocity, runoff concentration, and drainage patterns [43]. **Table 2** Shows values of the P factor based on slope and cultivation method.

Table 2: P value [44]

Slope (%)	P factor value
0-7	0.55
7-11.3	0.6
11.3-17.6	0.8
17.6-26.8	0.9
>26.5	1

3.2 Sediment Yield Model

3.2.1 Sediment Delivery Ratio (SDR)

Sediment delivery ratio is defined as the fraction of overall soil loss from a specific area in a specific period. It measures the sediment amount that is imparted from sources of erosion to the basin outlet in comparison with the gross amount of discrete soil from the same area. Many physical factors affect the SDR such as land use and land cover, slope, sediment particle size, drainage area, and relief length. Many relationships of SDR have been advanced on the basis of integration between different physical characteristics of the basin [45], but these relationships are applicable for small watersheds only [46]. The average slope of mainstream was found more important than other parameters in the assessment of SDR [47]. Williams and Berndt developed an empirical expression equation to estimate SDR based on a percentage of the main stream slope [47].

$$SDR=0.627*slp0.403 \quad (10)$$

Where slp is the percentage of mainstream slope. Method of Williams and Berndt [47] for estimating SDR was affirmed by Onyando et al. [48]. Empirical equation (10) was applied in this study.

3.2.2 Sediment yield estimation

Sediment yield estimation is the sediment load computed at the outlet of the basin (end of main stream channel). It can also be defined as smoothed sediment load in the drainage area and the gross outcome of deposition and erosion operations through a basin. Factors, which affect erosion and sediment delivery, are the same ones that affect sediment yield, such vegetation cover, climate, basin morphology, soil characteristics, and drainage network properties [49]. Due to lack of basin-appropriate sediment system, sediment yield cannot be measured directly [46]. Therefore, precise assessment of sediment delivery ratio is an essential tactic for estimating sediment yield. In this study, sediment yield was estimated by overlapping the soil loss raster layer acquired from the RUSLE model and sediment delivery ratio based on the slope of mainstream channel as expressed in the following equation:

$$SY= i=1nSDR*A \quad (11)$$

Where SY is the sediment yield, SDR is the sediment delivery ratio, and A is the annual soil loss.

IV. RESULTS AND DISCUSSION

4.1 Soil loss factors evaluation

4.1.1 Rainfall erosivity factor (R)

Rainfall erosivity values were analyzed and computed through ArcGIS using equation (2) with the help of the raster calculator tool. The R value ranges from 505.4 $MJ.mm.ha^{-1}.h^{-1}.y^{-1}$ to 647.4 $MJ.mm.ha^{-1}.h^{-1}.y^{-1}$ with a mean of 568.3 $MJ.mm.ha^{-1}.h^{-1}.y^{-1}$ and standard deviation of 42.1. R factor values are spatially distributed over the lake Tana basin as shown in **Figure 3**. The northern part of the basin has the lowest values of R factor, unlike the southern part which has maximum values.

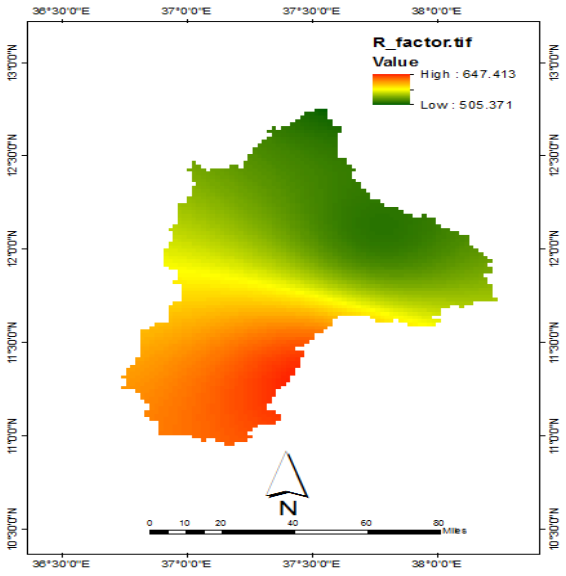

Figure 3: R factor map

4.1.2 Slope length-steepness factor (LS)

The slope length-steepness factor was estimated by using equation (3) and mapped in ArcGIS using the raster calculator tool. LS values range from 0 to 560, representing the steepest part of the basin, as shown in **Figure 4**. The greater the LS factor values, the greater the effect it has on soil erosion for the basin because of the water flows from rainfall and runoff.

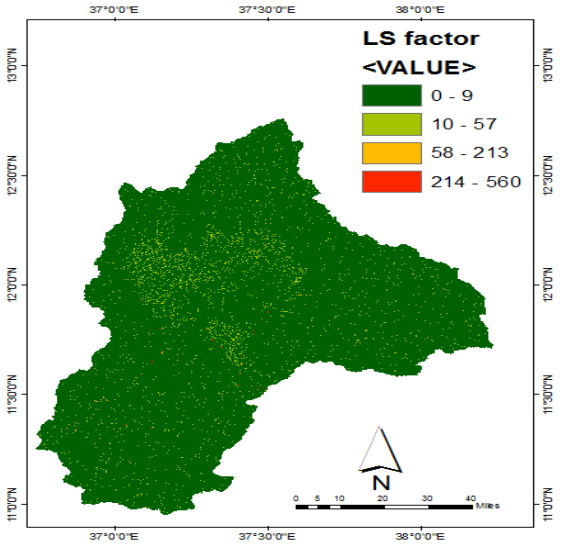

Figure 4: LS factor map

4.1.2 Soil erodibility factor (K)

Hydrologic soil groups for the lake Tana basin were assessed using global soil raster data downloaded from Harmonized World Soil Database-Food and Agriculture, HWSD FAO, soil web browser. Equations (5)-(9) were used to determine the K factor values. In this study, the K factor ranges from 0 to 0.151 with a mean value of 0.11 and standard deviation 0.06. **Figure 5** shows the spatial distribution of K factor as it increases from the lower part to the upper part while it equals 0 for the water body.

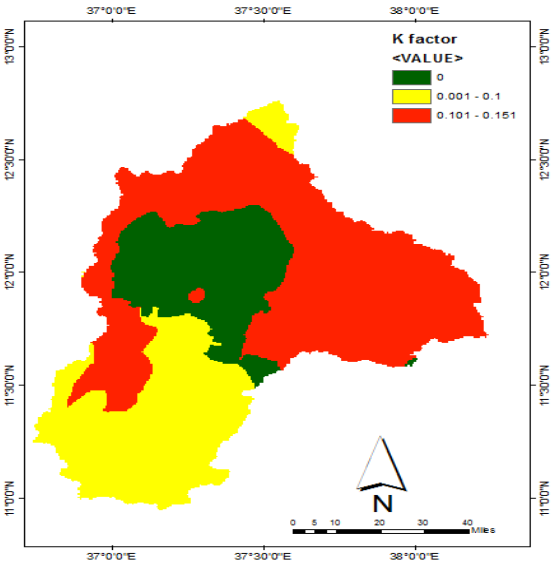

Figure 5: K factor map

4.1.4 Crop cover and management factor (C)

The crop cover and management factor values were assigned as shown in Table 3. the range of the C factor is from 0 to 1 with a mean value of 0.36 and a standard deviation of 0.36. The maximum value of K was assigned to barren land, which represents the most area of Lake Tana basin. Figure 6 shows the spatial distribution of the C factor for the lake Tana basin.

Table 3: C factor values [50]

Land Use Type	C Factor
Barren land	1
Urban	0.5
Water body	0
Forest	.01
Grass	.015
Crops	0.35

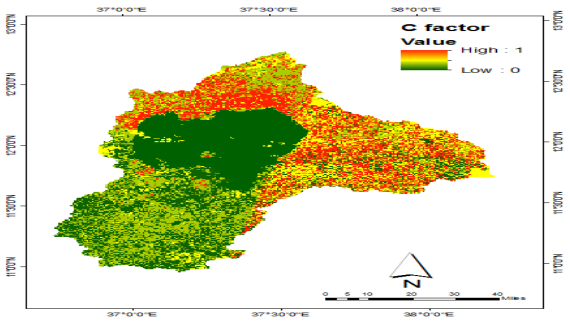

Figure 6: C factor map

4.1.5 Conservation support practice factor (P)

Conservation support practice factor values were computed based on slope and cultivation method as shown in **Table 2**. In this study, the P value varied from 0.55 to 0.6. **Figure 7** shows that P value of most lands in the study area equals 0.6 except the water body which has a value equals 0.55.

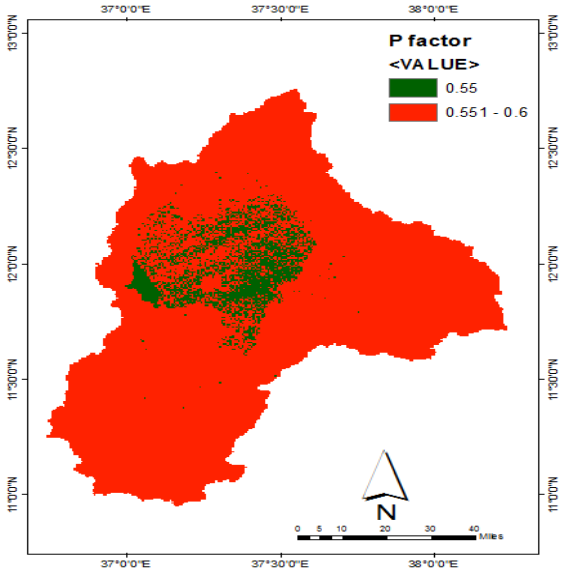

Figure 7: P factor map

4.1.6 Soil loss computation

All layers of RUSLE factors were simulated through ArcGIS using the empirical equation (1) with the help of the raster calculator geoprocessing tool, and the soil map was possessed. The map is represented in a grid format whose cells are 30m*30m. this map accounts for the average annual soil loss per hectare. The range of soil loss computed for the lake Tana basin varies from 0 to 10103 $t.ha^{-1}.y^{-1}$ with a mean value of 79.3 $t.ha^{-1}.y^{-1}$ and a standard deviation of 225.

Six classes of computed soil loss value were targeted on the basis of soil loss spatial distribution and histogram distribution as shown in **Figure 8**. **Table 4** shows that about 57.5% of the lake Tana basin is under low erosion risk (0-10 $t.ha^{-1}.y^{-1}$), and about 40.3% of the study area is under high and very high erosion risk.

Table 4: Soil loss of lake Tana basin

Soil erosion class ($t.ha^{-1}.y^{-1}$)	Area (ha)	Area (%)
Very low (0-5)	884417	56.3
Low (5-10)	19466	1.2
Moderate (10-15)	13667	0.9
Moderately high (15-20)	19610	1.3
High (20-40)	146429	9.3
Very high (>40)	486981	31

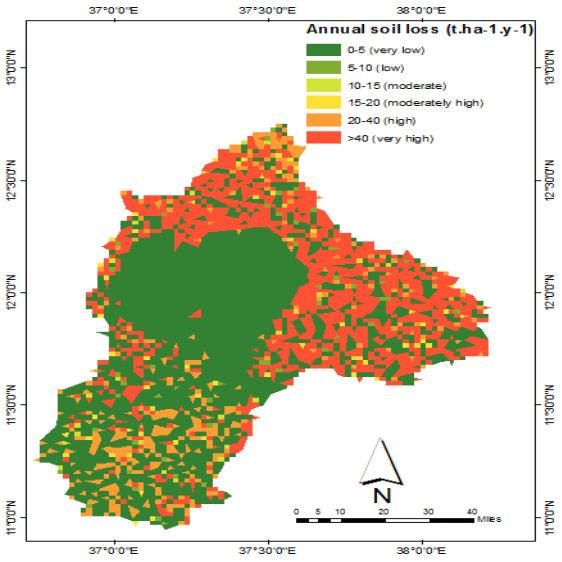

Figure 8: soil loss map of lake Tana basin

4.2 Sediment yield estimation

Sediment delivery ratio was estimated based on the slope of mainstream channel for lake Tana basin through ArcGIS environment. The average channel slope of the study area was found to be 0.136. SDR was computed using equation (10) and was found to be 0.281. sediment yield was calculated using equation (11). Sediment yield map was obtained by using the raster calculator tool through ArcGIS by multiplying the layer of the net soil loss by the average value of SDR. **Figure 9** shows that sediment yield value varies from 0 to 5405 $t.ha^{-1}.y^{-1}$ with an average value of 22.28 $t.ha^{-1}.y^{-1}$. The mean annual sediment yield computed at the outlet of lake Tana basin, in this study, is logic and actual compared to the results of the previous studies. Shimelis Gebriye Setegn used SWAT model to estimate sediment yield delivered to the outlet of the lake Tana basin and found it 24.6 $t.ha^{-1}.y^{-1}$ [51].

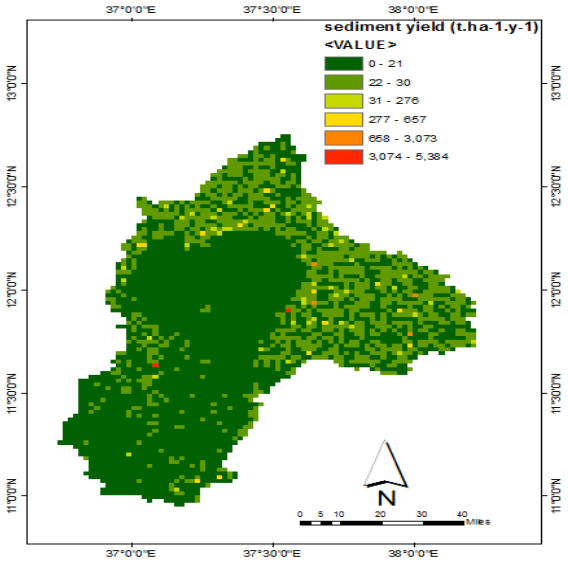

Figure 9: Sediment yield of Tana basin

V. CONCLUSION

Familiar models of investigating erosional hazard zones, even for small watersheds, need enormous data amounts and comprise huge arithmetic works. Integration among the RUSLE model and GIS and

remote sensing techniques is efficient in computing soil erosion and sediment yield for basins. It can also be applied to introduce thematic maps of the spatial distribution of soil loss and sediment yield.

In this study, soil loss and sediment yield in the lake Tana basin were simulated using RUSLE model integrated with GIS and remote sensing technologies. The results and analysis show that the average annual soil loss computed at the outlet of lake Tana basin is about 79.3 $t.ha^{-1}.y^{-1}$. This study also investigates zones that exposed erosion risk. The findings indicated that about 40.3 of the study area is under high and very high erosion risk. It is observed that the northern part of lake Tana basin is the most erosional risky zone. Map of annual soil loss is useful to carry out appropriate soil protection practices in areas of high erosion risk.

SDR was estimated through the ArcGIS environment based on the slope of the mainstream channel and found to be 0.281. sediment yield was assessed and found ranges from 0 to 5405 $t.ha^{-1}.y^{-1}$ with a mean value of 22.28 $t.ha^{-1}.y^{-1}$.

RUSLE method based on GIS was successfully used to estimate soil loss and sediment yield and investigate erosion risk zones. This study can be used for other basins other than lake Tana basin. It can help policymakers in making the best appropriate decisions to control soil erosion risk in various regions.

REFERENCES

1. Mekonnen, M., et al., *Reducing Sediment Connectivity Through Man-Made and Natural Sediment Sinks in the Minizr Catchment, Northwest Ethiopia*. 2016.
2. Novara, A., et al., *Understanding the role of soil erosion on CO2-C loss using 13C isotopic signatures in abandoned Mediterranean agricultural land.* Science of the Total Environment, 2016. **550**: p. 330-336.
3. Oliveira, M.L., et al., *River dynamics and nanopaticles formation: a comprehensive study on the nanoparticle geochemistry of suspended sediments in the Magdalena River, Caribbean Industrial Area*. Journal of Cleaner Production, 2019. **213**: p. 819-824.
4. Nyssen, J., et al., *Land management in the northern Ethiopian highlands: local and global perspectives; past, present and future*. Land Degradation & Development, 2015. **26**(7): p. 759-764.
5. Singh, G. and R.K. Panda, *Grid-cell based assessment of soil erosion potential for identification of critical erosion prone areas using USLE, GIS and remote sensing: A case study in the Kapgari watershed, India*. International Soil and Water Conservation Research, 2017. **5**(3): p. 202-211.
6. Ashiagbor, G., et al., *Modeling soil erosion using RUSLE and GIS tools*. Int J Remote Sens Geosci, 2013. **2**(4): p. 1-17.
7. FAO, I., *Status of the world's soil resources (SWSR)–main report*. Food and agriculture organization of the United Nations and intergovernmental technical panel on soils, Rome, Italy, 2015. **650**.
8. Wijesundara, N., N. Abeysingha, and D. Dissanayake, *GIS-based soil loss estimation using RUSLE model: A case of Kirindi Oya river basin, Sri Lanka*. Modeling Earth Systems and Environment, 2018. **4**(1): p. 251-262.
9. Pham, T.G., J. Degener, and M. Kappas, *Integrated universal soil loss equation (USLE) and Geographical Information System (GIS) for soil erosion estimation in A Sap basin: Central Vietnam*. International Soil and Water Conservation Research, 2018. **6**(2): p. 99-110.
10. Kayet, N., et al., *Evaluation of soil loss estimation using the RUSLE model and SCS-CN method in hillslope mining areas*. International Soil and Water Conservation Research, 2018. **6**(1): p. 31-42.
11. Quinton, J.N., et al., *The impact of agricultural soil erosion on biogeochemical cycling*. Nature Geoscience, 2010. **3**(5): p. 311-314.

12. Dissanayake, D., T. Morimoto, and M. Ranagalage, *Accessing the soil erosion rate based on RUSLE model for sustainable land use management: A case study of the Kotmale watershed, Sri Lanka*. Modeling Earth Systems and Environment, 2019. **5**(1): p. 291-306.
13. Tsegaye, L. and R. Bharti, *Soil erosion and sediment yield assessment using RUSLE and GIS-based approach in Anjeb watershed, Northwest Ethiopia*. SN Applied Sciences, 2021. **3**(5): p. 1-19.
14. Balthazar, V., et al., *Human impact on sediment fluxes within the Blue Nile and Atbara River basins*. Geomorphology, 2013. **180**: p. 231-241.
15. Vaezi, A.R., et al., *Assessment of soil particle erodibility and sediment trapping using check dams in small semi-arid catchments*. Catena, 2017. **157**: p. 227-240.
16. Vanmaercke, M., et al., *Sediment yield in Africa*. Earth-Science Reviews, 2014. **136**: p. 350-368.
17. Sentis, I.P., *A soil water balance model for monitoring soil erosion processes and effects on steep lands in the tropics*. Soil technology, 1997. **11**(1): p. 17-30.
18. Brenner, C., *Monitoring and simulation of soil erosion in the Ethiopian Highlands on a plot scale*. 2013, Universitaet für Bodenkultur Wien, Center for Development Research (BOKU/CDR).
19. Wischmeier, W.H. and D.D. Smith, *Predicting rainfall erosion losses: a guide to conservation planning*. 1978: Department of Agriculture, Science and Education Administration.
20. Borrelli, P., et al., *Assessment of the impacts of clear-cutting on soil loss by water erosion in Italian forests: First comprehensive monitoring and modelling approach*. Catena, 2017. **149**: p. 770-781.
21. Perović, V., et al., *Spatial modelling of soil erosion potential in a mountainous watershed of South-eastern Serbia*. Environmental Earth Sciences, 2013. **68**(1): p. 115-128.
22. Kolli, M.K., C. Opp, and M. Groll, *Estimation of soil erosion and sediment yield concentration across the Kolleru Lake catchment using GIS*. Environmental Earth Sciences, 2021. **80**(4): p. 1-14.
23. Sheikh[1], A.H., S. Palria, and A. Alam, *Integration of GIS and universal soil loss equation (USLE) for soil loss estimation in a Himalayan watershed*. Recent Research in Science and Technology, 2011. **3**(3).
24. Bera, A., *Assessment of soil loss by universal soil loss equation (USLE) model using GIS techniques: a case study of Gumti River Basin, Tripura, India*. Modeling Earth Systems and Environment, 2017. **3**(1): p. 29.
25. Pandey, A., V. Chowdary, and B. Mal, *Identification of critical erosion prone areas in the small agricultural watershed using USLE, GIS and remote sensing*. Water resources management, 2007. **21**(4): p. 729-746.
26. Renard, K.G., *Predicting soil erosion by water: a guide to conservation planning with the Revised Universal Soil Loss Equation (RUSLE)*. 1997: United States Government Printing.
27. Laflen, J.M. and W. Moldenhauer, *Pioneering soil erosion prediction: the USLE story*. 2003: World Association of Soil and Water Conservation.
28. Hurni, H., *Soil conservation manual for Ethiopia*. Ministry of Agriculture, Addis Ababa, 1985.
29. Yue-Qing, X., et al., *Adapting the RUSLE and GIS to model soil erosion risk in a mountains karst watershed, Guizhou Province, China*. Environmental monitoring and assessment, 2008. **141**(1): p. 275-286.
30. Helmecke, M., *Assessment of soil erosion in selected micro-watersheds in koraput District, Orissa*. Foundation for Ecological Security Anand-388, 2009. **1**.
31. Gelagay, H., *RUSLE and SDR model based sediment yield assessment in a GIS and remote sensing environment; a case study of Koga watershed, Upper Blue Nile Basin, Ethiopia*. Hydrology Current Research, 2016. **7**(2): p. 239.
32. Stone, R.P. and D. Hilborn, *Universal Soil Loss Equation, USLE*. 2001: Ministry of Agriculture, Food & Rural Affairs, Agriculture & Rural.

33. Zhang, H., et al., *Extension of a GIS procedure for calculating the RUSLE equation LS factor*. Computers & Geosciences, 2013. **52**: p. 177-188.
34. Hickey, R., *Slope angle and slope length solutions for GIS*. Cartography, 2000. **29**(1): p. 1-8.
35. Desmet, P. and G. Govers, *A GIS procedure for automatically calculating the USLE LS factor on topographically complex landscape units*. Journal of soil and water conservation, 1996. **51**(5): p. 427-433.
36. Moore, I. and G. Burch, *Modelling erosion and deposition: topographic effects*. Transactions of the ASAE, 1986. **29**(6): p. 1624-1630.
37. Moore, I.D. and G.J. Burch, *Physical basis of the length-slope factor in the universal soil loss equation*. Soil Science Society of America Journal, 1986. **50**(5): p. 1294-1298.
38. Mitasova, H., et al., *Modelling topographic potential for erosion and deposition using GIS*. International journal of geographical information systems, 1996. **10**(5): p. 629-641.
39. Simms, A., C. Woodroffe, and B. Jones, *Application of RUSLE for erosion management in a coastal catchment, southern NSW*. 2003.
40. Mitasova, H. and L. Mitas, *Modeling soil detachment with RUSLE 3d using GIS*. University of Illinois at Urbana-Champaign, 1999.
41. Chuenchum, P., M. Xu, and W. Tang, *Estimation of soil erosion and sediment yield in the Lancang–Mekong river using the modified revised universal soil loss equation and GIS techniques*. Water, 2020. **12**(1): p. 135.
42. Shobary, A., et al. *Updating land use and land cover classes of Blue Nile basin using landsat-8 images*. in *IOP Conference Series: Materials Science and Engineering*. 2021. IOP Publishing.
43. Kim, H.-S. and P.Y. Julien, *Soil erosion modeling using RUSLE and GIS on the IMHA Watershed*. Water Engineering Research, 2006. **7**(1): p. 29-41.
44. Karamage, F., et al., *Deforestation effects on soil erosion in the Lake Kivu Basin, DR Congo-Rwanda*. Forests, 2016. **7**(11): p. 281.
45. Ouyang, D. and J. Bartholic. *Predicting sediment delivery ratio in Saginaw Bay watershed*. in *Proceedings of the 22nd National Association of Environmental Professionals Conference*. 1997.
46. Mutua, B.M. and A. Klik, *Estimating spatial sediment delivery ratio on a large rural catchment*. 2006.
47. Williams, J.R. and H.D. Berndt, *Sediment yield computed with universal equation*. Journal of the Hydraulics Division, 1972. **98**(12): p. 2087-2098.
48. Onyando, J., P. Kisoyan, and M. Chemelil, *Estimation of potential soil erosion for river perkerra catchment in Kenya*. Water Resources Management, 2005. **19**(2): p. 133-143.
49. Hovius, N., et al., *Landslide-driven drainage network evolution in a pre-steady-state mountain belt: Finisterre Mountains, Papua New Guinea*. Geology, 1998. **26**(12): p. 1071-1074.
50. Teh, S.H., et al., *GIS-Based Upland Erosion Mapping*, in *Handbook of Engineering Hydrology: Modeling, Climate Change, and Variability*. 2014, CRC Press. p. 313-330.
51. Setegn, S.G., *Hydrological and sediment yield modelling in Lake Tana basin, Blue Nile Ethiopia*. 2008, KTH.

London Journal Press Membership

For Authors, subscribers, Boards and organizations

London Journals Press membership is an elite community of scholars, researchers, scientists, professionals and institutions associated with all the major disciplines. London Journals Press memberships are for individuals, research institutions, and universities. Authors, subscribers, Editorial Board members, Advisory Board members, and organizations are all part of member network.

Read more and apply for membership here:
https://journalspress.com/journals/membership

For Authors

Author Membership provide access to scientific innovation, next generation tools, access to conferences/seminars /symposiums/webinars, networking opportunities, and privileged benefits.
Authors may submit research manuscript or paper without being an existing member of LJP. Once a non-member author submits a research paper he/she becomes a part of "Provisional Author Membership".

For Institutions

Society flourish when two institutions come together." Organizations, research institutes, and universities can join LJP Subscription membership or privileged "Fellow Membership" membership facilitating researchers to publish their work with us, become peer reviewers and join us on Advisory Board.

For Subscribers

Subscribe to distinguished STM (scientific, technical, and medical) publisher. Subscription membership is available for individuals universities and institutions (print & online). Subscribers can access journals from our libraries, published in different formats like Printed Hardcopy, Interactive PDFs, EPUBs, eBooks, indexable documents and the author managed dynamic live web page articles, LaTeX, PDFs etc.

GO GREEN AND HELP
SAVE THE ENVIRONMENT

JOURNAL AVAILABLE IN

PRINTED VERSION, INTERACTIVE PDFS, EPUBS, EBOOKS, INDEXABLE DOCUMENTS AND THE AUTHOR MANAGED DYNAMIC LIVE WEB PAGE ARTICLES, LATEX, PDFS, RESTRUCTURED TEXT, TEXTILE, HTML, DOCBOOK, MEDIAWIKI MARKUP, TWIKI MARKUP, OPML, EMACS ORG-MODE & OTHER

SCAN TO KNOW MORE

support@journalspress.com
www.journalspress.com

*THIS JOURNAL SUPPORT AUGMENTED REALITY APPS AND SOFTWARES